Effect of Self-Excited Acoustic Perturbations on Flow Characteristics around Rectangular Cylinders with Varied Geometrical Aspects

by

Ahmed Shoukry

A thesis submitted to the School of Graduate and Postdoctoral Studies in partial fulfillment of the requirements for the degree of

Master of Applied Science

in

Mechanical Engineering

Faculty of Engineering and Applied Science

University of Ontario Institute of Technology
(Ontario Tech University)

Ontario, Canada

August 2023

THESIS EXAMINATION INFORMATION

Submitted by: **Ahmed Shoukry**

Master of Applied Science in Mechanical Engineering

Title: Effect of Self-Excited Acoustic Perturbations on Flow Characteristics around Rectangular Cylinders with Varied Geometrical Aspects

An oral defense of this thesis took place on August 16th, 2023 in front of the following examining committee:

Examining Committee

Chair of Examining Committee	Dr. Amirkianoosh Kiani
Research Supervisor	Dr. Atef Mohany
Examining Committee Member	Dr. Brendan MacDonald
Thesis Examiner	Dr. Sayyed Ali Hosseini

The above committee determined that the thesis is acceptable in form and content and that a satisfactory knowledge of the field covered by the thesis was demonstrated by the candidate during an oral examination. A signed copy of the Certificate of Approval is available from the School of Graduate and Postdoctoral Studies.

Abstract

This study explores the effects of aspect ratio, edge geometry and incidence angles on the dynamic lift force, wake behaviors, and the susceptibility of such geometrical aspects to self-excited acoustic resonance in rectangular cylinders inside a high-speed wind tunnel. Experimental findings demonstrate a notable shift in both acoustic pressure and dynamic lift force during resonance excitation for rods characterized by an aspect ratio of $l/h = 0.5$. For cylinders with an aspect ratio of $l/h = 2$, there is unexpected excitation of the third acoustic mode, imposing a considerable reduction in the dynamic lift force and alteration in shear layer dynamics, which subsequently impacts the shedding pattern. The study reveals that modifying the shape of the upstream edges to be rounded can alter the shedding pattern and decrease dynamic the loading, whereas alterations to the downstream edges amplify the sound pressure level (SPL) during resonance. Particle image velocimetry (PIV) measurements further accentuate the crucial role of incidence angles in modulating flow structures, vortex generation, and wake dynamics. The combined effect of a small angle of incidence and self-excited acoustic resonance was found to have an added streamwise length effect. This research emphasizes the significant influence of incidence angles and self-induced acoustic resonance on the ILEV/TEVS shedding pattern, underscoring the importance of rod geometry and orientation in the mechanism of flow-sound interaction.

Keywords: Flow-induced noise, rectangular cylinders, Flow-excited acoustic resonance, Hydrodynamic loading on bluff bodies, Shear layer instability, Particle image velocimetry.

Note: Rectangular rod and cylinder are used interchangeably in this thesis.

Acknowledgements

First and foremost, I am sincerely grateful to my supervisor, Prof. Mohany, for his unwavering guidance, insightful suggestions, and continuous encouragement throughout this research journey. His expertise and mentorship have been invaluable in shaping the direction and quality of the work outlined in this thesis.

I would like to express my gratitude to my colleagues Ahmed Elgazwy, Omar Hammad, Abdalrahman Alsaqa, Marc Hanna, Ali Saudy, and Rasha Noufal who have been a source of motivation and support throughout this journey. Their discussions, encouragement, and friendship have made the research experience more enjoyable and rewarding.

A special mention goes to Dr. Mohammed Alziadeh who willingly and generously contributed his time and expertise to this study. His involvement and cooperation were crucial in gathering the necessary data and insights, and I am sincerely grateful for their invaluable contributions.

Lastly, yet of utmost significance, I wish to express my deepest gratitude to two incredible individuals who have played an immeasurable role in shaping my academic pursuits: my beloved father, Khaled, and my dear sister, Soha. Their unwavering love, unwavering support, and unwavering understanding have been the cornerstone of my educational journey. I am forever indebted to them for their unwavering belief in my abilities and the countless sacrifices they have made to ensure my success. Their

presence in my life has been a constant source of strength and inspiration, and I am eternally grateful for their profound impact on my personal and academic growth.

"... And when ye are told to rise up, rise up. Allah will raise up, to (suitable) ranks (and degrees), those of you who believe and who have been granted (mystic) Knowledge. And Allah is well-acquainted with all ye do" [Quran, 58:11]

Dedication

In loving memory of the one who touched my heart deeply and is now peacefully resting, I dedicate this work to my late mother, Sahar. Though I long for her presence and dearly miss her, her love and influence continue to inspire me every day. This thesis stands as a tribute to her unwavering support, boundless love, and the profound impact she had on my life. May her soul rest in eternal peace...

Author's Declaration

I hereby declare that this thesis consists of original work of which I have authored. This is a true copy of the thesis, including any required final revisions, as accepted by my examiners.

I authorize the University of Ontario Institute of Technology (Ontario Tech University) to lend this thesis to other institutions or individuals for the purpose of scholarly research. I further authorize University of Ontario Institute of Technology (Ontario Tech University) to reproduce this thesis by photocopying or by other means, in total or in part, at the request of other institutions or individuals for the purpose of scholarly research. I understand that my thesis will be made electronically available to the public.

Ahmed Shoukry

Statement of Contributions

I hereby affirm that I am the exclusive author of this thesis. All external ideas, methodologies, or resources utilized in this work have been appropriately cited to give due credit to their original authors. Moreover, I confirm that the creative contributions and innovative insights described within this thesis originate solely from my own endeavors with the aid of my supervisor Prof. Atef Mohany. Below is a list of publications abstracted from this thesis.

Proceeding Publication(s)

1. Shoukry, A., Mohany, A., 2022. Direct measurements of the dynamic lift force acting on rectangular rods in cross-flow during acoustic resonance excitation. Proceedings of the 12th International Conference on Flow-Induced Vibration 1, 263 – 279.

Journal Publication(s)

1. A. Shoukry and A. Mohany, Characteristics of the flow-induced noise from rectangular rods with different aspect ratios and edge geometry. Journal of Fluids and Structures (2023) 103959, https://doi.org/10.1016/j.jfluidstructs.2023.103959.

2. A. Mohany, A. Shoukry , and L. Pastur. Self-selection of Flow Instabilities by Acoustic Perturbations Around Rectangular Cylinder in Cross-Flow. Journal of Fluid Mechanics (2023) (Submitted).

Contents

Abstract ii

Acknowledgements iii

Dedication v

Author's Declaration vi

Statement of Contributions vii

Contents viii

List of Tables xi

List of Figures xii

Nomenclature xvii

1 Introduction 1
- 1.1 Problem overview . . . 1
- 1.2 Motivation . . . 2
- 1.3 Objectives . . . 3
- 1.4 Thesis outline . . . 4

2 Literature review 8
- 2.1 Bluff body aerodynamics . . . 8
  - 2.1.1 Vortex shedding . . . 9
  - 2.1.2 Flow instabilities . . . 10
- 2.2 Flow around rectangular cylinders . . . 15
  - 2.2.1 Effect of the aspect ratio (AR) on the wake dynamics and hydrodynamic loading . . . 17
  - 2.2.2 Effect of Reynolds number on the separated shear layer . . . 21
  - 2.2.3 Approaching flow turbulence level effect . . . 24
  - 2.2.4 Shedding patterns and flow instabilities for elongated cylinders 26

2.3 Flow around rectangular and square cylinders at an angle of incidence 35
2.3.1 Flow regimes classification and the critical angle of attack . . 36
2.3.2 Effect of angle of incidence on the hydrodynamic loading . . . 41
2.4 The effect of externally applied periodic disturbance on the flow topology 44
2.4.1 Applied velocity perturbation 45
2.4.2 Forced oscillations 46
2.5 Flow-sound interaction mechanism in rectangular cylinders 49
2.5.1 Sound generation by periodic flow structures 49
2.5.2 Self-excited acoustic resonance 51
2.5.3 Rectangular cylinders under acoustic resonant conditions . . . 52
2.6 Summary and thesis scope 56

3 Characteristics of the flow-induced noise from rectangular rods with different aspect ratios and edge geometry 58
3.1 Introduction 58
3.2 Experimental Setup 61
3.2.1 Aeroacoustic measurements 64
3.2.2 Dynamic lift force measurements 64
3.2.3 Particle-image velocimetry (PIV) measurements 66
3.3 Results and discussion 67
3.3.1 Aeroacoustic response 67
3.3.2 Dynamic lift force measurements 73
3.3.3 Dynamic lift force decomposition 76
3.3.4 Time-averaged flow topology 82
3.3.5 Phase-averaged flow topology 89
3.3.6 Phase-locked flow topology during self-excited acoustic resonance 95
3.4 Conclusion 96

4 Self-selection of Flow Instabilities by Acoustic Perturbations Around Rectangular Cylinder in Cross-Flow 102
4.1 Introduction 102
4.2 Experimental Setup 110
4.2.1 Wind tunnel facility 110
4.2.2 Acoustic pressure measurements 111
4.2.3 Particle image velocimetry (PIV) 113
4.3 Results and discussion 117
4.3.1 Flow under non-resonant condition 117
4.3.2 Flow under resonant condition 127
4.3.3 Conclusions 159

5 Conclusions and Recommendations 161
5.1 Summary and conclusions 161
5.2 Recommendations for future investigations 163

Bibliography **165**

A Appendices **184**
A.1 Particle Image Velocimetry (PIV) 184

List of Tables

3.1 The six investigated cases with the dimensions in inches 63

3.2 The normalized acoustic pressure P^* and the lock-in range U_{res}/U_{Max} for all the tested cases 72

3.3 The ratio between the C_l' at the peak of the two acoustic modes which were excited either early or at the coincidence frequency and the average value outside of acoustic resonance.(1C) denotes first acoustic mode excitation at coincidence frequency; (3C) denotes third acoustic mode excitation at coincidence frequency; (3E) denotes early third acoustic mode excitation. 78

3.4 The value and location ($L_{\overline{v'v'}/U_\infty^2}/h$) of the peak normal Reynolds stress ($\overline{v'v'}/U_\infty^2$) and the C_l' value at the time-averaged analysis velocity ($U_\infty = 27.6m/s$) 89

List of Figures

2.1 Visual representation of Von Kármán vorticies and the spatial spacing between adjacent vorticies 10
2.2 Schematic sketch that depicts an impulse response (a) absolutely unstable flow; (b) convectively unstable flow [74] 13
2.3 Stability map of state selection for laminar wakes [55] 16
2.4 The variation the drag coefficient C_d with different aspect ratios AR [82] 19
2.5 The variation of Strouhal number St with different aspect ratios AR [82] 19
2.6 Flow around rectangular cylinder of different aspect ratio filmed using dye filament in a water tunnel (Adapted from [9]) 20
2.7 Side view of the vorticies downstream (a) $320 < Re_h < 380$; (b) $Re_h > 380$ (Adapted from [109]) 22
2.8 Mean pressure variation at different approach turbulence intensities (σ_u/u) (Adapted from [38]) 25
2.9 Reattachment length (S_r) variation at different approach turbulence intensities (σ_u/u) (Adapted from [104]) 26
2.10 Strouhal number (St_h) VS the cylinder aspect ratio (l/h) (Adapted from [94]) 28
2.11 Strouhal number (St_h) VS the cylinder aspect ratio (l/h) at $Re_l = 1000$ (Adapted from [79]) 30
2.12 The process of coalescence of mixing layers small-scale vorticies into large-scale vorticial structure (Adapted from [40]) 32
2.13 ILEV mechanism for an rectangular cylinder with $6 < AR < 9$ and $n = 2$ (Adapted from [67]) 32
2.14 Vortex shedding patterns from rectangular cylinders with progressively increasing aspect ratio 34
2.15 Vorticity contour delineating the LE and TE vorticies shedding (Adapted from [91]) 35
2.16 Fluctuating pressure coefficient Cp' at different points on the faces of the square cylinder at different angle of incidence. $Re_l = 27,000$ squares; $Re_l = 41,000$ circles (Adapted from [49]) 37
2.17 Streamlines which outlines the different flow patterns at $Re_l = 5000$ (Adapted from [46]) 39

2.18 Surface-oil measurements showing the position of the topological critical point at different Reynolds number (Adapted from [46]) 40
2.19 Lift and Drag coefficients at a range of Reynolds numbers (Adapted from [49]) 42
2.20 The effect of the approaching flow turbulence level on the drag and lift coefficients at different angles of incidence (Adapted from [126]) . . . 43
2.21 Cylinder edge geometry effect on the mean lift and drag coefficients at different angles of incidence (Adapted from [126]) 43
2.22 (a) Shedding phase wrt to the cylinder oscillation frequency, (b) Base pressure coefficient $C_{p(b)}$ vs. the oscillation frequency of the cylinder. (a) and (b) are at the same amplitude ratio. (Adapted from [120]) . . 47
2.23 Dipole source sound radiation in the far field. (Adapted from [11]) . . 49
2.24 Different leading and trailing edge geometries with the SPL scale. (Adapted from [132]) 50
2.25 SPL at different angles of incidence for a square cylinder (Adapted from [33]) 51
2.26 Rectangular cylinder positioned at the anti-node of odd-numbered transverse acoustic modes within a duct along with the pressure distribution associated with the first pair of these modes (This figure is not to scale). 52
2.27 Schematic of the arrangement of the plates in cross flow (Adapted from [92]) 53
2.28 Vortex shedding frequency at different flow velocity with the natural and excited modes coincidence with acoustic transverse modes ($Parker's\beta - mode$). (Adapted from [140]) 54
2.29 Vorticity field at the peak of acoustic resonance excitation of the same transverse acoustic mode ($Parker's\beta - mode$) at two different flow velocities showing the two shedding patterns for a rectangular cylidner with $AR = 2$ (Adapted from [114]) 54
2.30 SPL at peak of acoustic resonance excitation at different cross-stream length to spacing ratio (Adapted from [122]) 56

3.1 Schematic of the six investigated cases 63
3.2 (a) Schematic of the particle image velocimetry setup. (b) Dynamic lift force measurements setup 63
3.3 Raw signal measured from the force sensors for aspect ratio $l/h = 2$ all-sharp edges case at U = 31m/s. 66
3.4 Acoustic pressure spectra for;(a) Square (b) Bluff rectangle (c) all-sharp edges rectangle, (d) two-upstream rounded edges rectangle, (e) two-downstream rounded edges rectangle, and (f) all-rounded edges rectangle. 74

3.5 RMS of the the fluctuating lift coefficient (C_l') vs free stream velocity (U_∞) with the acoustic pressure dominant frequency superimposed on the secondary axis : (a) Square (b) Bluff rectangle (c) all-sharp edges rectangle, (d) two-upstream rounded edges rectangle, (e) two-downstream rounded edges rectangle, and (f) all-rounded edges rectangle. 77
3.6 In-phase c_{mh} and out-of-phase c_{dh} lift coefficient components for all the studied cases 83
3.7 Time-averaged normalized streamwise velocity ($\overline{u}/U_\infty$) contours with streamlines superimposed in the x–y plane at $U_\infty = 27.6m/s$. (a) all-sharp edges, (b) two-upstream rounded edges, (c) two-downstream rounded edges, and (d) all-rounded edges. The red contour line represents $\overline{u}/U_\infty = 0$, which outlines the recirculation region. The streamlines are represented by contour lines. 85
3.8 Time-averaged Reynolds shear stress ($\overline{u'u'}/U_\infty^2$) and normal stress ($\overline{v'v'}/U_\infty^2$) at $U_\infty = 27.6m/s$. (a, b) all-sharp edges, (c, d) two-upstream rounded edges, (e, f) two-downstream rounded edges, and (g, h) all-rounded edges. The red contour line represents $\overline{u}/U_\infty = 0$, which outlines the recirculation region. 88
3.9 Energy distribution of the POD modes in the turbulent kinetic energy: (a) mode energy (λ_k), (b) cumulative mode energy, and (c) Scatter plot of the temporal coefficients a_1 and a_2 from the POD analysis performed on the PIV data for the all edges sharp case. Black open square-downstream rounded edges; yellow open square-all edges rounded; green open square-sharp edges; red open square-upstream rounded edges 91
3.10 Four equidistant Phase-averaged vorticity fields with the flow streamlines superimposed at $U_\infty = 27.6m/s$. (a) all-sharp edges, (b) two-upstream rounded edges. 93
3.11 Four equidistant Phase-averaged vorticity fields with the flow streamlines superimposed at $U_\infty = 27.6m/s$ (c) two-downstream rounded edges, and (d) all-rounded edges. 94
3.12 Eight equidistant phase-locked vorticity fields with the flow streamlines superimposed in the wake during third acoustic mode excitation over an acoustic pressure cycle at its peak value for the two upstream rounded edges case 97
3.13 Eight equidistant phase-locked vorticity fields with the flow streamlines superimposed in the wake during third acoustic mode excitation over an acoustic pressure cycle at its peak value for the two downstream rounded edges case. 98

3.14 A Schematic that shows the effect of the rod length in the flow direction, upstream edge rounding, and the acoustic excitation on pronouncing different shedding modes in the wake of rectangular rods. . 101

4.1 Schematic of the rectangular cylinder geometry with faces and nodes label 111
4.2 Schematic representation of the acoustic pressure distribution inside the duct for the odd-numbered transverse modes. 113
4.3 Schematic of the full PIV setup. 114
4.4 Strouhal number of natural shedding measured under non-resonant conditions at different angles of incidence. 118
4.5 Time-averaged normalized streamwise velocity ($\overline{u}/U_\infty$) contours with streamlines superimposed in the x–y plane at $U_\infty = 19.32m/s$. The red contour line represents $\overline{u}/U_\infty = 0$, which outlines the recirculation region. The streamlines are represented by contour lines. The 'X' outlines the end of the recirculation region 121
4.6 Time-averaged transverse Reynolds stress ($\overline{v'v'}/U_\infty^2$) at different angle of incidence α. 123
4.7 Energy distribution of the POD modes in the turbulent kinetic energy: (a) mode energy (λ_k), and (b) Scatter plot of the temporal coefficients a_1 and a_2 from the POD analysis performed on the PIV data for the angle of incidence $\alpha = 90°$. The definition of the red circle is given by Eq.(4.4). 128
4.8 Phase-averaged vorticity field with the streamlines superimposed at $U_\infty = 19.32\ m/s$ for all the tested incidence angles 129
4.9 Phase-averaged vorticity field with the streamlines superimposed at $U_\infty = 19.32\ m/s$ for all the tested incidence angles (Continued) . . . 130
4.10 Aeroacoustic response of a rectangular cylinder with aspect ratio $AR = 2$ at different angle of incidence α 134
4.11 Phase-locked vorticity field with the streamlines superimposed over a complete acoustic pressure cycle during acoustic third mode excitation f_{a3} for $\alpha = 0°$ at $St_{l'} = 0.6$ 138
4.12 Single complete acoustic pressure cycle discretized at an arbitrary phase ϕ_a during third mode excitation f_{a3} for $\alpha = 0°$ at $St_{l'} = 0.6$ 139
4.13 Phase-locked vorticity field with the streamlines superimposed over a complete acoustic pressure cycle during acoustic third mode excitation f_{a3} for $\alpha = 5°$ at $St_{l'} = 1.21$ 140
4.14 Single complete acoustic pressure cycle discretized at an arbitrary phase ϕ_a during third mode excitation f_{a3} for $\alpha = 5°$ at $St_{l'} = 1.21$ 141
4.15 Phase-locked vorticity field with the streamlines superimposed over a complete acoustic pressure cycle during acoustic third mode excitation f_{a3} for $\alpha = 5°$ at $St_{l'} = 0.6$ 143

4.16 Single complete acoustic pressure cycle discretized at an arbitrary phase ϕ_a during third mode excitation f_{a3} for $\alpha = 5°$ at $St_{l'} = 0.6$ 144
4.17 Phase-locked vorticity field with the streamlines superimposed over a complete acoustic pressure cycle during acoustic third mode excitation f_{a3} for $\alpha = 10°$ at $St_{l'} = 0.29$ 145
4.18 Single complete acoustic pressure cycle discretized at an arbitrary phase ϕ_a during third mode excitation f_{a3} for $\alpha = 10°$ at $St_{l'} = 0.29$ 145
4.19 Phase-locked vorticity field with the streamlines superimposed over a complete acoustic pressure cycle during acoustic first mode excitation f_{a1} for $\alpha = 15°$ at $St_{l'} = 0.26$ 146
4.20 Phase-locked vorticity field with the streamlines superimposed over a complete acoustic pressure cycle during acoustic first mode excitation f_{a1} for $\alpha = 75°$ at $St_{l'} = 0.1$ 148
4.21 Phase-locked vorticity field with the streamlines superimposed over a complete acoustic pressure cycle during acoustic first mode excitation f_{a1} for $\alpha = 90°$ at $St_{l'} = 0.06$ 149
4.22 Hybrid experimental/numerical methodology implemented to compute the acoustic power production. 151
4.23 Instantaneous acoustic power (Π) calculated at two instants of the acoustic pressure cycle $\phi = 0°$ and $\phi = 180°$ respectively with the acoustic particle velocity U_a vectors superimposed (a, b); normalized net acoustic power over one pressure cycle ($\Pi h/U_\infty^3$) (c, d) during third acoustic mode excitation f_{a3} for $\alpha = 0°$ at $St_{l'} = 0.6$. 156
4.24 Instantaneous acoustic power (Π) calculated at two instants of the acoustic pressure cycle $\phi = 0°$ and $\phi = 180°$ respectively with the acoustic particle velocity U_a vectors superimposed (a, b); normalized net acoustic power over one pressure cycle ($\Pi h/U_\infty^3$) (c, d) during third acoustic mode excitation f_{a3} for $\alpha = 5°$ at $St_{l'} = 1.21$ 157
4.25 Instantaneous acoustic power (Π) calculated at two instants of the acoustic pressure cycle $\phi = 0°$ and $\phi = 180°$ respectively with the acoustic particle velocity U_a vectors superimposed (a, b); normalized net acoustic power over one pressure cycle ($\Pi h/U_\infty^3$) (c, d) during third acoustic mode excitation f_{a3} for $\alpha = 5°$ at $St_{l'} = 0.6$ 158
4.26 Instantaneous acoustic power (Π) calculated at two instants of the acoustic pressure cycle $\phi = 0°$ and $\phi = 180°$ respectively with the acoustic particle velocity U_a vectors superimposed (a, b); normalized net acoustic power over one pressure cycle ($\Pi h/U_\infty^3$) (c, d) during third acoustic mode excitation f_{a3} for $\alpha = 10°$ at $St_{l'} = 0.29$ 159

A.1 Uncertainty of time-averaged flow velocity decomposed in the streamwise direction for the case of $AR = 2$ and $\alpha = 0°$ 185

Nomenclature

Symbol	Definition
St	Strouhal number
c	Speed of sound in air
H	Duct height
W	Duct width
f_{peak}	Frequency at peak resonance
f_a	Theoretically estimated acoustic frequency
P_a	Acoustic pressure
P_{rms}	Root mean square acoustic pressure
ρ	Density of air
Re	Reynolds number
C_p	Static pressure coefficient
SPL	Sound Pressure Level
PIV	Particle Image Velocimetry
$DEHS$	Di-Ethyl-Hexyl-Sebacat
α	Cylinder angle of incidince
$\vec{\omega}$	Vorticity
$F_{L(rms)}$	Root mean square of the lift force
AR	Aspect ratio
St_l	Strouhal number based on the rod streamwise length l
St_h	Strouhal number based on the rod cross-stream length l
$\overline{v'v'}$	Normal Reynolds stress
$\overline{u'u'}$	Shear Reynolds stress
a_n	Temporal coefficient,
λ_n	Eigenvalue of the POD mode

ψ_n	Spatial features
ϕ	Instantaneous flow field phase
$ILEV$	Impinging leading edge vortex shedding
$TEVS$	Trailing edge vortex shedding
P^*	Normalized acoustic pressure
$\vec{u}_a$	Acoustic particle velocity
k	Wave number
∇p	Acoustic pressure distribution

Chapter 1

Introduction

1.1 Problem overview

Fluid dynamics, an expansive field, delves into an array of processes, including the examination of the aerodynamics associated with bluff bodies - a phenomenon most of us inevitably engage with in our everyday lives, either indirectly or directly. The comprehensive understanding of bluff body flows has far-reaching implications, notably in the design process, aiding in the creation of efficient and effective structures, such as buildings, heat exchangers, bridges, and various transport vehicles.

Research that employs simple geometric configurations, such as rectangular and circular cylinders, is particularly valuable. These uncomplicated forms allow for an in-depth exploration of intrinsic features of flows, including vortex formation regions and separation bubbles. Such insights are invaluable for elucidating the intricate flow phenomena associated with more complex geometrical forms.

Rectangular cylinders are prominent in a range of industrial applications due to their unique characteristics and versatility. For example, these geometric forms are integral to the construction of trashracks at hydraulic intakes in hydropower plants.

Here, they serve a critical role as filters, preventing debris from entering and potentially damaging the intricate hydraulic systems. Another industry where rectangular cylinders play a pivotal role is its presence in gas turbine blades. These cylinders are positioned within the turbine's cooling channels where they function as vortex generators. The resultant effect is an increase in the turbulence levels, which in turn boosts the heat transfer process. This enhanced heat dissipation allows the turbine blades to maintain a cooler operational temperature, thus mitigating the risk of overheating and damage. This effective cooling mechanism not only preserves the longevity of the turbine blades, but also elevates the overall efficiency of power generation. It underscores the transformative potential that simple geometric forms like rectangular cylinders can have in complex industrial applications, ultimately driving advancements in power production and resource optimization.

In recent decades, experimental investigations of flow over two-dimensional rectangular cylinders have paved the way for significant breakthroughs in our grasp of several flow phenomena. Notably, it has enhanced our comprehension of turbulence's impact on the separating shear layer, the fundamental properties of the separated flow region near the leading edge, and the influence of controlled flow perturbations on vortex shedding and heat transfer. The furtherment of this understanding contributes to ongoing advancements in the field of fluid dynamics and helps us furthermore understand the complex flow phenomenon that arise as a result of the interaction of a moving fluid with a bluff body.

1.2 Motivation

Despite the substantial body of research focused on the mechanism of flow-sound interaction for cylindrical structures subjected to cross-flow, surprisingly, the flow-

acoustic coupling from rectangular rods in a similar setting has not been accorded the same level of scrutiny. This is noteworthy given the prevalent use of these structures in various industrial applications.

The processes of flow separation and reattachment occurring around rectangular rods subjected to cross-flow exhibit fundamental differences when compared to those around circular cylinders. Such distinctions in flow behaviour can significantly influence the resulting aeroacoustic phenomena and the dynamics of flow-acoustic interactions.

Furthermore, the shape of the corners in rectangular rods, whether they are sharp, chamfered, or rounded, can profoundly affect the flow separation mechanism. By extension, these variations can also impact the coupling between the fluid flow and an acoustic mode. Thus, understanding these intricacies and their implications for flow-acoustic coupling in rectangular rods in cross-flow is critical, and the dearth of research in this area suggests a substantial knowledge gap that this study aims to address.

1.3 Objectives

The primary objective of this thesis is to undertake an exhaustive exploration of the behavior of the shear layer and flow topology around rectangular cylinders under both non-resonant and flow-excited acoustic resonance conditions, and for various configurations. This research endeavors to build upon the work of [114], who examined the flow characteristics and aeroacoustic response of rectangular cylinders with varying aspect ratios. Their research revealed the existence of a minimum rod length in the flow direction that prompts an early excitation of higher acoustic modes. To delve deeper into and expand upon these initial findings, this work will focus on several key

areas.

Firstly, the effects of aspect ratio will be examined under both resonant and non-resonant conditions, aiming to identify and understand any variations or anomalies. Secondly, the investigation will delve into the hydrodynamic loading experienced by rectangular cylinders of different aspect ratios, again under both resonant and non-resonant conditions, to illuminate the influence of these states on the structures' interaction with the flow. Thirdly, the study will select a particular aspect ratio and investigate the impact of various edge roundings on the flow topology and the interaction between flow and sound. By doing so, it hopes to determine how these changes may influence the aeroacoustic characteristics of the cylinder. Lastly, this thesis will probe the role of the angle of incidence in magnifying different shedding modes under non-resonant conditions or during self-excited acoustic resonance. By analyzing these factors, this research aims to comprehensively understand how these variables influence the complex interplay of flow dynamics and acoustics around rectangular cylinders.

1.4 Thesis outline

This thesis is divided into 5 chapters and the chapters are divided as follows

1. Chapter 1: Gives an overview of the problem and the motivation and main objectives of this study.

2. Chapter 2: The second chapter of this work presents a comprehensive literature review, summarizing the vast research efforts undertaken to understand the dynamics of flow around rectangular and square cylinders. This body of work is extensive and spans several decades, highlighting the scientific community's

interest and persistent efforts in understanding and predicting the intricate behavior of flow around these geometric structures.

Beginning with early empirical investigations, the literature review traces the evolution of our understanding, moving through theoretical developments, experimental studies, and advancements in numerical modeling techniques. These studies have progressively deepened our comprehension of the flow characteristics around rectangular and square cylinders, including the fundamental mechanisms of flow separation, vortex formation, wake behavior, and associated acoustic phenomena.

Considerable attention is given to the effects of aspect ratio and edge roundings, and their influences on the cylinder's aerodynamic and aeroacoustic responses. A rich array of studies investigates how these geometric modifications alter the flow separation points, vortex shedding frequencies, and the structure of the wake region, among others.

The literature review also discusses the impact of external forcing conditions, particularly the role of resonant and non-resonant conditions, on flow dynamics. It elucidates the nature of flow-excited acoustic resonance and its influence on the flow topology and hydrodynamic loading of the cylinders.

3. Chapter 3: First journal article published in the Journal of Fluids and Structures, which addresses the first objective provides a comprehensive exploration of various aspects of the studied phenomena. This includes an in-depth analysis of the aeroacoustic response of rectangular cylinders with different aspect ratios and edge roundings. Through careful evaluation, it sheds light on the effects of these variations on acoustic generation.

   This chapter quantifies the hydrodynamic loading under resonant and non-

resonant conditions. It meticulously assesses how these conditions influence the forces acting on the cylinder due to the flow, offering insights into the changes in loading patterns and their implications for design and performance.

Lastly, the chapter utilizes flow visualization techniques during both resonant and non-resonant conditions to delve into the alterations in shear layer behavior and wake topology under resonance. By investigating the changes in flow behavior and structure, it further enhances our understanding of the complex interplay between flow dynamics, structural characteristics, and acoustic resonances.

This multi-pronged approach provides a comprehensive and detailed picture of the effects of aspect ratio, edge rounding, and resonant conditions on the aeroacoustic and hydrodynamic characteristics of rectangular cylinders in cross-flow. The findings detailed in this chapter lay a strong foundation for subsequent chapters.

4. Chapter 4: Second journal article submitted to Journal of Fluid Mechanics, which delves into the complex interplay between acoustic resonance perturbations and angle of incidence in affecting shear layer instability and vortex shedding patterns within the wake of rectangular cylinders. This analysis furnishes critical insights into the mechanisms underpinning these patterns and how they are influenced by a range of operational and geometrical conditions, thereby expanding our understanding of the flow dynamics around such bodies.

5. Chapter 5: The final chapter of this work synthesizes the findings from the previous chapters and offers an executive conclusion, elucidating the significant implications of the results. Moreover, it provides recommendations for future studies, outlining potential avenues for further advancing the understanding of

flow dynamics around rectangular cylinders.

Chapter 2

Literature review

2.1 Bluff body aerodynamics

Fluid dynamics around bluff bodies are markedly different from those around streamlined structures. This divergence primarily arises from the prevalence of separated and often reattaching flow regions in bluff bodies, the relatively high drag coefficient (C_D), and the manifestation of vortex shedding. These characteristics render bluff bodies a frequent occurrence in engineering-related fluid movements. Investigations into fluid behavior around basic shapes, such as circular cylinders, prisms of varying cross-sections, and inclined aerofoils, have significantly bolstered our understanding of many fundamental aspects of fluid dynamics related to bluff bodies over the past half-century. This knowledge enrichment not only illuminates the complex dynamics of fluid flow around these simpler shapes, but also paves the way for more advanced studies involving intricate geometries and more complex flow scenarios.

2.1.1 Vortex shedding

The phenomenon of vortex shedding typically appears for Reynolds number (Re) values exceeding 50 when dealing with bluff bodies. This can lead to significant structural vibrations, which in extreme cases can result in catastrophic structural failure or more commonly, fatigue failure. Furthermore, vortex shedding can also act as a source of undesired noise. Historically, Strouhal was the first to identify the relationship between the frequency of the sound generated (known as the aeolian tone), the velocity of the flow, and the diameter of the cylindrical wire that the flow traverses [123]. He formulated this relationship as a non-dimensional constant, expressed as $St = f_s d/U_\infty$, where 'fs' represents the frequency of the sound, 'd' is the wire diameter, and 'U_∞' denotes the flow velocity. This constant, now widely recognized as the Strouhal number, serves as a key metric in the study of fluid dynamics and vortex shedding phenomena.

Subsequently, Bernard (1912) [10] further elucidated that the aeolian tone is actually a consequence of the vortex shedding phenomenon occurring in the wake of bluff bodies. In the same year, Von Karman introduced a criterion for establishing stable vortex shedding. He postulated that the ratio of the spacing between vortices along the transverse direction (spanned by the two shear layers)(a) to the streamwise distance between vortices emanating from the same shear layer (h) should maintain a value of $a/h = 0.28$ [136]. A visual representation is shown in figure 2.1. The shedding pattern that emerged from this configuration was then named by Von Karman as "Kármán vortex streets". This pioneering work marked a significant step forward in our understanding of fluid dynamics, setting a foundation for much of the modern work in this field.

Roshko 1955 [102] identified a remarkable similarity among bluff body flows across diverse geometries. His work centered on the investigation of the pressure recovery

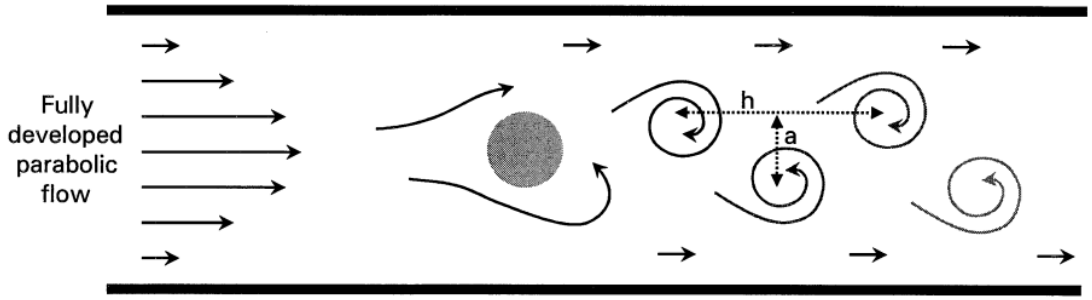

Figure 2.1: Visual representation of Von Kármán vorticies and the spatial spacing between adjacent vorticies .

mechanism inherent in reattaching flows. Remarkably, he discovered that the pressure distributions for all examined shapes coalesced onto a singular curve when the pressure was normalized by the pressure at the point of separation, and the streamwise displacement was normalized by the length of reattachment.

In a comprehensive investigation of flow over rectangular cylinders, Bearman (1967) [7] made significant strides in our understanding of this complex phenomenon. One of his main discoveries was the convergence of data when plotting the base pressure parameter, represented as $K = (1 - Cp_b)^{0.5}$, against the universal Strouhal number St_b, expressed as $S_b = fb/U_b$. Here, U_b stands for the velocity at the point of separation, f denotes the frequency of the observed vortex shedding pattern, and b refers to the streamwise distance between the shed vortices. Furthermore, his findings emphasized on the accuracy of the von Kármán vortex street drag formula in predicting the convective velocity of the vortices and the streamwise spatial distance between adjacent vortices.

2.1.2 Flow instabilities

The study of fluid dynamics has revealed several types of naturally occurring flow instabilities that are of critical relevance to engineering applications. These include

instabilities in free shear layers, bluff body shear layers, impinging shear layers, vortex street wakes, and boundary layers transitioning to turbulence. Lately, with advancements in computational power and computational fluid dynamics turbulence models, the field of linear stability analysis has garnered renewed attention, significantly contributing to our understanding of the mechanisms that lead many flows to instability. The primary objective of conducting a linear stability analysis is to assess the stability of a given flow pattern, providing predictions about the onset of any flow instability. However, it's crucial to note that linear stability analysis offers predictions that primarily apply to the early stages of instability. As the instability intensifies and the flow pattern alters, it quickly transitions into the realm of non-linearity. Thus, while a linear stability analysis provides valuable insights into a flow's initial destabilization, it cannot capture the full complexity of the evolution of flow instabilities.

Flow instabilities can be classified in different ways. Two of the key distinctions are whether an instability is local or global, and whether it is absolute or convective.

Local instabilities pertain to disturbances that grow locally in space and are mainly linked to properties of the flow at a particular location. In contrast, global instabilities involve growth in disturbances that interact with the entire flow field, regardless of their local origin, often leading to larger-scale modifications in the flow structure. A classic example of local instability is the Kelvin-Helmholtz instability that manifests at the boundary between two fluids or gas layers with different velocities [18]. This often causes the formation of waves or vortices at the interface, for instance, the ripples we see on the wind-blown water surface or the wavy structure of certain clouds. An example of global instability can be seen in the transition to turbulence in pipe flow, where a disturbance at one location can affect the entire flow, leading to globally chaotic behavior [27]. Another instance is the transition to chaotic convection in a fluid heated from below (Rayleigh-Bénard convection), where a small temperature

fluctuation can trigger a global reorganization of the convective cells.

In terms of absolute and convective instabilities, they differ in terms of how disturbances propagate through a system. Absolute instabilities are those in which disturbances grow in place and amplify both upstream and downstream. This is commonly observed in wake flows behind bluff bodies, where an absolute instability can cause an upstream influence, leading to the oscillation of the wake and the generation of vortex streets. On the other hand, convective instabilities are those in which disturbances grow while being convected downstream. This is typical of shear layers, such as the boundary layer on a flat plate, where perturbations can grow and eventually lead to turbulence, but they do so while being transported downstream, without having an effect on the upstream flow [47].

Figure 2.2 provides a graphic representation of how a system typically reacts to an impulse disturbance. The left panel showcases an absolutely unstable system. On the other hand, the right panel depicts a convectively unstable system. Briggs (1964) [14] utilized plasma instabilities as a tangible mechanism to elucidate the dynamics of absolutely unstable systems. He demonstrated that when an impulse, or a disturbance with a small amplitude acting within a finite time period, is applied to such systems, it triggers an exponential growth of the disturbance at its source. This exemplifies the fundamental characteristic of absolute instability, where perturbations proliferate rapidly and impact the entire system. Conversely, for convectively unstable systems, the impulse disturbance is carried away from the disturbance source due to the inherent convection properties of the system. Over time, this leads the system to revert back to its original state, showcasing the temporary nature of disturbances in convectively unstable systems. In the context of shear flows without downstream impingement surfaces, Rockwell (1990) [99] suggested that a region of absolute instability is essential for the existence of global instabilities. An archetypal example of

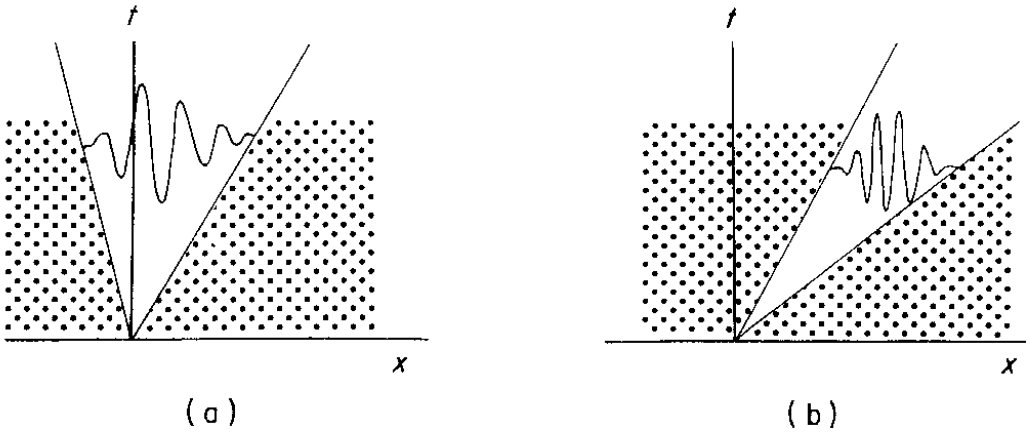

Figure 2.2: Schematic sketch that depicts an impulse response (a) absolutely unstable flow; (b) convectively unstable flow [74]

a globally unstable flow is the wake behind a bluff body, attributed to the presence of an absolute instability region within the wake itself. However, the dynamic shifts when a downstream impingement body is introduced into a convectively unstable shear flow. This additional element can generate a feedback loop, instigating global instability. The process works through the provision of upstream feedback from the downstream surface to the shear layer at the upstream separation edge [81].

The characteristics of convectively unstable flows have been deeply studied, and such flows have been found to exhibit a high degree of sensitivity to external perturbations that span a broad range of frequencies, thereby earning the label of "noise amplifiers." For instance, Ho & Huerre 1984 [39] research sheds light on the mixing layer as an exemplar of convectively unstable shear flows. His findings underline the extreme susceptibility of the shear layer to externally applied disturbances. Similarly, the research conducted by Parker & Welsh (1983) [94] on rectangular cylinders with a long streamwise length showcases another instance of such behavior. Their study identified that the instability of the separated shear layer can synchronously lock with a transverse duct acoustic mode, demonstrating the effect of external perturbations on

the flow characteristics. Building on these foundational insights, subsequent research by Soria & Wu (1992) [119] further corroborated these findings. They demonstrated that the process of shear layer separation from the trailing edge of rectangular cylinders, followed by reattachment on the lateral face, is indeed indicative of convectively unstable flow.

Merati & Adrian (1992) [66] conducted an exploration into the mechanism that magnified inherent instabilities in a planar shear layer as it collided with a downstream object. They discerned that the positioning of a slender, planar piece in the shear layer's centerline, precisely within the area experiencing exponential growth, generated cyclical disturbances that reverberated upstream to the initial destabilization. The fluctuations in the shear layer's magnitude—either intensifying or lessening—were contingent on the gap between the separation splitter plate and the downstream plate. Optimal amplification transpired when the interval separating the feedback edge from the separation splitter plate's edge was commensurate with a whole-number multiple of the initial instability frequency's wavelengths.

Wake flows that are globally unstable owing to an absolute instability region in the wake show self-induced oscillations and can be classified as oscillators [74]. Due to the inherent self-induced instability, they typically show indifference to low-amplitude disturbances. Only when perturbations are introduced with enough intensity to substantially modify the mean flow, can the flow be influenced by externally applied disturbances.

A classic example of globally unstable flows is the Kármán vortex shedding street seen in the wake of circular cylinders. In this scenario, the wake forms a region of absolute instability, while the separated shear layers demonstrate convective instability. This phenomenon exemplifies the intricate interplay between these two types of instabilities in governing the flow characteristics around bluff bodies. Karniadakis

& Triantafyllou (1989) [55] conducted a numerical investigation into the impact of external periodic forcing on flow instability. As depicted in Figure 2.3, the lock-in boundary delineates the graph into two parameter regions, creating a parabolic shape. When a perturbation of minimal amplitude is applied at a frequency resonating with the Kármán vortex shedding street, the vortex shedding remains unaffected. However, if the amplitude of this perturbation exceeds a certain threshold, the wake frequency synchronizes with the perturbation frequency, a phenomenon known as lock-in. If the perturbation frequency is applied outside the receptive boundary, the ensuing near frequency matches the vortex shedding frequency. Interestingly, when the perturbation frequency falls within the range between the lock-in boundary and the receptivity boundary, a quasi-periodic wake results. This quasi-periodic state features both the perturbation frequency and the inherent shedding frequency within the wake. For rectangular cylinders with aerodynamic leading edges and sharp trailing edges, a similar behavior as of the circular cylinders is observed with a minimum threshold of the perturbation amplitude to be able to intrinsically alter the vortex shedding [120].

2.2 Flow around rectangular cylinders

Rectangular cylinders and geometries of similar nature are prevalent in various engineering sectors. These can be seen in architectural constructions like skyscrapers and the decking structures in bridges. In addition, they also find use in trash racks at the inlet of hydraulic intakes to prevent the entrance of debris and solid wastes.

One defining characteristic that differentiates flows around rectangular prisms from those around circular cylinders is the existence of a fixed separation point. This point is typically situated at the sharp leading edge corners of the prism. In

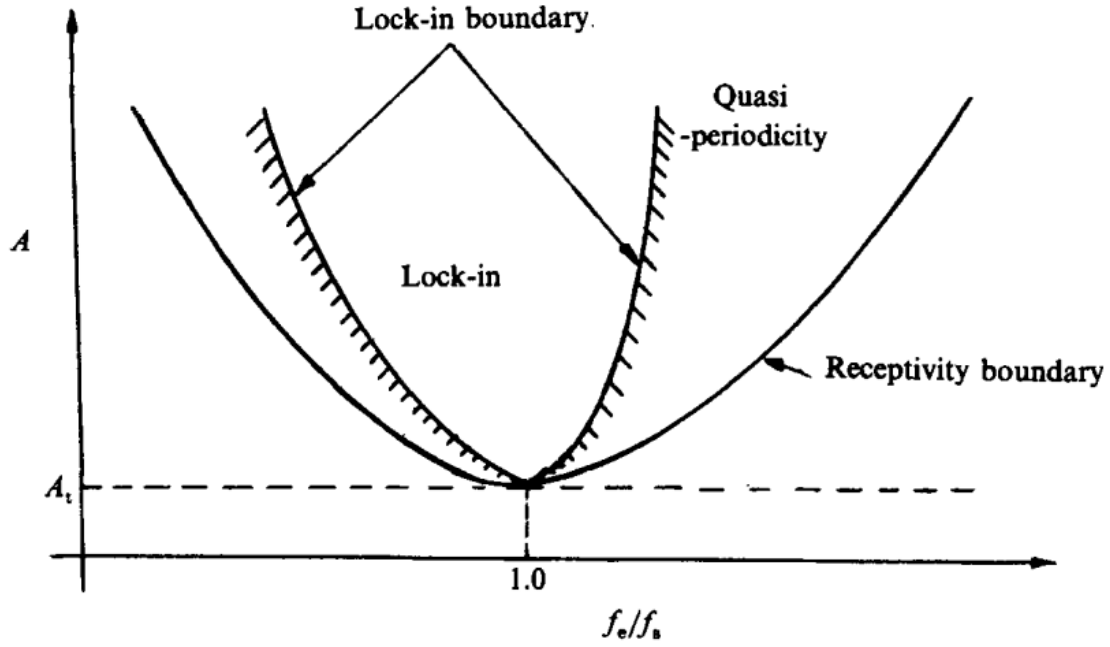

Figure 2.3: Stability map of state selection for laminar wakes [55]

contrast to rounded bodies like cylinders, where the flow separation point can shift along the curved surface, rectangular bodies have rigid boundaries that direct the flow in a specific manner. This factor significantly influences the behavior of the flow around these shapes, thereby impacting the related engineering parameters such as lift, drag, and vortex shedding patterns. Understanding these distinctive flow dynamics around rectangular prisms can provide valuable insights for optimizing their design and performance in the aforementioned applications.

The aerodynamics of rectangular cylinders are influenced by a variety of factors. The aspect ratio of the cylinder, defined as the ratio of the stream-wise length to the cross-stream length, significantly influences the behavior of the flow. It plays a pivotal role in the generation of wake patterns and large-scale structures in the fluid flow. Another critical factor is the Reynolds number, a dimensionless quantity that measures the ratio of inertial forces to viscous forces. It characterizes the nature of the

flow – whether it is laminar or turbulent – and heavily influences the vortex shedding patterns observed in the wake of the cylinder. Higher Reynolds numbers typically imply more turbulent flows, leading to complex shedding patterns and substantial large-scale vortex structures. The turbulence level of the incoming flow also plays a role. It impacts the dynamics of the shear layer, the region where the velocity of the fluid changes significantly. Higher turbulence levels can induce more instabilities in the shear layer, contributing to increased vortex formation and potential alterations to the flow behavior. Lastly, any external disturbances or vibrations induced in the cylinder can substantially modify the flow topology. For example, an oscillating cylinder might cause the vortex shedding frequency to synchronize with the cylinder's vibration frequency, a phenomenon known as lock-in. This synchronization can amplify the vibrations and cause substantial changes in the flow field.

2.2.1 Effect of the aspect ratio (AR) on the wake dynamics and hydrodynamic loading

The study of hydrodynamic loading on rectangular cylinders traces back to the work of Fage & Johansen (1927) [32]. They embarked on an investigation to measure the drag force exerted on a thin rectangular cylinder (possessing a notably low aspect ratio of $AR = 0.028$) at zero angle of incidence. Their results indicated that the drag coefficient remained approximately constant around the value of 2.0. Subsequent research sought to evaluate the drag coefficient of rectangular cylinders, and the prevailing assumption was that for square cylinders and those with moderate aspect ratios (specifically, $0.5 < AR < 2$), the drag coefficient would hover around 2. However, this assumption was later challenged by the findings of Nakaguchi et al. [75] in 1968. They reported a considerably higher drag coefficient of 2.8 for cylinders with

an aspect ratio of $AR = 0.62$, thus contesting the commonly held view. Examination of figure 2.5 and 2.4 offers valuable insights into the relationship between the Strouhal number and two critical parameters: the Reynolds number and the aspect ratio. In the high Reynolds number regime ($Re_d > 0.5x10^3$), the Strouhal number exhibits a rather insignificant dependency on the Reynolds number, indicating the influence of Reynolds number on the vortex shedding frequency is not very pronounced within this range. In contrast, a substantial dependency on the aspect ratio is clearly observed. As the aspect ratio increases, the Strouhal number follows a downward trajectory until the aspect ratio reaches a value of approximately 2. At this point, the curve experiences a noticeable inflection, with the Strouhal number suddenly escalating from 0.05 to 0.19. This abrupt change suggests a considerable alteration in the wake shedding topology, likely instigated by the reattachment of the flow onto the cylinder's lateral face. The implications of this shift are considerable, as it signifies a critical transition point in the flow dynamics around a rectangular cylinder. Further examination of the data presented in Norberg (1993) [82] study (as shown in Figure 2.4), reveals a decreasing trend for the drag coefficient with increasing aspect ratio. This trend persists until the aspect ratio reaches a value of 5, at which point the drag coefficient stabilizes around 1. Hence, these findings highlight the dynamic nature of the drag coefficient for rectangular cylinders, demonstrating its dependence on the aspect ratio and challenging earlier assumptions about its consistency.

Bearman (1967) [7] introduced the concept that a reduction in base suction pressure is a consequence of an extended vortex formation length, which subsequently translates into diminished drag force exerted on the cylinder. Further elaborating on this notion, Bearman & Trueman (1972) [9] provided an explanation for the remarkable surge in the C_d value for an aspect ratio $AR = 0.62$. According to their research, this spike is linked to a critical afterbody length, beyond which the afterbody be-

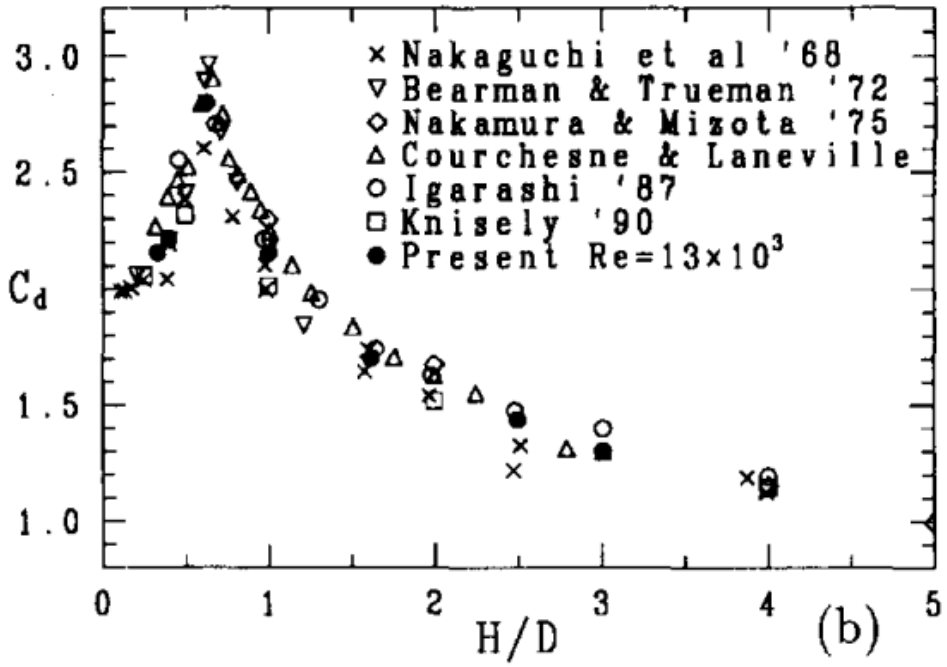

Figure 2.4: The variation the drag coefficient C_d with different aspect ratios AR [82]

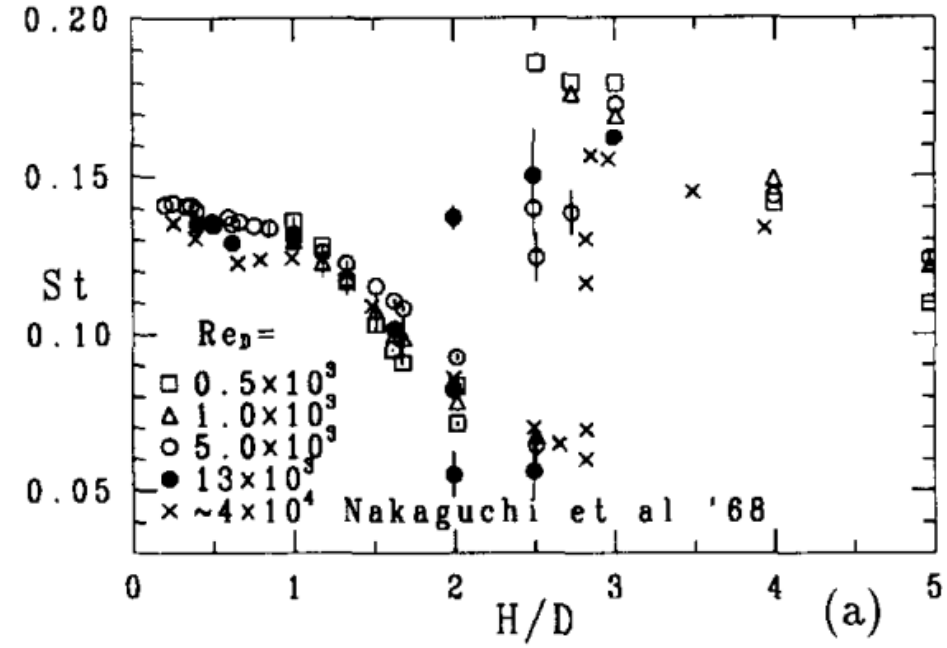

Figure 2.5: The variation of Strouhal number St with different aspect ratios AR [82]

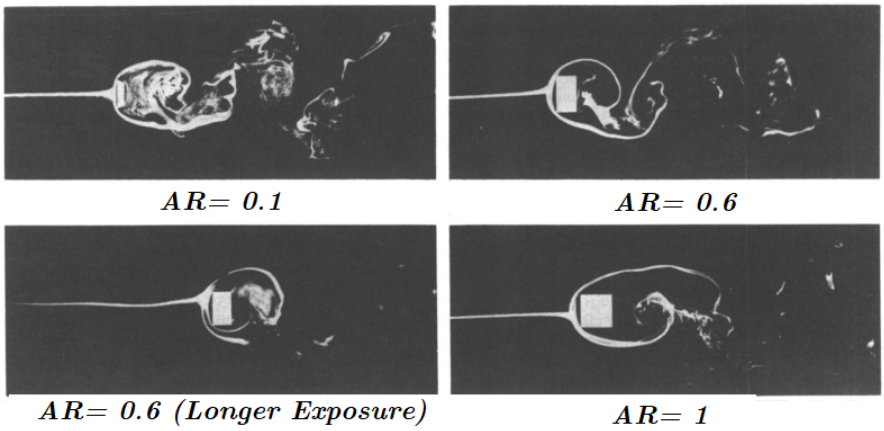

Figure 2.6: Flow around rectangular cylinder of different aspect ratio filmed using dye filament in a water tunnel (Adapted from [9])

gins to interact with the vortex formation process. This can be seen in figure 2.6, where for $AR = 0.6$ the vortex formation tends to occur very close to the base of the cylinder, leaving behind a minimal area of flow separation. This means the region where the flow detaches from the body of the cylinder, creating a zone of turbulence and reduced pressure. For streamwise lengths falling below this threshold, the vortex formation length remains constant and unaffected, being determined primarily by the leading corners. However, when the aspect ratio reaches around $AR = 0.6$, a complex interplay begins to emerge between the separated shear layer originating from the cylinder's leading edge and the trailing edges. As the aspect ratio further increases, the vortex formation length no longer remains independent of the streamwise length but instead, it becomes closely associated with the position of the trailing edge. This intricate dynamics lead to a significantly enhanced base suction, which in turn contributes to a downward trend in C_d, culminating in a value of approximately 1 when the aspect ratio is around 5.

2.2.2 Effect of Reynolds number on the separated shear layer

In case of elongated rectangular cylinders, the separated shear layer from the leading edge always reattach to the cylinder lateral face. The prononced shedding pattern in the wake is highly dependent on the Reynolds number in the low range ($Re < 380$). Sasaki & Kiya (1991) [109] identified three ranges for the separated shear layer regime based on the Reynolds number.

1. In the Reynolds number range of $80 < Re_h < 320$, the shear layer that separates from the leading edge maintains its laminar characteristics until it reattaches. Nonetheless, due to the prevalence of viscous forces, the shear layer is prevented from rolling up to form a distinct vortex. In this range, the flow behavior is mainly dictated by viscous effects, which suppress the instabilities necessary for vortex generation, resulting in a flow pattern that lacks well-defined vortical structures.

2. In the Reynolds number range of $320 < Re_h < 380$, the Kelvin-Helmholtz (K-H) instability becomes prominent in the shear layer, enabling the creation of distinct inverted V-shaped vortices. These vortex structures are distributed evenly across the span length of the cylinder, as illustrated in figure 2.7(a). Interestingly, within this range, an inverse correlation is observed between the size of the separation bubble and the Reynolds number. As the Reynolds number increases, the size of the separation bubble tends to decrease, indicating a greater influence of inertial forces over viscous forces within this regime. This shift in dominant forces encourages the development of instabilities and, subsequently, the formation of more complex flow structures.

3. In the Reynolds number range of $Re_h > 380$, the vortical structure formed impose a horseshoe topology resulted from the coalescence of vorticies. As

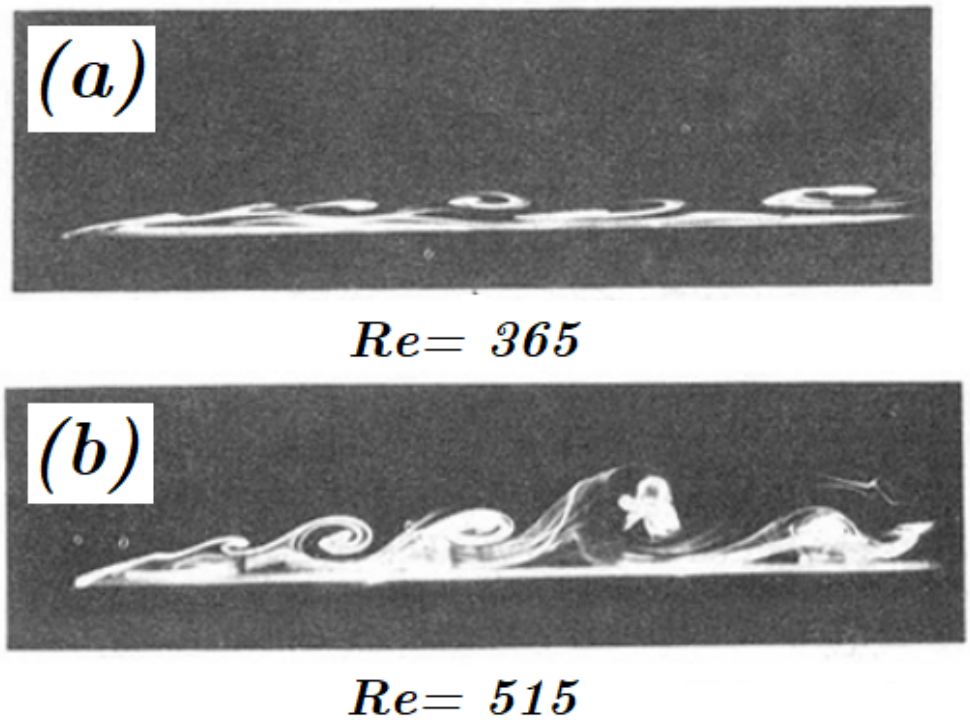

Figure 2.7: Side view of the vorticies downstream (a) $320 < Re_h < 380$; (b) $Re_h > 380$ (Adapted from [109])

shown in figure 2.7(b) the vorticies are spread on the cylinder lateral face in a staggered arrangement.

At high Reynolds numbers ($Re_h > 380$), the shear layer separating from the leading edge takes on a more streamlined, thinner form and accelerates its roll-up into the wake. Additionally, the process of vortex coalescence intensifies, proceeding more rapidly. This stage can be identified as the transition from a laminar shear layer to a turbulent one. As the Reynolds number continues to increase, the transition point, or the location where the shear layer shifts from laminar to turbulent behavior, moves closer to the leading edge. When Re_h reaches approximately 2×10^4 [88], the shear layer immediately becomes fully turbulent upon separating from the leading edge. This progression towards turbulence implies increasing flow complexity, potentially

influencing the aerodynamic forces acting on the rectangular cylinder.

Numerous studies have indicated that at high Reynolds numbers ($3.4\times10^4 < Re < 8\times10^4$) and under conditions of low incoming turbulence intensity, the behavior of the separated shear layer exhibits independence from the Reynolds number [38, 94]. In these conditions, the reattachment length of the shear layer (S_r) has been observed to depend solely on the cross-stream dimension of the rectangular cylinder. More specifically, it's noted that S_r equates to approximately $4.9h$, where h represents the cross-stream length.

The development of the separation bubble length resulted from the shear layer is said to be divided into two fragments. The first fragment, which resembles the first 60%, is analogous to plane mixing layer with a linear thickness growth. However, the remaining 40% are affected by the shear layer impingement (reattachment) to the cylinder surface. The vorticies reduced frequency (f_c) is found to be function of the free stream velocity (U_∞) and the reattachment length of the shear layer (S_r) following the relation ($0.6U_\infty/S_r$). Moreover, the spatial streamwise distance between adjacent vorticies is estimated to be a fraction of the reattachment length approximated to $0.75S_r$ [38, 56].

In the literature, the phenomenon of "shear layer flapping" has been frequently reported. This activity, which happens downstream of the leading edge, involves the shear layer undulating or "flapping" at a relatively low frequency. This behaviour is often linked to the formation of a large-scale, unsteady separation bubble in the flow. The presence of this bubble can lead to markedly elevated suction pressures beneath the bubble, which can significantly influence the dynamics of the flow and the forces exerted on the bluff body [21, 103].

2.2.3 Approaching flow turbulence level effect

Free stream turbulence, or the turbulence level in the flow approaching a body, can indeed have a significant influence on bluff body flows. The free stream turbulence can modulate these flow features in several ways such as altering wake dynamics, destabilizing the separated shear layer, and affecting the hydrodynamic loading on the bluff body.

Vickery (1966) [135] comprehensive examination of square cylinders 1966 yielded a notable finding concerning the connection between aerodynamic drag and free stream turbulence. His research indicated an inverse relationship between the two: as the intensity of free stream turbulence increased, aerodynamic drag on the square cylinder was found to decrease. Contrasting Vickery's findings, Bearman (1971) [9] study on cylinders with aerodynamic leading edges and small cross-stream lengths uncovered a distinctly different relationship. Instead of an inverse correlation, Bearman observed that an increase in free stream turbulence intensity led to an augmentation in aerodynamic drag on the studied cylinders. Gartshore (1973) [34] shed further light on this debate, indicating that the relationship between aerodynamic drag and turbulence is not solely dictated by the overall turbulence intensity. He discovered that the presence of small-scale vortical structures also played a significant role in shaping the topology of the separated shear layer. These structures imbued additional vorticity to the flow, thereby amplifying turbulent mixing. Hence, the contrasting results found by Vickery and Bearman in relation to the connection between turbulence intensity and the drag coefficient can be attributed to the differing geometries of their respective studies. While Vickery focused on square cylinders, Bearman utilized thin cylinders in his research. This alter the radius of the shear layer curvature which in turn shifts the reattachment point and, hence, the drag force.

Hillier & Cherry (1981) [38] investigated the relation between the turbulence in-

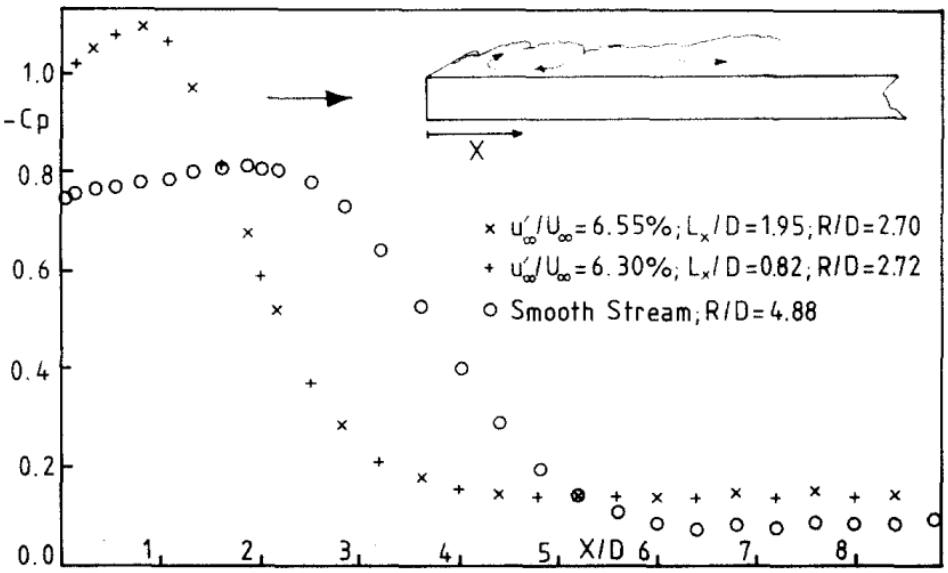

Figure 2.8: Mean pressure variation at different approach turbulence intensities (σ_u/u) (Adapted from [38])

tensity σ_u/u of the approaching free stream and the pressure distribution on elongated rectangular cylinders. As shown in figure 2.8, there is a strong dependence on the turbulence intensity.

Kiya & Sasaki (1983) [56] first an inverse relation between the turbulence intensity and the reattachment length. This was confirmed later by Saathoff & Melbourne (1997) [104] as they found an increase in the turbulence intensity can yield to a significant decrease in the reattachment length. This can be seen in figure 2.9 which reports an increase from zero to 6.5 % in the turbulence intensity can yield into almost reducing the reattachment length to half its value. Moreover, they discovered a relationship between turbulence intensity and the correlation of the vortices shed in the wake, leading to an increase in pressure fluctuations. This can be attributed to two key factors. The first is the amplification of vorticity coherence as the shear layer rolls into the wake. The second factor is the extended time window available to the shear layer due to the decreased frequency of the perturbation. This extra time

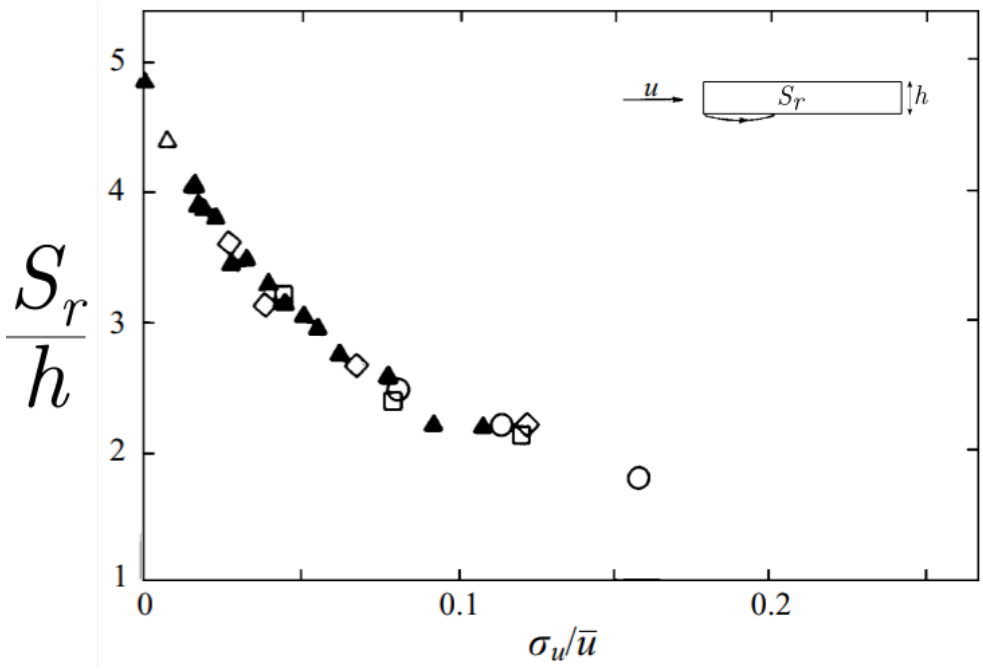

Figure 2.9: Reattachment length (S_r) variation at different approach turbulence intensities (σ_u/u) (Adapted from [104])

allows the shear layer to entrain more flow, thereby elevating the vorticity content.

2.2.4 Shedding patterns and flow instabilities for elongated cylinders

Vortex shedding from rectangular cylinder with different aspect ratios

The vortex shedding process from free streams interaction with bluff bodies is distinguished by Kármán shedding. This shedding pattern is the direct outcome of the mutual induction between the two detached shear layers. When considering vortex shedding from rectangular cylinder at relatively high Reynolds numbers (i.e., $Re_h > 10,000$), Parker and Welsh (1983) [94] classified the process into four distinct regimes. This classification is contingent on the aspect ratio of the cylinder ($AR = l/h$).

1. Regime (I): For rectangular cylinders of $AR < 3.2$, typical vortex shedding with the a separated shear layer from the leading edge rolling into the wake with no observable interaction (reattachment) with the streamwise length of the cylinder.

2. Regime (II): For rectangular cylinders of $3.2 < AR < 7.6$, the separated shear layer reattaches exactly at the trailing edge at a frequency equals to the global shedding frequency. The separation bubble envelope starts at the trailing edge with the vorticies shedding within the the vortex formation length.

3. Regime (III): For rectangular cylinders of $7.6 < AR < 16$, the seprated shear layer reattaches to the lateral face of the cylinder between the leading and trailing edge. The location where the shear layer reattaches mainly depends on the aspect ratio. A separation bubble is formed at the point of reattachment. Vorticies spread out along the span of the cylidner within the boundary layer in an unpredictable manner producing a random shedding street which can not be designated as Kármán shedding.

4. Regime (IV): For rectangular cylinders of $AR > 16$, Same as Regime (III) in terms of the shear layer separation and reattachment. However, the main difference is that the vorticies which forms within the boundary layer disseminate before reaching the afterbody wake past the trailing edge.

Figure 2.10 illustrates the variance of the Strouhal number (St_h) with the cylinder aspect ratio at high Reynolds numbers ($Re_h > 10,000$). The curve clearly delineates discrete regions, corresponding to the different regimes identified later. From 0 to $AR = 1$, the Strouhal number remains roughly constant at around 0.13. Following that, the Strouhal number starts to decline, reaching a value of 0.065 at $AR = 3.2$. This point marks a significant leap in the Strouhal number to a value of 0.15,

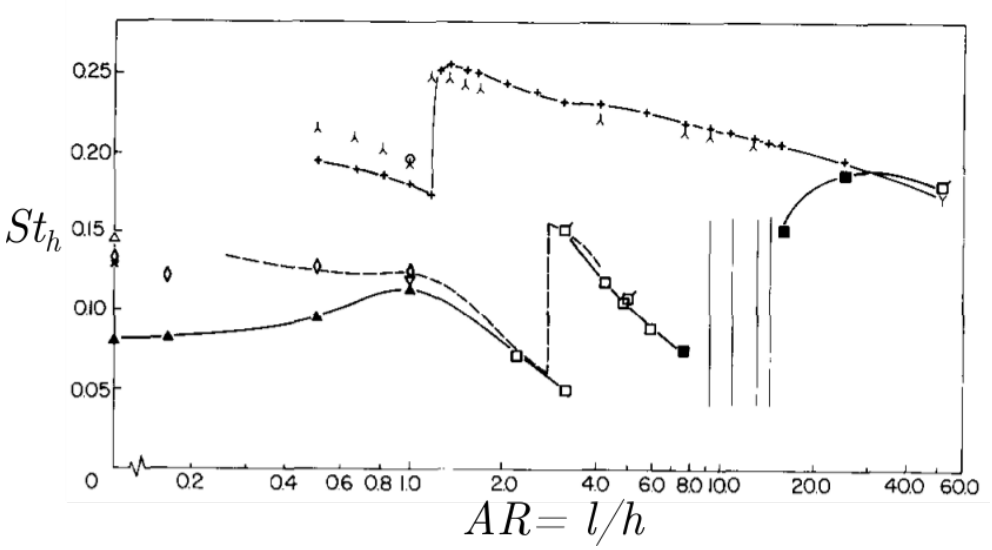

Figure 2.10: Strouhal number (St_h) VS the cylinder aspect ratio (l/h) (Adapted from [94])

indicating the onset of regime (II). The Strouhal number then begins to decrease again until it reaches a value of 0.07 at $AR = 7.6$. A discontinuity in the curve follows, indicating regime (III), where no regular shedding street is observed. Beyond $AR = 16$, the periodicity of the Strouhal number begins to reemerge, achieving a value similar to those seen in aerodynamic leading edge airfoils with the same streamwise length. This similarity underscores the idea that the shedding within this regime is indeed trailing edge shedding.

In studies conducted at comparatively low Reynolds numbers, Nakamura et al. (1991) [79] explored the Strouhal periodicity in the wake of rectangular cylinders with varying aspect ratios at a Reynolds number (Re_l) of 1000. A key finding of this study was the stepwise progression of the Strouhal number. The Strouhal number, when based on the streamwise length of the cylinder (St_l), was found to be an integral multiple of 0.6. In a subsequent investigation conducted at an elevated Reynolds number ($Re_l = 50,000$), Nakamura and Nakashima (1986) [77] analyzed the wake behavior of two distinct geometries, H-shaped and ⊢-shaped cylinders. These cylin-

ders had aspect ratios ranging from 2 to 8. Once more, the study revealed a stepwise evolution of the Strouhal number, reinforcing the previous findings at lower Reynolds numbers. One way to interpret this stepwise increase in St_l is to consider that an integer number (n) of vortices are always present along the streamwise length of the cylinder. The streamwise length decides the number of discrete vorticies materialize along the span of the cylinder. This pattern suggests that the plate length plays a key role in determining the spatial distribution and quantity of vortices formed along its side.

Figure 2.11 presents a vivid demonstration of the stepwise progression of the Strouhal number in relation to the aspect ratio. This progression is marked by jumps in the Strouhal number which occur in integer multiples of $0.6n$, where 'n' represents the quantity of vortices that have been shed from the leading edge and traveled along the length of the cylinder within a single global shedding cycle. Thus, the Strouhal number does not simply scale linearly with the aspect ratio, but shows this distinctive, quantized behavior, which suggests a close link between the geometry of the cylinder and the dynamics of vortex shedding.

The impinging leading edge vortex instability (ILEV)

Nakamura & Nakashima's (1986) [77] study pioneered the explanation for the pattern of vortex shedding observed in longer rectangular cylinders with aspect ratios greater than 3. They suggested that the shedding pattern is a manifestation of the instability of the shear layer, separated from the leading edge of the cylinder, known as the impinging shear layer instability. Naudascher & Rockwell (1994) [81] later refined this concept in , introducing the term "ILEV instability," which stands for "Impinging-Leading-Edge-Vortices instability." This terminology more accurately describes the phenomenon as, for cylinders with an aspect ratio exceeding 7, the separated shear

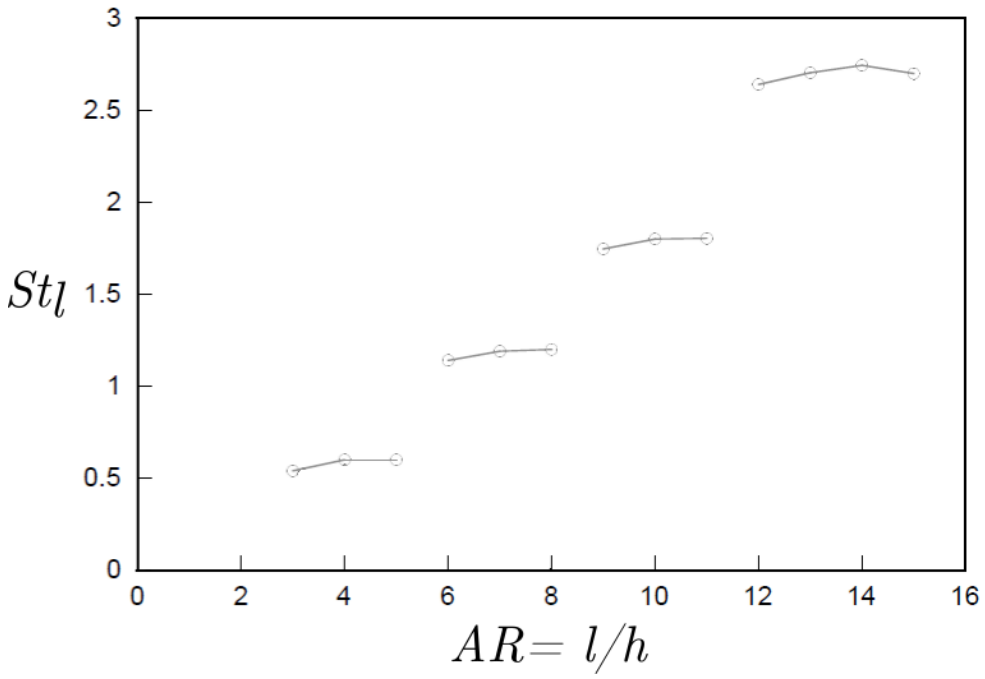

Figure 2.11: Strouhal number (St_h) VS the cylinder aspect ratio (l/h) at $Re_l = 1000$ (Adapted from [79])

layer from the leading edge does not directly interact with the trailing edge of the cylinder.

The concept of this shear layer instability is based on Rockwell & Naudascher (1978) [100] work for sharp-edged cavities. The flow over cavities is known to be self-sustained oscillation which can be divided into three categories outlined as follows:

1. Fluid dynamic oscillations: Hydrodynamic feedback mechanism materialize between the upstream and downstream corners.

2. Fluid resonant oscillations: Flow-acousitc coupling with an acoustic standing wave having a wavelength close to the cavity depth.

3. Fluid-elastic oscillations: Analogous to synthetic jets, an oscillatory motion is created without net mass flux, which is generated through the periodic inflow and outflow of fluid in a cavity by the oscillation of one of the cavity's walls

imposing a feedback loop of control on the shear layer separation.

Rockwell & Naudascher (1978) [100] focused their work on cavity flows that involve a feedback loop between the upstream and downstream edges via the separated shear layer. Contrasting this, Ho & Nozir (1981) [40] explored the interactions of impinging free jets on flat plates. They discovered that the shedding process is governed by two principal parameters: the large-scale vortices emanating from the free jet and the pressure waves generated as a result of these vortices impinging on the flat plate. As illustrated in figure 2.12, a pressure wave propagates upstream from the point of impingement. This pressure wave acts as a backpressure force on the free shear layer separating from the jet opening, promoting the coalescence of small-scale vortices into larger-scale vortical structures. This feedback mechanism helps maintain a phase lock between the jet opening and the flat plate, thus establishing a unique shedding process.

Figure 2.13 illustrates how the ILEV maintain a feedback loop. The seprated shear layer from the leading edge generates leading edge vorticies (LE). These vorticies are convected downstream. As it pass through the trailing edge it generates a pressure pulse which travels upstream of the cylinder to the upstream. As this pulse travels upstream this stimulate the leading edge to shed a new vortex closing the feedback loop between the leading and trailing edge. As we look at the nature of this mechanism, the vorticies wavelength is equal to the spanwise length of the cylinder. However, this explains the Strouhal number lock with a range of aspect ratios and then it jumps with an integar multiple. This jump resembles the materialization to an extra vortex within the spanwise length of the cylinder. This suggests that there is threhold values of the aspect ratios at which the shear layer impingement momentum generates a pressure pulse strong enough to shed extra vortex within the one complete shedding cycle.

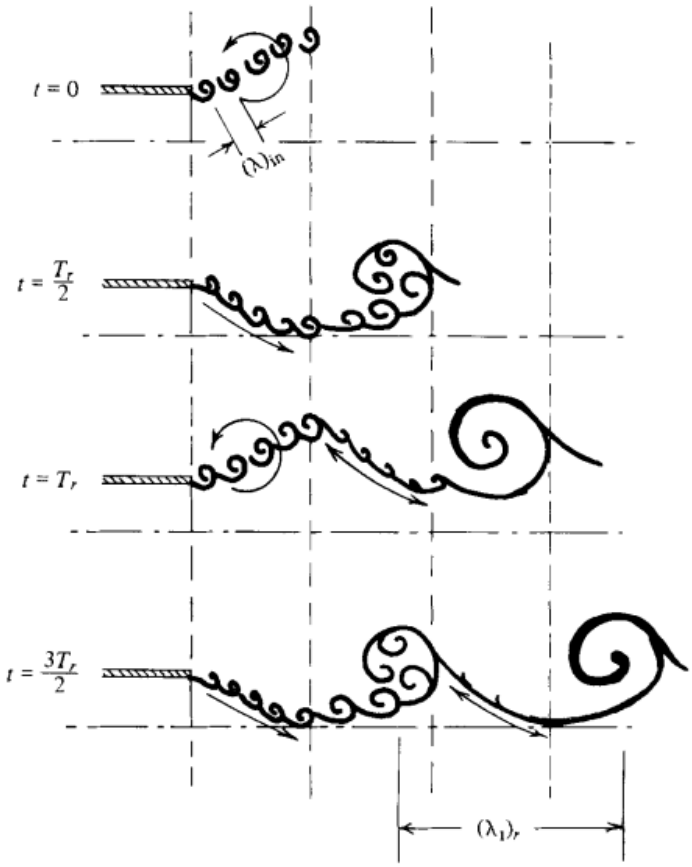

Figure 2.12: The process of coalescence of mixing layers small-scale vorticies into large-scale vorticial structure (Adapted from [40])

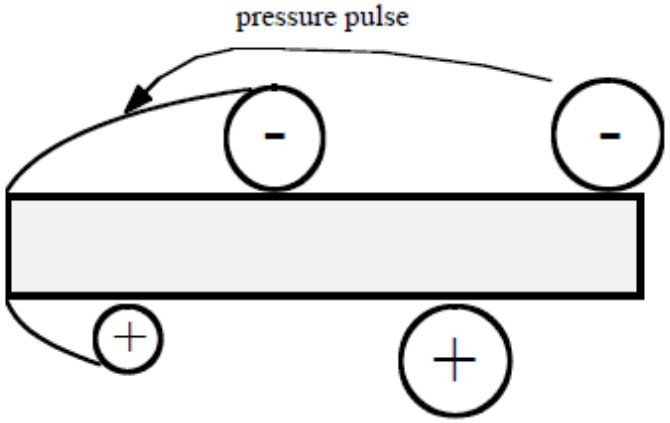

Figure 2.13: ILEV mechanism for an rectangular cylinder with $6 < AR < 9$ and $n = 2$ (Adapted from [67])

In order to delve deeper into the mechanisms underlying ILEV instability, Nakamura & Nakashima (1986) [77] conducted a study on H-section structures with an aspect ratio of 5, at high Reynolds numbers ($Re_h > 50,000$). The primary goal of this study was to determine whether this phenomenon was one or two-sided. To accomplish this, they compared wake frequencies in scenarios both with and without a splitter plate. Their findings indicated that the frequencies remained consistent in both cases, leading to the conclusion that ILEV instability is a one-sided phenomenon. This stands in contrast to natural vortex shedding, which relies on the mutual induction of counter-rotating shear layers. Another notable discovery was the absence of any distinct spectral peak in the Fast Fourier Transform (FFT) analysis of velocity fluctuation data obtained from a hot wire anemometer, at aspect ratios larger than 8. This absence of a spectral peak implies that no organized vortex-shedding pattern exists in the wake of these structures. These observations mirrored those reported by Parker & Welsh (1983) [94] for regular-shaped rectangular cylinders with similar aspect ratios.

One of the key discoveries made by Nakamura et al. (1991) [79] pertains to the absence of vortex shedding for cylinders with aspect ratios greater than 6 at relatively low Reynolds numbers ($Re_h > 2000$). As discussed earlier in this section, at such low Reynolds numbers, the shear layer transitions from a laminar state at the point of separation to a turbulent state approximately one cylinder cross-stream length downstream from the leading edge. However, the shear layer becomes turbulent at high Reynolds numbers immediately upon separation. This reduces the shear layer's sensitivity and susceptibility to both forced and natural perturbations. Furthermore, the influence of three-dimensional flow effects becomes more pronounced at high Reynolds numbers, which disrupts the feedback loop between the separated shear layer and the point of impingement.

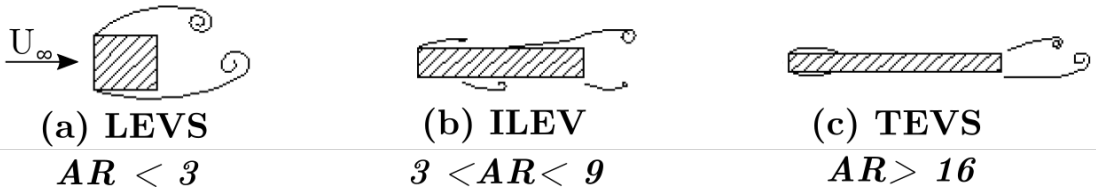

Figure 2.14: Vortex shedding patterns from rectangular cylinders with progressively increasing aspect ratio

Figure 2.14 outlines the three vortex shedding patterns than can materialize for rectangular cylinders at different ranges of aspect ratio. Type I, also known as Leading-Edge Vortex Shedding (LEVS), is characterized by the formation of a separation bubble at the leading edge of the body. Vortices form and shed from this separation bubble. Type II, referred to as Impinging Leading-Edge Vortex (ILEV) instability, involves the shedding of vortices from the separation bubble at the leading edge, which then interact with vortices forming at the trailing edge of the body. The dynamic interaction of these leading-edge and trailing-edge vortices forms a unique and complex shedding pattern. Type III, or Trailing-Edge Vortex Shedding (TEVS), involves the detachment of vortices directly from the trailing edges of the body. In this type of shedding, the influence of leading edge separation is less pronounced, and the primary dynamic feature of the flow is the shedding of vortices from the trailing edge.

In a bid to delve deeper into the ILEV shedding mechanism, Ohya et al. (1992) [91] carried out a 2-D CFD simulation on rectangular cylinders with aspect ratios ranging from 3 to 9. Their results generally agreed with the findings from Nakamura et al. (1991). However, discrepancies emerged for aspect ratios of 8 and 9. These differences can be primarily attributed to the 2-D nature of the CFD simulations, which may not fully capture the dynamics of the flow field at these Reynolds numbers where the flow is anticipated to be three-dimensional. This limitation may alter the predicted

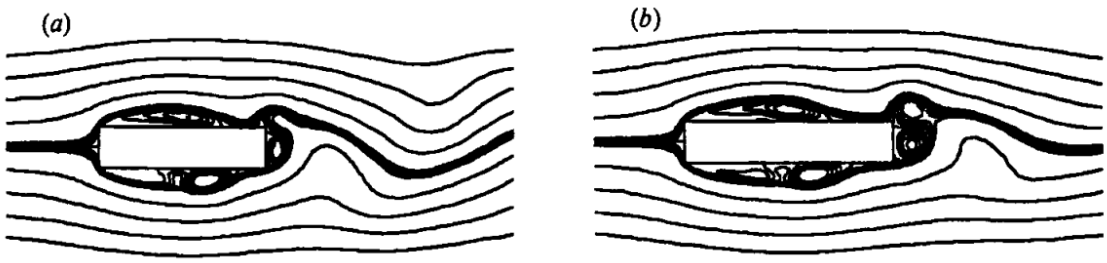

Figure 2.15: Vorticity contour delineating the LE and TE vorticies shedding (Adapted from [91])

wake frequencies and flow topology from their actual values and structures.

A novel characteristic of the flow, not identified in prior research, is the trailing edge vortex shedding, or TE vortex. As depicted in figure 2.15, when a leading edge vortex (LE vortex) nears the trailing edge, the reattached boundary layer detaches anew, curling up to shed a T-vortex in the wake. This T-vortex interacts with the oncoming LE vortex on the same lateral face of the cylinder, with both being subsequently shed as one vortex downstream. This interplay between LE and TE vortices is observed alternately on the cylinder's opposing sides at the top and bottom corners of the trailing edge. It culminates in the creation of a regular pattern, akin to a vortex street. Namely, ILEV/TEVS.

2.3 Flow around rectangular and square cylinders at an angle of incidence

The angle of incidence in the flow has a substantial influence in modifying the flow topology and shifting the characteristics of how the shear layer separates, impinges, and rolls into the wake. In this section, we will explore in detail the flow topology and characteristics around rectangular and square cylinders when placed at an angle of incidence. This will help to further comprehend how the asymmetry, introduced

by the incidence angle, influences the flow behavior in the vicinity of the rod.

2.3.1 Flow regimes classification and the critical angle of attack

Igarashi (1984) [49] pioneered the investigation of the incidence angle's influence on the flow dynamics surrounding a square cylinder. He discerned four unique flow patterns, each determined by a specific range of the angle of incidence (α). These patterns are delineated as follows:

1. ($0° < \alpha < 5°$): Shear layer separation from the leading edge with no interaction or impingement yielding a symmetric flow.

2. ($5° < \alpha < \alpha_{cr}$) In this regime, the flow becomes asymmetric due to the angle of incidence. The vortex shedding process is similar to the regular Karman vortex street, with the vortices shedding alternately from the upper and lower edges of the cylinder.

3. ($\alpha_{cr} < \alpha < 35°$): Shear layer reattach to the square lateral faces.

4. ($35° < \alpha < 45°$): Symmetric wedge flow.

Figure 2.16 delineates the fluctuating pressure coefficient (Cp') plotted at the middle of the leeward lateral face (C) and the leeward face (B) against the angle of incidence. A closer look at this diagram reveals two distinct behaviors divided by a critical angle of incidence, which corresponds to the lowest observed Cp' value. Post this critical point, Cp' exhibits an increasing trend until it eventually reaches a plateau as it nears the symmetric wedge angle.

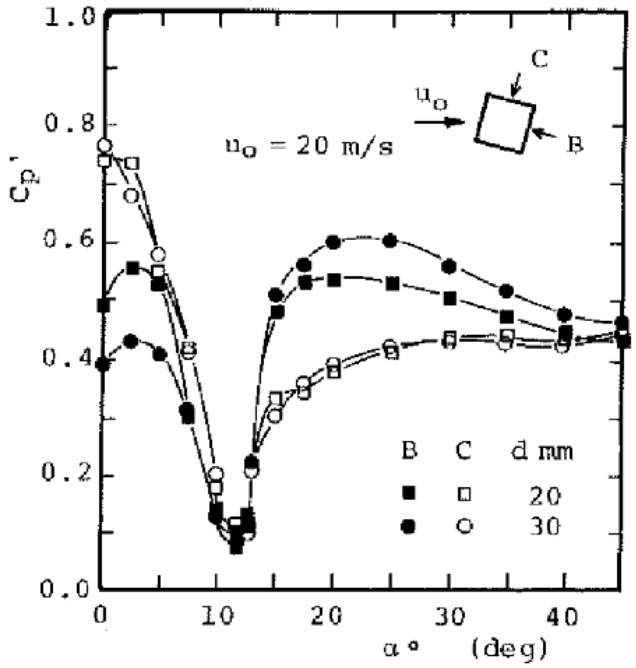

Figure 2.16: Fluctuating pressure coefficient Cp' at different points on the faces of the square cylinder at different angle of incidence. $Re_l = 27,000$ squares; $Re_l = 41,000$ circles (Adapted from [49])

Expanding on Igarashi's (1984) [49] classifications of wake flow patterns at varying incidence angles, Huang (2010) [46] made further comprehensive contributions. The expanded categorization by Huang is as follows:

1. $(0° < \alpha < \alpha_{cr})$: Named as subcritical flow which is characterised by a classical stagnation as a result of the flow impingement on the windward faces forming two separation points and typical vortex shedding street is present in the wake.

2. $(\alpha_{cr} < \alpha < 45°)$: Named as supercritical flow which is characterised by the formation of the separation bubble at the surface of the windward lateral face and a significant flow reattachment is present at the critical angle of incidence.

3. $(\alpha = 45°)$: Named as wedge flow which is characterised by the flow separation at the adjacent edges on the cross-stream axis resulting in a symmetric flow

downstream.

In the parlance of flow topology, a "critical point" denotes a location within the fluid flow where the trajectory of the streamlines is indeterminate; examples of such locations include points known as saddles. On the other hand, a "separatrix" is characterized as a specific streamline that originates from or concludes at a saddle point. These terminologies contribute significantly to understanding complex flow behaviors by illustrating how streamlines diverge or converge at specific points within the flow.

Figure 2.18(a) displays the line of stagnation, also known as the 3-way saddle point line. This line delineates the impingement point of the free shear layer. As indicated in the figure, the oil line, which signifies the stagnation point, progressively relocates between points A and B with the increase in angle of incidence. Remarkably, this shift in the location of the stagnation point does not seem to be influenced by changes in the Reynolds number. This suggests that the impact of incidence angle on the flow characteristics around the cylinder might be more profound than the effects induced by Reynolds number changes at these conditions.

Figure 2.4(b) displays critical points on cylinder side B. In the subcritical region, a dual-ring bubble appears behind the leading edge, its second oil strip's location diminishing as the angle increases. This junction is a three-way saddle. In the supercritical region, a single oil strip at the reattachment point becomes evident, shrinking and disappearing as the angle nears 45 degrees. It's notable that the complex recirculation zone in the subcritical region varies with Reynolds number, while the reattachment point's position in the supercritical region is Reynolds number independent.

For studies on the effect of different flow and geometrical parameters on altering the critical angle of incidence. In his insightful study, Tamura (1999) [126] explored the relationship between the incoming flow turbulence intensity, the geometry of the

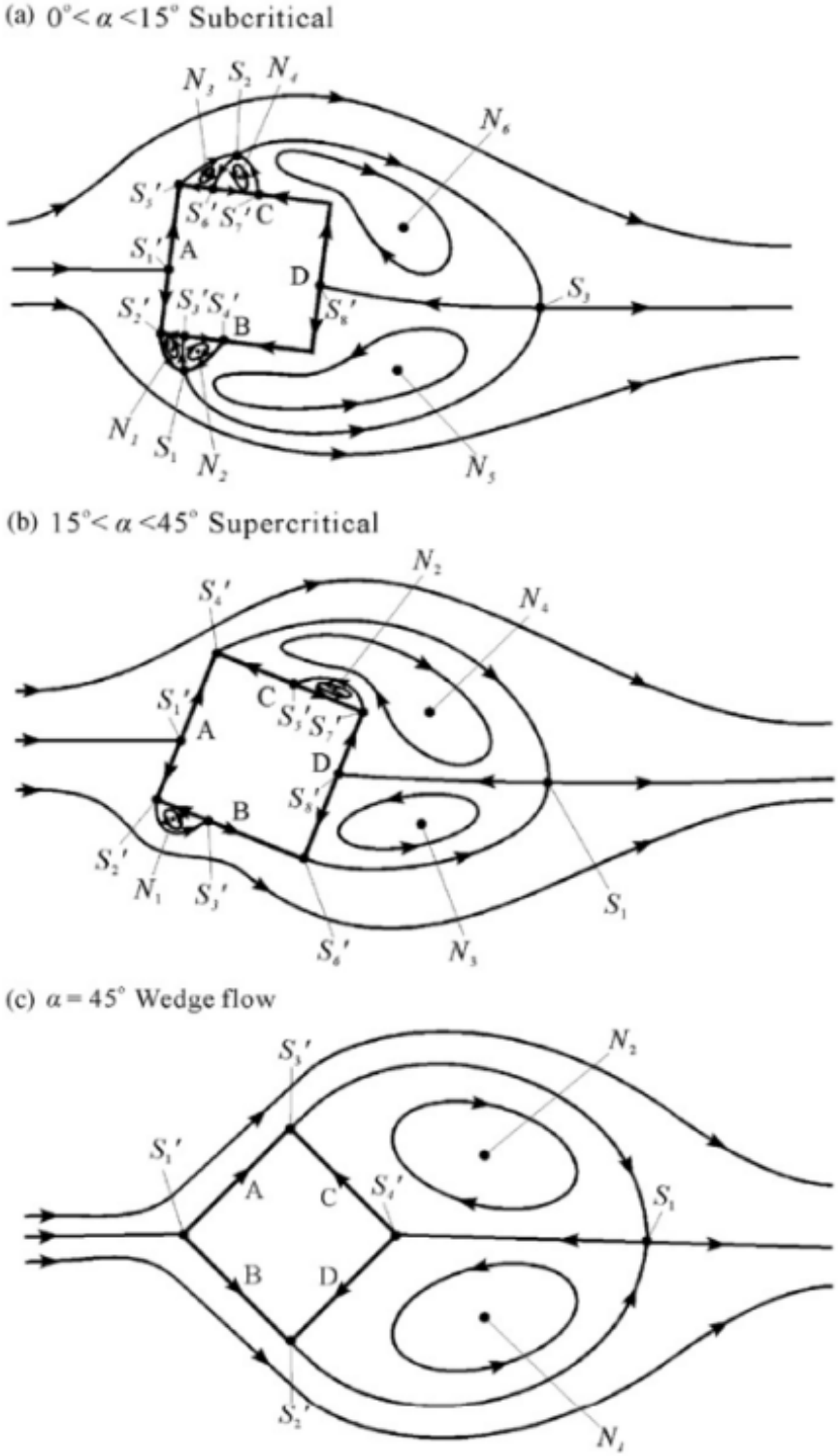

Figure 2.17: Streamlines which outlines the different flow patterns at $Re_l = 5000$ (Adapted from [46])

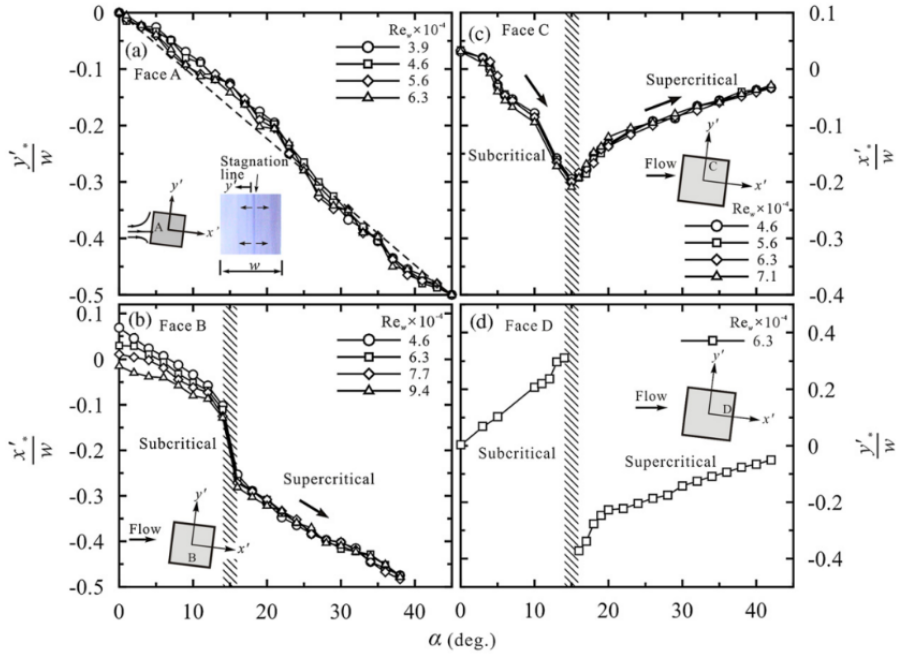

Figure 2.18: Surface-oil measurements showing the position of the topological critical point at different Reynolds number (Adapted from [46])

cylinder edges, and their collective influence on the critical angle of incidence. The findings from his research highlight an inverse relationship between the turbulence intensity and the angle of incidence, suggesting that a rise in turbulence intensity corresponds with a decrease in the angle of incidence. Additionally, he discerned that modifications to the cylinder edges, specifically rounding or chamfering, have substantial implications for the critical angle of incidence. His observations suggest that such alterations can result in a substantial reduction of the critical angle, revealing an important interplay between edge geometry and fluid dynamics. Chen (1999) [19] delved into the effects of varying the Reynolds number, specifically within a lower range of 2000 to 3300, on the critical angle of incidence. A noteworthy observation from his research was the discovery of an inverse correlation between the Reynolds number and the critical angle of incidence. This finding suggests that as the Reynolds number decreases within the aforementioned range, the critical angle of incidence cor-

respondingly increases, thereby revealing an intriguing dimension to the dynamics of flow around a square cylinder.

2.3.2 Effect of angle of incidence on the hydrodynamic loading

Figure 2.19 depicts the average lift and drag coefficients, computed indirectly via the integration of pressure measurements at various points along the cylinder's span. Superimposed on the plot are results from Otsuki et al. (1978) [89], derived from direct measurements of the hydrodynamic load on the cylinder. A notable feature in this data is the inflection point of the curve at a critical angle of incidence $\alpha_{cr} = 15°$. Here, the drag coefficient is at a minimum and the slope's sign flips. Discrepancies between the coefficient values from the two sources become more prominent at high angles of incidence. These disparities can be attributed to differences in the blockage ratios between the two studies, which stem from their respective wind tunnel dimensions. As the angle of incidence changes significantly, it correspondingly alters the blockage ratio.

In an extensive study conducted by Tamura (1999) [126], the impact of approaching flow turbulence intensity and edge geometry on the average lift and drag forces were thoroughly examined, as represented in figure 2.20. Tamura discovered an inverse relationship between turbulence intensity and the drag coefficient C_d, which is particularly evident at angles of incidence below the critical angle α_{cr}. Conversely, the lift coefficient C_l exhibited a direct correlation with the turbulence intensity, increasing as turbulence decreased. Moreover, the least value of the lift coefficient was observed to shift towards lower values of incidence with less turbulence. These findings suggest that both the turbulence intensity of the incoming flow and the edge

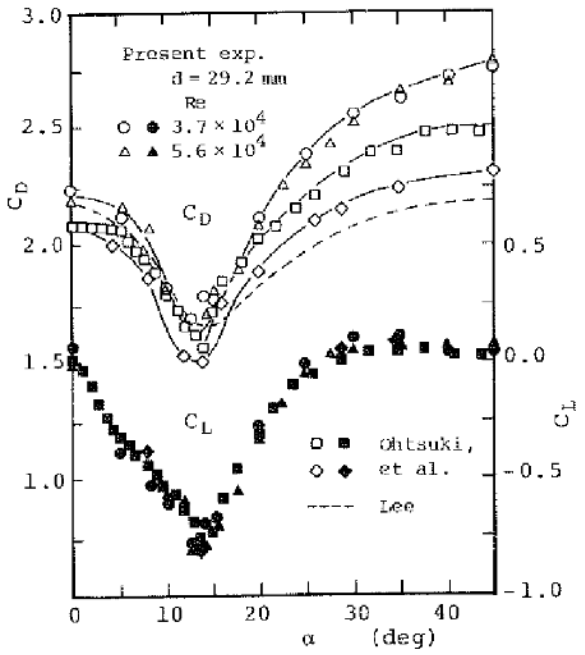

Figure 2.19: Lift and Drag coefficients at a range of Reynolds numbers (Adapted from [49])

geometry of the cylinder significantly affect the resultant aerodynamic forces.

Figure 2.21 encapsulates Tamura's findings on the impact of edge geometry on the mean lift and drag coefficients. The study encompassed various edge geometries, including sharp, chamfered, and rounded edges. Interestingly, cylinders with sharp edges manifested markedly elevated drag coefficients compared to their chamfered and rounded counterparts. Furthermore, edge geometry significantly influenced the critical angle of incidence, with the rounded edges recording the smallest value, followed by chamfered edges and sharp edges respectively. The intriguing aspect of these results, highlighted in figure 2.21(b), lies in the lift force coefficient's fluctuation. It appears that rounding the edges has a profound influence on suppressing the fluctuating hydrodynamic loading on the cylinder.

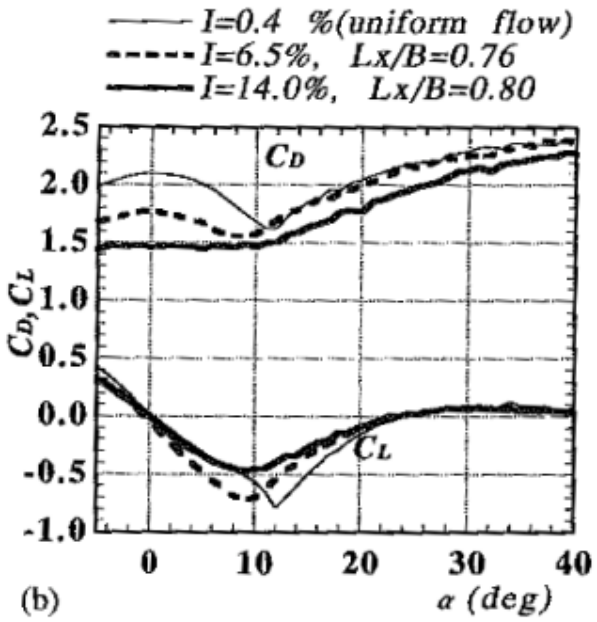

Figure 2.20: The effect of the approaching flow turbulence level on the drag and lift coefficients at different angles of incidence (Adapted from [126])

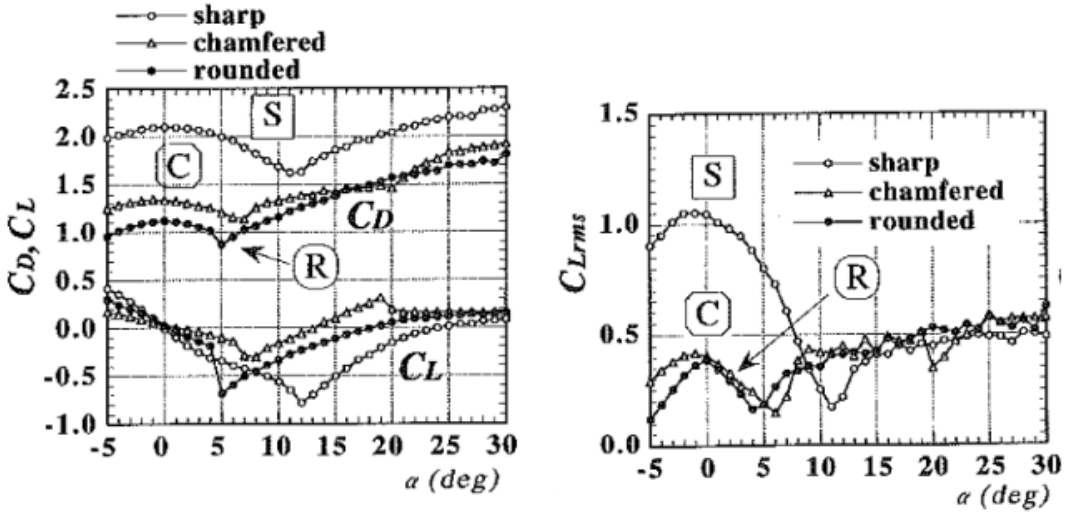

(a) Mean Cl and Cd

(b) Fluctuating Cl

Figure 2.21: Cylinder edge geometry effect on the mean lift and drag coefficients at different angles of incidence (Adapted from [126])

2.4 The effect of externally applied periodic disturbance on the flow topology

The catastrophe that befell the Tacoma Narrows Bridge first highlighted the significant impact of vortex-induced vibrations. A surge in wind speed prompted an increase in the vortex shedding frequency, which, unfortunately, corresponded with the bridge's inherent mechanical resonant frequency. This unfortunate alignment induced amplified oscillations, culminating in the bridge's eventual downfall. This phenomenon exemplifies a fluid-elastic oscillation mode, a concept that was first delineated by Rockwell & Naudascher in 1979 [100]. Not only do such instances present an intrinsic hurdle for researchers, but they also establish a substantial impetus for investigations that enhance our comprehension of the dynamics between flow and structures. Understanding the impact of periodic flow perturbations on the flow behavior around bluff bodies is of particular interest. Here are some representative examples of potential flow perturbation:

1. Velocity perturbation applied to the mean free stream.
2. Forced cross-stream oscillation of the bluff body.
3. Centrifugal oscillations for circular-like bluff bodies.
4. Acoustic resonance standing wave oscillation in longitudinal or transverse direction.
5. Flow-induced oscillations.

2.4.1 Applied velocity perturbation

Blevins (1985) [13] endeavored to comprehend the acoustic feedback loop between the vortex shedding process and the sound field surrounding circular cylinders. A key revelation of his research was the synchronization of the vortex shedding frequency with the applied velocity perturbation frequency. As the perturbation frequency escalated, the shedding frequency maintained a consistent pace with it. Alongside, he noticed a remarkable augmentation in the spanwise correlation of the generated vortices. Additionally, Blevins observed a direct proportionality between the amplitude of the introduced sound and the lock-in range, further elucidating the connection between acoustic stimuli and fluid dynamics.

In a study on rectangular cylinders, Knisely et al. (1986) [58] subjected the flow around the cylinder to streamwise velocity perturbations. Their research uncovered a marked decrease in base pressure when even minor velocity perturbations were applied. Flow field visualizations pinpointed this drop in base pressure to a reduced vortex formation length, resulting from an increase in curvature of the shear layer.

Wu et al. (1993) [142] took a novel approach to studying velocity perturbations by inducing such perturbations in a water tunnel. Their method involved adjusting the tunnel walls at a specifically tuned frequency and amplitude. They focused on a rectangular cylinder with an aerodynamic leading edge, aiming to understand the effect of velocity perturbations on vortex shedding. Their findings pointed to a crucial threshold in the freestream's perturbation percentage, which needed to be surpassed for lock-in between the perturbation and vortex shedding to occur. If the applied perturbation fell below this threshold, the coherence of the vortices was markedly reduced, demonstrating the critical role that the intensity of perturbations plays in modulating vortex behavior.

In an innovative experiment designed to mimic the conditions of transverse acous-

tic duct mode excitation, Parker & Welsh (1983) [94] utilized diaphragm speakers on both sides of a wind tunnel. These speakers facilitated precise control over the frequency and amplitude of the applied perturbations. They discovered that leading-edge vortices of rectangular cylinders with aspect ratios between 7.6 and 16 became synchronized with the applied frequency. Concurrently, the separated bubble mirrored the exact oscillation frequency. A key insight from their study was the importance of shear layer reattachment: the shear layer only responded to the applied perturbation if reattachment occurred. For shorter rectangular cylinders with an aspect ratio less than 3, they observed that the applied sound failed to influence vortex shedding, underscoring the influence of geometry and aspect ratio on flow dynamics.

2.4.2 Forced oscillations

There has been substantial research aimed at mitigating flow-induced vibrations as a means to prevent oscillation or limit its effects, thereby circumventing structural fatigue failures. The majority of these investigations have concentrated on bluff bodies with a circular-like geometry. However, a relatively smaller number of studies have explored the oscillations associated with elongated rectangular cylinders, highlighting a potential area for further exploration and research.

In investigations focused on circular cylinders, Stansby (1976) [120] delved into changes in base pressure during forced oscillations of the cylinder in the cross-stream direction. Remarkably, when the cylinder oscillation frequency neared the natural frequency of vortex shedding, both frequencies were found to synchronize or lock-in, leading to in-phase oscillations. As depicted in Figure 2.22, a significant phase shift between the cylinder oscillation and vortex shedding emerges as the oscillation frequency approximates the vortex shedding frequency. Notably, these shifts accompany substantial alterations to the base pressure coefficient.

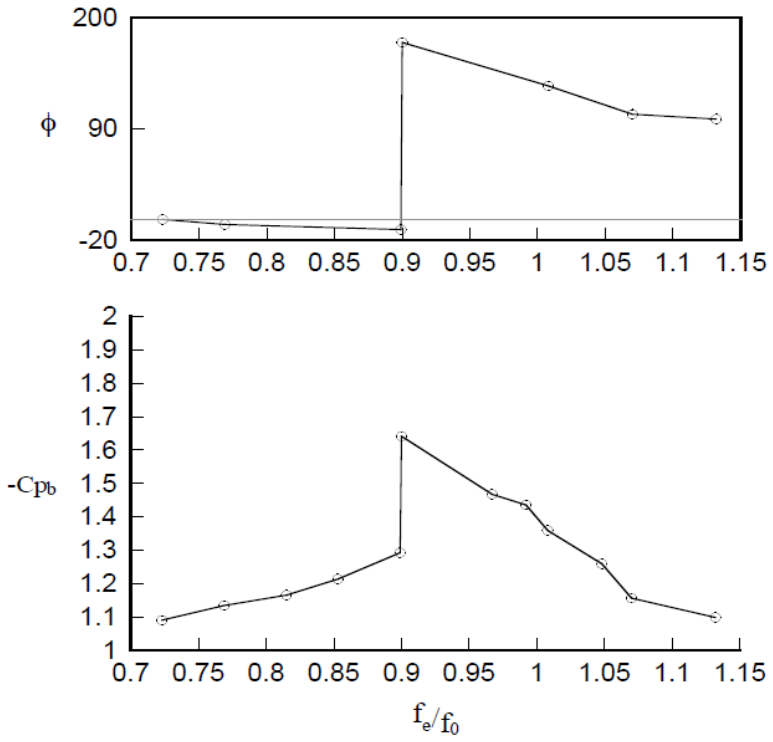

Figure 2.22: (a) Shedding phase wrt to the cylinder oscillation frequency, (b) Base pressure coefficient $C_{p(b)}$ vs. the oscillation frequency of the cylinder. (a) and (b) are at the same amplitude ratio. (Adapted from [120])

Handful of investigations studied the flow around rectangular cylinder with forced oscillations at different aspect ratios (Bearman & Obasaju (1982) [9]; Nakamura & Nakashima (1986) [77]; Deniz & Staubli (1997) [25]).

Nakamura & Hirata (1989) [76] investigated aspect ratio ranging from 0.2 to 1 for forced oscillation rectangular cylinder. As observed before, the shedding frequency seemed to lock with the cylinder oscillation frequency when the applied frequency is close to the shedding frequency of non-oscillating cylinder. They observed a critical aspect ratio around 0.6. Below this value, the applied oscillation reduced the base pressure which is the result of the reduced length in the vortex formation length. On the other hand, the cylinders with aspect ratios above 0.6 the oscillations seemed to enhance the shedding process by increasing the shear layer curvature, hence the

length of vortex formation.

Deniz & Staubli (1997) [25] further expanded the research to include rectangular cylinders of higher aspect ratios (AR=2) and high Reynolds numbers, examining the vortex shedding response to forced oscillations. Their study revealed a synchronization and in-phase relationship between the cylinder oscillation and the downstream vortex shedding. To probe the reaction of leading-edge vortices, they manipulated the oscillation to resonate with the combined vortices at the leading and trailing edges of the cylinder. Remarkably, their experiments revealed a phase shift between the dynamic transverse loading (evident through lift force) and the cylinder's oscillatory motion.

Ongoren & Rockwell (1988) [87] observed one common feature observed for the forced oscillation of different bluff bodies is the lock-in between the vortex shedding frequency and the frequency of the applied oscillation when this frequency is close to the natural shedding frequency of non-oscillating bluff body. Throughout this spectrum of frequencies, substantial alterations in the phase correlation between vortex shedding and the bluff body oscillations are observable. However, it's important to note that the emergence and characteristics of this phase shift are intimately linked to the specifics of the downstream-facing geometry (for example trailing edge in case of rectangular cylinder). This implies that even slight modifications to the geometry can significantly influence the interactions between vortex shedding and body motion. For bluff bodies with short streamwise length, significant alterations in the base pressure coefficient align with this phase change, provided there is no disruption in vortex formation from the leading edge by the body's downstream-facing geometry. However, for a bluff body with a substantial streamwise length, there is, in fact, no discernible phase shift in the vortex shedding from the leading edge, even when the body oscillation frequency varies. This finding illustrates how the structure's

geometry can significantly influence the flow dynamics around it.

2.5 Flow-sound interaction mechanism in rectangular cylinders

2.5.1 Sound generation by periodic flow structures

Curle (1955) [23] posited that during the flow past standard bluff bodies, acoustical energy or sound is produced in both cross and streamwise directions named aeolian tone. This tone is attributed to a dipole source and originates from fluctuating hydrodynamic forces acting on the bluff body, specifically the drag and lift forces. The cross-stream component of the dipole is dominant, as the lift force is typically around 90% greater than the drag force. A representation of the sound radiation from a dipole source can be seen in Figure 2.23.

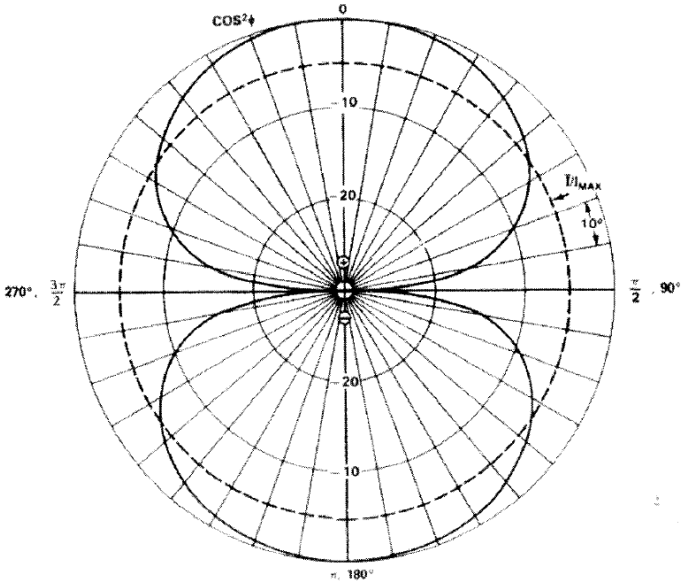

Figure 2.23: Dipole source sound radiation in the far field. (Adapted from [11])

Uffinger et al. (2008) [132] conducted an exploration into the sound radiation from rectangular cylinders with varying leading and trailing edge designs. The findings, illustrated in figure 2.24, suggest that the rounding of the leading edge appears to mitigate sound radiation. Conversely, a rounded trailing edge seems to intensify the emitted sound. A similar finding is reported in our results during acoustic resonance excitation which will be discussed in detail in a later chapter.

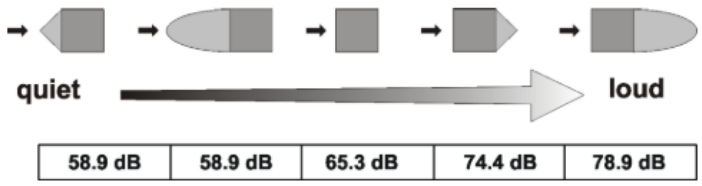

Figure 2.24: Different leading and trailing edge geometries with the SPL scale. (Adapted from [132])

Fujita (1998) [33] examined the variations in the Sound Pressure Level (SPL) produced by a square cylinder at differing angles of incidence. Prior to reaching the critical angle, the SPL demonstrated a downward trend, bottoming out at the critical angle of incidence. However, after surpassing the critical angle, the SPL witnessed a swift rise, reaching an approximate value of 50 dB, and then remained relatively constant thereafter.

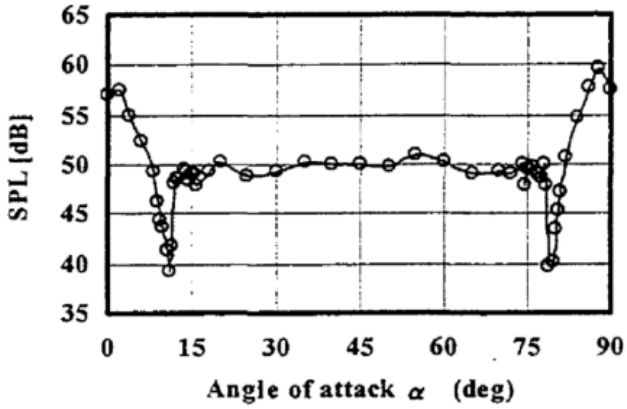

Figure 2.25: SPL at different angles of incidence for a square cylinder (Adapted from [33])

2.5.2 Self-excited acoustic resonance

A bluff body within an enclosure has the potential to self-excite the enclosure's acoustic modes. This process is contingent on the bluff body's position and the shedding patterns around it ([5], [4], [6], [69]). For instance, in a rectangular or square duct with the bluff body positioned centrally (refer to Figure 2.26), the odd-numbered acoustic modes are most likely to be excited. However, adequate energy from the flow field is required to excite an acoustic standing wave. This typically happens when the shedding pattern frequency synchronizes with the duct acoustic mode frequency under appropriate phasing [23]. As the flow velocity increases, the shedding frequency locks onto the acoustic mode until a "lock-out" point is reached, where the shedding reverts back to the Strouhal periodicity. Further lock-in events may occur at higher velocities.

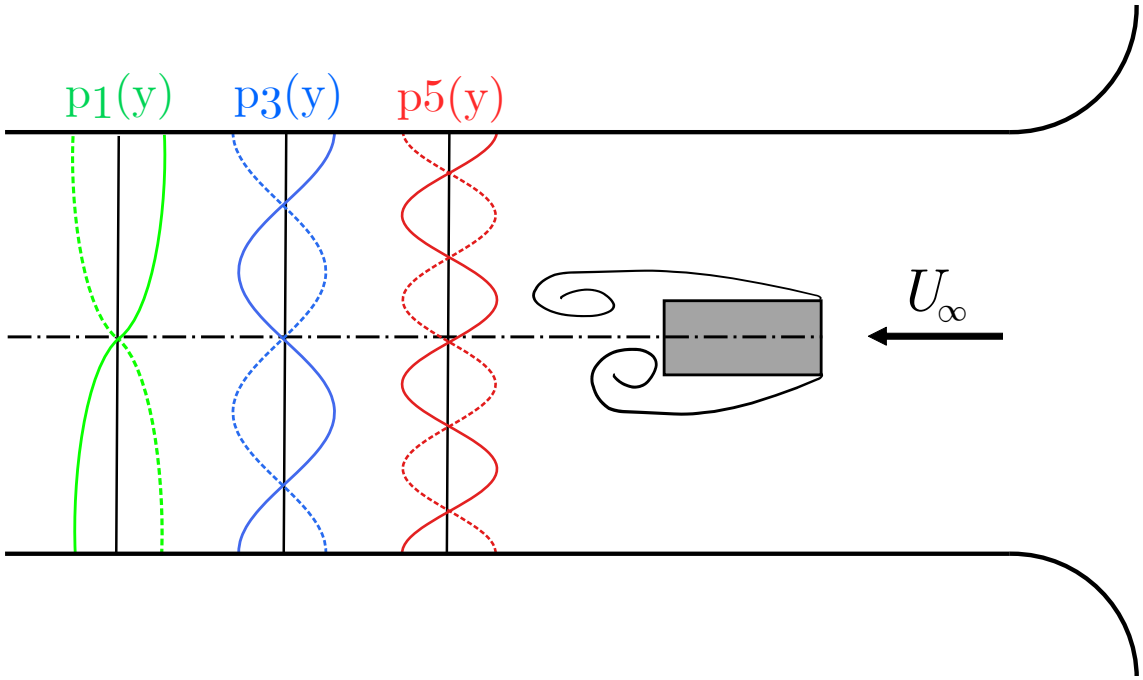

Figure 2.26: Rectangular cylinder positioned at the anti-node of odd-numbered transverse acoustic modes within a duct along with the pressure distribution associated with the first pair of these modes (This figure is not to scale).

2.5.3 Rectangular cylinders under acoustic resonant conditions

Parker (1966) [92] investigated the mechanism of self-excited acoustic resonance for rectangular cylinders placed in a staggered cascade arrangement (see figure 2.27) at different flow velocities. He found that the excitation is a result of a frequency coincidence between the duct transverse mode and the natural shedding frequency with a wavelength multiple of the gap between the cylinders.

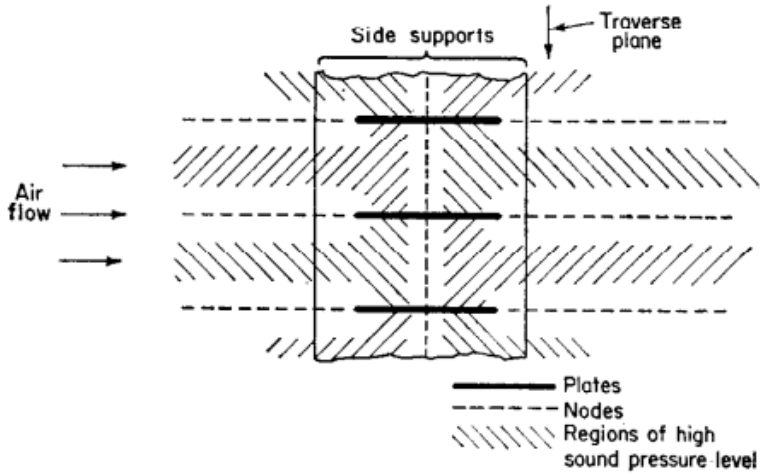

Figure 2.27: Schematic of the arrangement of the plates in cross flow (Adapted from [92])

Welsh & Gibson (1979) [140] offers significant insights into the interaction between fluid flow and acoustics for rectangular cylinders with an aspect ratio of 5, placed within a high-speed wind tunnel. They observed two distinct mechanisms of excitation. The first excitation occurred at the frequency where the progressing shedding coincided with the acoustic transverse mode. Meanwhile, a second phenomenon, referred to as 'excited vortex shedding', occurred at an undetectable frequency but resulted in a sudden and noticeable excitation (refer to Figure 2.28). However, the specifics of this excited vortex shedding pattern, as well as the reasons behind its occurrence, remained unexplained due to the limitations in the flow visualization techniques available at the time. Later, Nakamura et al. [79] suggested that this early excitation is a result of the excitation of the intrinsic shear layer instability. This is further evident from Shabaan & Mohany (2022) [114] as we can see the early and natural coincidence excitation for a rectangular cylinder of aspect ratio of 2 (see figure 2.29).

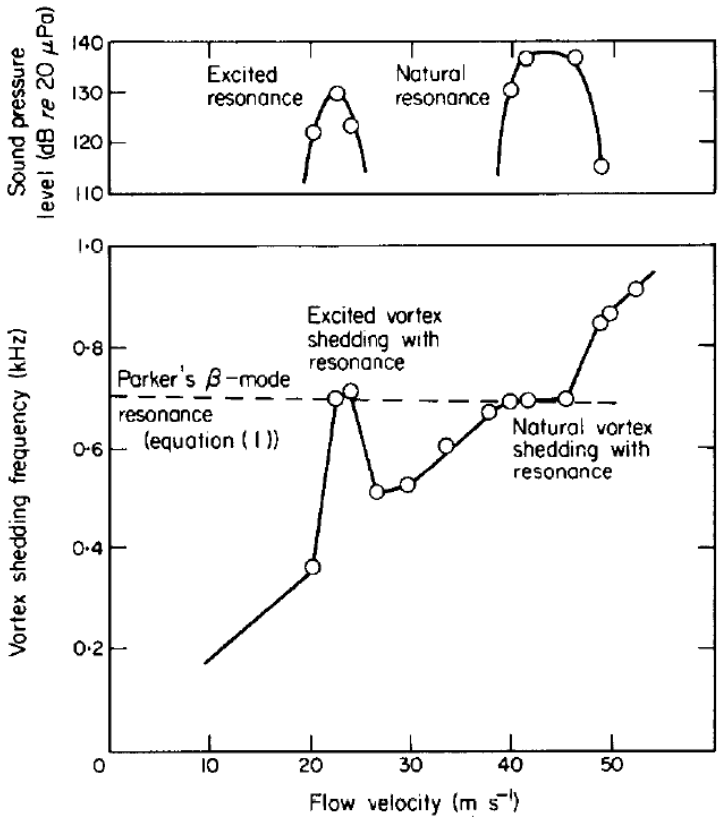

Figure 2.28: Vortex shedding frequency at different flow velocity with the natural and excited modes coincidence with acoustic transverse modes ($Parker's \beta - mode$). (Adapted from [140])

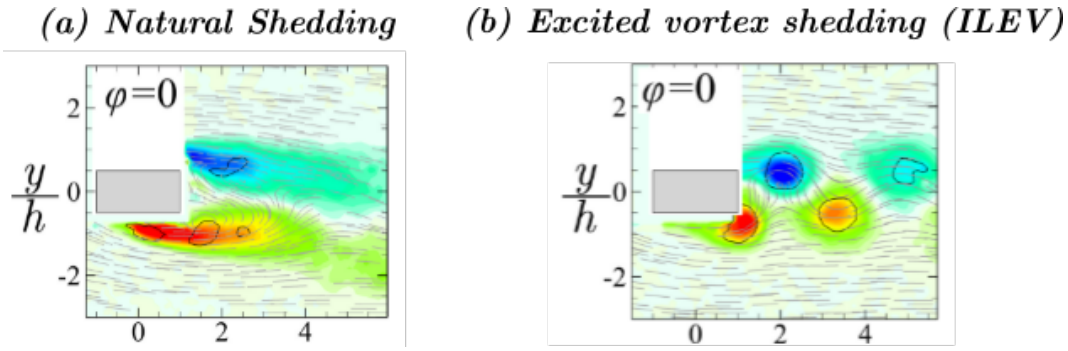

Figure 2.29: Vorticity field at the peak of acoustic resonance excitation of the same transverse acoustic mode ($Parker's \beta - mode$) at two different flow velocities showing the two shedding patterns for a rectangular cylidner with $AR = 2$ (Adapted from [114])

In their compelling research, Welsh et al. (1984) [94] highlighted two primary

findings relating to the excitation of resonance in sharp and rounded (semi-circular) leading edges. They discovered that a sharp edge could stimulate resonance over two frequency ranges due to the interaction between separation from the leading edge and the feedback acoustic pressure signal from the trailing edge. Conversely, rounded leading edges were found to generate resonances over only a single range, as shedding occurred solely from the trailing edge. These findings are expanded upon in Section 3, which offers an extensive analysis of how varying edge rounding impacts flow-acoustic coupling.

Stoneman et al. (1988) [122] studied two rectangular cylinder in tandem arrangement at different spacing ratios. They found that having a cylinder downstream can lead to the suppression of the resonance excitation found for a single cylinder. However, excitation at new flow velocities was found to take place. Interestingly, they found that the ratio between the the cross-stream length of the upstream cylinder and the spacing between the cylinders directly affects the SPL at peak of acoustic resonance with local minimums and maximums as this ratio increase which is clear in figure 2.30

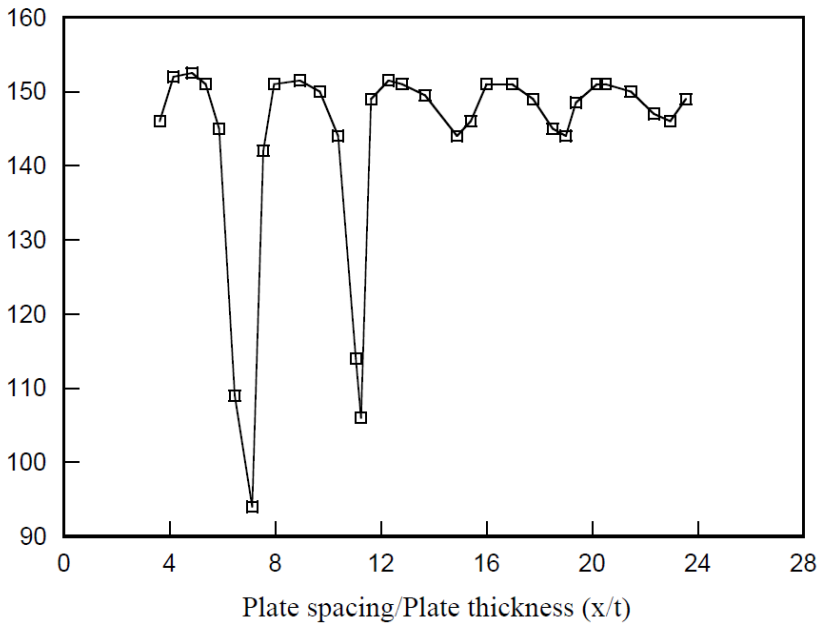

Figure 2.30: SPL at peak of acoustic resonance excitation at different cross-stream length to spacing ratio (Adapted from [122])

2.6 Summary and thesis scope

This in-depth literature review illuminates the progress made over the past decades in understanding the mechanisms of flow-structure and flow-sound interactions for rectangular cylinders with varying configurations. Despite these advances, a comprehensive study focused on the flow-sound interaction mechanism of moderately long rectangular cylinders has not been given due attention.

This thesis, therefore, concentrates on rectangular cylinders with relatively small aspect ratios, specifically choosing an aspect ratio of 2 for an extensive investigation into the mechanisms of flow-sound interactions and flow behavior under non-resonant conditions. This investigation includes variations in flow incidence angle and edge geometry. To unravel these interactions, a series of detailed experiments has been conducted involving acoustic measurements, flow visualization utilizing a Particle

Image Velocimetry (PIV), and direct measurement of the hydrodynamic loading on the cylinder with the aid of piezoelectric force transducers. The subsequent sections will delineate the findings from our in-depth study, culminating in a conclusion that summarizes the key insights gained from this research. The scope of this thesis thereby contributes significantly to the understanding of fluid-structure-sound interactions, specifically for rectangular cylinders with smaller aspect ratios at varying geometrical configurations.

Chapter 3

Characteristics of the flow-induced noise from rectangular rods with different aspect ratios and edge geometry

Cited as: A. Shoukry and A. Mohany, Characteristics of the flow-induced noise from rect- angular rods with different aspect ratios and edge geometry. Journal of Fluids and Structures (2023) 103959,https://doi.org/10.1016/j.jfluidstructs.2023.103959

3.1 Introduction

Flow-acoustic coupling is found to be disastrous in different engineering applications due to the generation of severe noise and intolerable vibration levels, which could lead to fatigue failure of structures or irreversible damage. Some examples of such applications that encounter flow-acoustic coupling are tube arrays in heat exchangers

([139], [124], [30]), cavity flows ([1], [80]), side branches in piping systems [146], and control valves [145]. Self-Excited acoustic resonance is triggered by the flow instabilities when their frequencies coincide with an acoustic mode in the system and the flow energy is enough to overcome the acoustic damping. During this process, energy exchange takes place between the acoustic and the flow fields organizing the flow instability which in turn generates severe noise. The flow-sound interaction mechanism for cylindrical structures in cross-flow has received considerable attention in the literature. However, flow acoustic coupling from rectangular rods in cross-flow didn't receive much attention, even though they are widely used in different industrial applications. The flow separation and reattachment around rectangular rods in cross-flow is fundamentally different than that around circular cylinders. Additionally, the shape of the corners in rectangular rods (i.e. sharp, chamfered, or round corners) is bound to have an effect on the flow separation mechanism and its coupling with an acoustic mode. Therefore, the main objective of this chapter is to investigate the flow-excited acoustic resonance from rectangular rods with different aspect ratios and edge geometry and its effect on the dynamic lift forces and wake structure.

For studies done outside of acoustic resonance excitation, Ohya (1994) [83] found that the shear layer behaviour is dependent on the rod aspect ratio. Hence, significant changes in the rod base pressure was observed when different aspect ratios were tested. Van Oudheudsen et al. (2005) [134] reported that the wake topology, Strouhal periodicity and aerodynamic forces are significantly dependent on the rod aspect ratio and the flow incident angle. Nakamura et al. (1996) [78] studied the wake characteristics of rectangular rods with different aspect ratios at low Reynolds numbers. They found that for the investigated aspect ratios, at Reynolds number around 250, the vortex shedding street switches from two shear layers separating from the leading edges, namely Karman vortex street into a single separated shear layer street, namely

impinging shear layer instability. Dobre (2004) [26] experimentally studied the wake of square rods at high Reynolds number and reported that the wake flow structures exhibit similarities with that observed downstream of circular cylinders and indent flat plates. Gonc alves da Silva Pinto and Margnat (2020) [36] investigated the noise generated for different geometries and reported that globally for all tested geometries, increasing the aspect ratio (the length in the flow direction against the height perpendicular to the flow direction) will always decrease the generated noise.

For studies performed on the effect of rounding the edges of rectangular rods, Tamura & Miyagi (1999) [126] found that edge rounding have a favourable effect in terms of reducing the fluctuating lift and drag forces due to substantial changes in the flow topology and wake dynamics. Carassale et al. (2014) [16] experimentally studied the effect of corners rounding in square rods. A substantial reduction in the aerodynamic forces was observed. Also, the rounding yielded a lower critical angle of incidence which is defined as the angle at which the flow reattaches on the lateral faces. Several studies later confirmed these findings ([133], [31], [24]). Esfeh et al. (2021) [31] found that increasing the edge rounding of a square rod results in a higher Strouhal number and lower drag and lift fluctuations. This was attributed to the disruption of the organized vortex shedding due to delayed separation. However, all of these investigations were performed on rectangular rods with sharp or rounded corners in the absence of acoustic resonance excitation.

The flow structures in the wake of rectangular rods suggest that this bluff body is susceptible to fluid-resonant mechanisms. Shaaban & Mohany (2022) [114] studied the flow characteristics and the aeroacoustic response of rectangular rods with different aspect ratios. They found that there is a minimum rod length in the flow direction that causes an early excitation of higher acoustic modes. So, the aspect ratio of $l/h = 2$ was chosen in this study to be comprehensively investigated and

compared with aspect ratios of $l/h = 0.5$ and 1 since the former case was reported to early self-excite higher duct acoustic modes at frequencies far from the typical vortex shedding frequency. Early here means that the excitation took place at a frequency that does not coincide with the dominant shedding mode frequency but rather it coincides with another undetectable instability frequency. Shaaban & Mohany (2022) [114] suggested that the early excitation of the third acoustic duct mode is due to the existence of a shear layer instability periodicity which requires a minimum rod length in the direction of the flow to materialize. This instability was not detectable in the acoustic pressure spectrum outside of resonance because the vortex shedding was dominant and masked out the shear layer instability.

The work presented in this chapter is an extension of the work presented at the FIV 2022 conference [116] to investigate the role of the shear layer instability from rectangular rods on the early excitation of higher order acoustic modes. One of the objectives of this study is to investigate the shear layer instability by modifying the rod leading and trailing edges to understand the shear layer separation and impingement mechanism and its coupling with resonant acoustic modes. Such knowledge will clarify the source(s) that triggers the early excitation of higher acoustic modes, which, in turn will improve our understanding of the flow-sound interaction mechanism for the case of rectangular rods in cross-flow. Ultimately, this will provide a design safeguard for applications employing rectangular rods subjected to high cross-flow velocities.

3.2 Experimental Setup

The experiments were conducted in an open-loop wind tunnel at the Fluid-Structure Interaction and Noise Control Laboratory at Ontario Tech University, Oshawa, Canada. The test section is 762 mm long with a diffuser section connected to an acrylic test

section with a height of $H = 254mm$ and a width of $W = 127mm$. The maximum turbulence intensity was measured along the full range of velocities and was found to be less than 0.8%.

Six different cases of rectangular rods were investigated. Table 3.1 shows the investigated cases with their dimensions. The aspect ratio is equal to A.R= l/h. Where l is the rod length in the direction of the flow and h is the rod length perpendicular to the flow direction. The tested cases are, all-sharp edges, the two-upstream rounded edges, the two-downstream rounded edges, and all-rounded edges. All the rounds have the same dimension of $r/l = 1/8$. This rounding ratio was chosen based on the available information in the literature as this rounding ratio had an influence on the separation point and caused a reduction of the hydrodynamic forces rounded2014. Figure 3.1 shows a schematic of all the tested cases. To ensure flow uniformity in the spanwise direction, pressure measurements were performed along the span of a rod at 11 different points over a wide range of Reynolds numbers. The results showed that the maximum spanwise variation in the mean base pressure coefficient is within the experimental uncertainty of the measurements. All the tested cases were placed at a distance of 381 mm from the parabolic bell mouth entrance. At that location, hot-wire measurements revealed that the flow uniformity in the transverse direction has a maximum deviation of 1% from the free stream-stream velocity. To eliminate any vibration transmission to the test section from the blower, a flexible connection is used to connect them. The experiments were carried out in a monitored environment at a temperature of 25° and 50% humidity which is frequently monitored using an indoor climate sensor.

Table 3.1: The six investigated cases with the dimensions in inches

Case	l	h	r/l
(a) Square	0.5	0.5	NA
(b) Bluff rectangle	0.5	1	NA
(c) all-sharp edges rectangle	1	0.5	1/8
(d) upstream-rounded edges rectangle	1	0.5	1/8
(e) downstream-rounded edges rectangle	1	0.5	1/8
(f) all-rounded edges rectangle	1	0.5	1/8

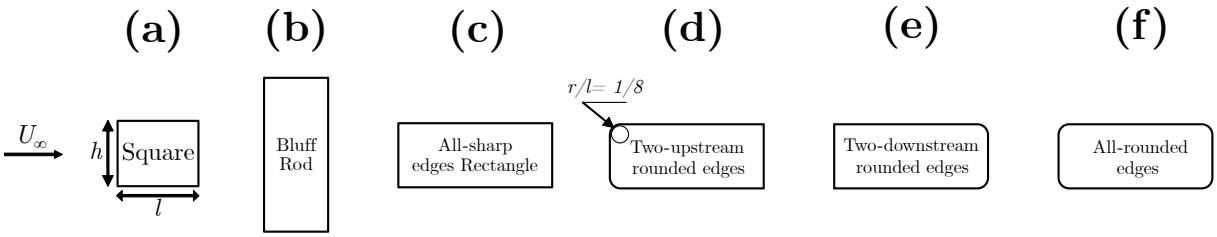

Figure 3.1: Schematic of the six investigated cases

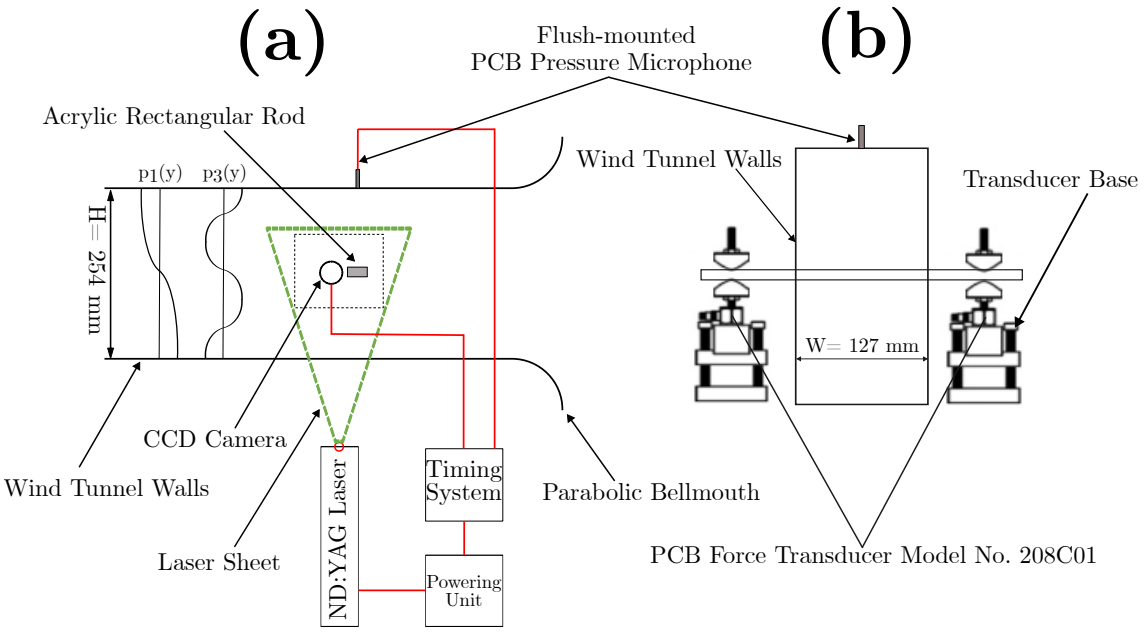

Figure 3.2: (a) Schematic of the particle image velocimetry setup. (b) Dynamic lift force measurements setup

3.2.1 Aeroacoustic measurements

Acoustic pressure was recorded for the full velocity sweep (20 m/s to 120 m/s with a 2.76 m/s step) for each case. The periodic flow structures in the wake of the rod produce pressure fluctuations normal to the rod axis. So, only transverse acoustic modes with acoustic particle velocity antinodes at the rod can be excited (e.g. $1^{st}, 3^{rd}, 5^{th}$, etc.). In the current study, the first and the third acoustic modes were excited by different shedding modes. Flush-mounted pressure microphone (6.35 mm) on the wind tunnel top wall is used to record the pressure signal generated by the unsteady separated flow in the transverse direction. The microphone is placed exactly above the centre of the rod. The pressure signal was recorded for 120 s at a sampling frequency of 20 kHz. Welch's modified periodogram method is used to analyze the pressure signal to get the frequency spectrum (FFT) with a 50% overlap and resolution of 1 Hz. A band-pass filter is applied with a range of ±50 Hz around the dominant frequency peak to extract the pressure value. The root means square value of the filtered pressure signal (P_{rms}) is obtained. The theoretical value of the first and the third acoustic cross-mode is calculated using the following equation:

$$f_{a(1)} = \frac{c}{2H} \tag{3.1}$$

$$f_{a(3)} = \frac{3c}{2H} \tag{3.2}$$

3.2.2 Dynamic lift force measurements

Two piezoelectric force sensors (PCB Model No. 208C01) were utilized for the force measurements one on each side of the cylinder mounted outside of the test section. The force sensor's nominal sensitivity is 112.4 mV/N. To prevent any vibration transmission from the test section to the sensors, the sensors were mounted on a custom-

made steel base which is isolated from the wind tunnel and rubber footing was used to mitigate ground vibration transmission to the sensors. The rods pass through a 1.5 mm gap in the wind tunnel windows. A special sealing technique was developed to prevent any air leakage and eliminate the gap effect inside the wind tunnel. From inside the wind tunnel, the gap was covered by a 0.254 mm plastic ring with lubricant between the ring and the tunnel wall to minimize any vibration translation. From outside the wind tunnel, an ultra-thin sheet is used to cover the gap from outside and was tapped into the rod and the tunnel wall. The center-to-center distance between the two sensors was tuned to achieve the maximum mechanical resonant frequency possible. Some cases resulted in high frequencies of the Strouhal periodicity which were close to the mechanical resonance frequency of the force transducer setup. These data were excluded from the measurements. A schematic of the force setup and the PIV system is shown in figure 3.2. A sample of the force sensors time signal is shown in figure 3.3 for the sharp corners case. The force-time signal for both sensors has nearly the same phase and amplitude. The same trend was observed for all the investigated cases. A double peak is clear in the total signal which was observed in previous studies performed on rectangular rods([143], [15]). This comes from the fact that the body is sufficiently long to allow vortex interaction between the leading and the trailing edges. The first peak is due to the shear layer separation from the leading edge generating a recirculating region near the rod walls that causes a negative pressure and increases the hydrodynamic loading on the rod. The second peak is present due to the shear layer minor interaction with the trailing edge. The root mean square of the lift force was calculated as follows:

$$C_l' = \frac{F_{L(RMS)}}{0.5\rho U^2 A} \tag{3.3}$$

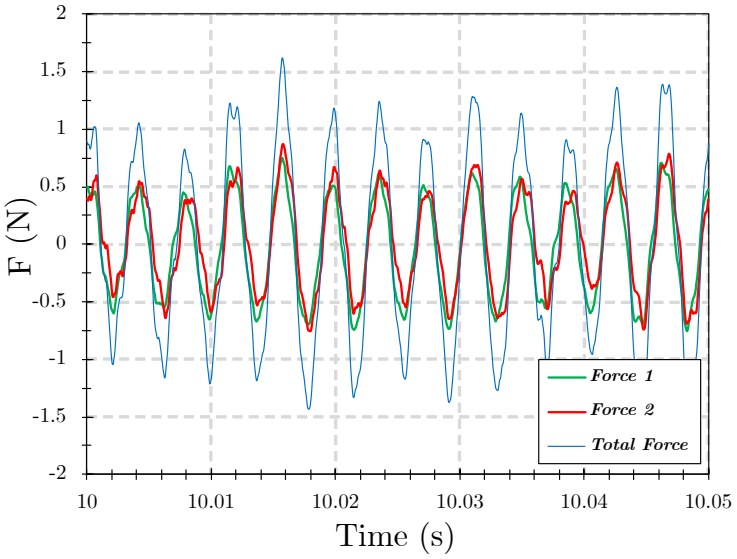

Figure 3.3: Raw signal measured from the force sensors for aspect ratio $l/h = 2$ all-sharp edges case at U = 31m/s.

Where $F_{L(RMS)}$ is the root mean square value of the dynamic lift force, C_l' is the root mean square value of the dynamic lift coefficient, ρ is the air density, U is the flow velocity, and A is the projected area of the rod in the lift force direction.

3.2.3 Particle-image velocimetry (PIV) measurements

PIV measurements were conducted using LaVision PIV system. PIV measurements were performed for 4 selected cases at selective flow velocities outside and during self-excited acoustic resonance. The laser sheet is located at the x-y mid-plane. Double-head 532 nm ND:YAG laser is used on a double pulse mode at 15 Hz with a peak power output of 200 mJ. To seed the camera field of view atomized Di-Ethyl-Hexyl-Sebacat is used. The maximum particle size is 2 μm. To minimize the optical shadow and facilitate comprehensive visualization of the entire flow field, rectangular rods that are precisely machined from optical-grade acrylic are used. This material ensures light transmission and minimal distortion, thereby enhancing the clarity and accuracy of the captured flow field. 12- bit camera is used on a double frame mode to acquire

the images with a maximum resolution of 2752x2000 pixels. For measurements at off-resonance conditions, the signal from the flush-mounted microphone was used as the input signal for the laser trigger. Since the maximum trigger frequency is far lower than the duct acoustic modes, the trigger captures the images on different shedding cycles. Therefore, the shedding cycle is constructed using POD analysis employing 1200 images. During self-excited acoustic resonance, the feedback cycle and the energy transfer between the sound and the flow fields makes the shedding mode more correlated and thus phase-locked PIV measurements are performed ([113], [51], [2], [114], [3]). The camera and the laser are synchronized on a double frame mode at which the camera captures pairs of images having the same phase on the acoustic pressure cycle. The acoustic pressure cycle is divided into eight phases. So, the camera captures 250 instantaneous pair of images every 45 degrees on the acoustic pressure cycle. The maximum particle displacement is captured within $\frac{1}{4}$ of the interrogation window used for vector calculation. This is achieved by tuning the time between the pulses. During the post-processing, any shadows or reflections was excluded from the field of view. For the first step, one pass was performed at an initial interrogation window size of 64 $\times$ 64 pixels with a 50% overlap. For the 2^{nd} and final steps, four passes were performed at a final interrogation window size of 24 $\times$ 24 pixels with a 50% overlap.

3.3 Results and discussion

3.3.1 Aeroacoustic response

In this section, the aeroacoustic response of the six investigated cases is discussed to define the different shedding modes interacting with the acoustic field. Figure 3.4 represents the aeroacoustic response of the six investigated cases as a waterfall plot

to be able to visualize the progression of the different Strouhal periodicity and their coupling with the different acoustic duct modes. Figure 3.4(a) corresponds to a rod with an aspect ratio of $l/h = 1$, the progression of the vortex shedding is clear with $\mathrm{St}_l \approx 0.14$. Lock-in starts to take place exciting the first acoustic mode of the duct at $U = 57$ m/s. The acoustic pressure reaches a peak value of $P_{rms} = 396$ Pa at $U = 60$ m/s. This pressure level is noticeably lower compared to the acoustic pressure generated during resonance excitation from a circular cylinder of an equivalent hydraulic diameter mohnayforce. This considerable discrepancy may largely be due to a fundamental divergence between circular and rectangular cylinders, underscored by the rectangular rod's four distinct separation points situated at its edges, leading to planar wall surfaces between adjacent edges. As a result, the complexity of the wake flow increases due to the emergence of two dominant separation regions within the shear layer: leading edge (LE) separation and trailing edge (TE) separation. Figure 3.4(b) corresponds to a rod with an aspect ratio of $l/h = 0.5$. Vortex shedding is progressing with distinctive peaks at $\mathrm{St}_l \approx 0.06$. Only the first acoustic mode was excited at the vortex shedding frequency coincidence with the first acoustic mode at $U = 115$ m/s generating acoustic pressure that reached a maximum value of $P_{rms} = 4209$ Pa at $U = 128$ m/s. Peaks appear at twice the frequency of the initial acoustic mode, reflecting the harmonic of this mode. It can be observed that there is a direct relation between the aspect ratio and the Strouhal number based on the rod length. This is attributed to the change in the flow structures in terms of the shear layer separation and roll-up in the wake and the recirculation zone topology around the rod which substantially changes when the aspect ratio changes. The Strouhal values for these 3 cases are in good agreement with the values reported in the literature ([57], [9], [94]).

For the cases with aspect ratio of $l/h = 2$, figure 3.4(c) corresponds to the case with all-sharp edges. The progression of the vortex shedding is clear with $\mathrm{St}_l \approx 0.18$

which is in good agreement with the values reported in the literature for the same aspect ratio ([143], [15], [53], [110]). At $U_\infty = 70$ m/s, the third acoustic duct mode was suddenly excited and lock-in took place. The Strouhal number which coincides with the third mode excitation is $\mathrm{St}_l \approx 0.54$. Nevertheless, this Strouhal periodicity was undetectable before the third mode excitation. The acoustic pressure reaches a peak value of $P_{rms} = 2494$ Pa at $U_\infty = 110$ m/s. Figure 3.4(d) corresponds to the case with the upstream-rounded edges. The shedding periodicity is far different from the first case as this case exhibits $\mathrm{St}_l \approx 0.5$. Interestingly, this Strouhal periodicity matches the Strouhal periodicity for the first case at which the third acoustic duct mode was excited. The first acoustic duct mode was excited at the typical frequency of coincidence reaching a peak pressure value $P_{rms} = 50$ Pa at $U_\infty = 34$ m/s. The peak pressure for this excitation is relatively low since the Strouhal number is high and the lock-in takes place at a low flow velocity. As a result, the flow doesn't have enough energy to couple with the sound field and generate high acoustic pressures. At $U_\infty = 91$ m/s lock-in to the third acoustic mode materialized. Reaching a maximum acoustic pressure value of $P_{rms} = 882$ Pa at $U_\infty = 102$ m/s. Figure 3.4(e) corresponds to the case with the downstream-rounded edges. The response of this case was quite similar to the all-sharp edges case in terms of the excitation and Strouhal periodicity. Clear vortex shedding progression is observed with $\mathrm{St}_l \approx 0.16$. Third acoustic duct mode is excited reaching a maximum acoustic pressure value of $P_{rms} = 2094$ Pa at $U_\infty = 110$ m/s. Figure 3.4(f) corresponds to the case with the all-rounded edges. The response of this case has the same behaviour as the upstream-rounded edges case with a Strouhal periodicity of $\mathrm{St}_l \approx 0.52$.The first acoustic duct mode was excited at the frequency coincidence with the Strouhal periodicity of 0.52. Acoustic pressure reached a peak pressure value of $P_{rms} = 125$ Pa at $U_\infty = 34.5$ m/s. Afterward, the shedding mode locked-out of the first acoustic duct mode and progressed till it locked-in with

the third acoustic duct mode reaching a maximum acoustic pressure of $P_{rms} = 2293$ Pa at $U_\infty = 92.5$ m/s.

Table 3.2 shows the normalized acoustic pressure at the peak of acoustic resonance for all the tested cases for the two self-excited acoustic modes. The normalized peak acoustic pressure indicates how strong the acoustic resonance is. The normalized acoustic pressure is given as follows:

$$P^* = \frac{2P_{rms}}{\rho U^2} \tag{3.4}$$

Also, $(U_{Max} - U_{Min}/U_{Max})$ is presented which is a normalized factor that demonstrates the lock-in range for each case. These two factors give a more in-depth understanding of the self-excitation strength and the intrinsic ability of the downstream flow structures to self-sustain acoustic resonance. For the first mode excitation, all the cases recorded nearly the same $P^* = 0.17 \approx 0.19$. However, the two-upstream rounded edges cases reached a low value of 0.06. This is due to the relatively low flow velocity at which lock-in take place. Also, the case C which is equivalent to AR= 0.5 reached the highest value of 0.41. This relatively high value is suggested to be associated with the more distant separation edges which creates larger recirculation region width in the cross-stream direction. Such wake flow structure allows a larger vortex cores to form which become more correlated and stronger during acoustic resonance excitation. For the third mode excitation, only the cases of AR=2 with different edges rounding excited the third mode either at the frequency of coincidence with the periodic flow structures or early excitation. Comparing all the cases to the sharp edges case, the upstream rounded edges case showed a significantly greater reduction in the P^* value compared to the downstream edges case. On the other hand, the case which involved rounding of all edges recorded a higher P^* value. This means that

there is a combined effect for rounding the upstream and downstream edges which have a positive effect on the flow-sound interaction mechanism. For AR=2, the two cases which involved sharp edges and downstream edges rounding showed a relatively wider lock-in range for the third acoustic mode compared to the other two cases of the same AR. Such finding emphasizes on the fact that upstream edges rounding have a limiting effect on the lock-in range.

Table 3.2: The normalized acoustic pressure P^* and the lock-in range U_{res}/U_{Max} for all the tested cases

Case	$P^*(1^{st}Mode)$	Δ $U_{res}/U_{Max}(1^{st}Mode)$	$P^*(3^{rd}Mode)$	Δ $U_{res}/U_{Max}(3^{rd}Mode)$
(a) Square	0.17	0.08	NA	NA
(b) Bluff rectangle	0.41	1.12	NA	NA
(c) all-sharp edges rectangle	NA	NA	0.33	0.47
(d) upstream-rounded edges rectangle	0.06	0.11	0.13	0.16
(e) downstream-rounded edges rectangle	0.19	0.06	0.26	0.43
(f) all-rounded edges rectangle	0.18	0.18	0.43	0.32

The aeroacoustic response suggests that the early third mode excitation does not materialize unless the rod length in the direction of the flow is above a certain threshold. Also, the upstream rounding has a substantial effect on pronouncing a completely different shedding mode in the wake with a Strouhal number similar to that observed for the shear layer instability reported in the literature for flow over cavities ([80], [86]). Moreover, this case showed a considerable reduction in the peak acoustic pressure during the third acoustic duct mode excitation compared with all-sharp edges case. For the downstream edge rounding, no observable differences were seen in terms of the peak acoustic pressure during resonance or the Strouhal periodicity compared to the case with all-sharp edges.

3.3.2 Dynamic lift force measurements

To quantify the hydrodynamic loading on the rods outside and during self-excited acoustic resonance, direct lift force measurements are conducted simultaneously with the acoustic pressure measurements to further understand the effect of edge rounding on the hydrodynamic loading and to study the effect of different shedding modes coupling with the duct transverse acoustic modes and their effect on the forces in the transverse direction. Also, measuring the hydrodynamic loading on the rod gives a fruitful insight into any potential changes in the shedding modes and wake structure. Figure 3.5 shows the r.m.s. of the lift force coefficient C_l' with the dominant shedding frequency superimposed on the secondary axis in order to identify the lock-in regions. It is important to note that all the peaks of the lift coefficient coincided with the acoustic pressure peak which set forth that there is a minimum acoustic energy losses along the acoustic pressure cycle. Also, the discontinuity in some of the C_l' figures is because these points were close to the setup mechanical resonant frequency and thus, they were eliminated.

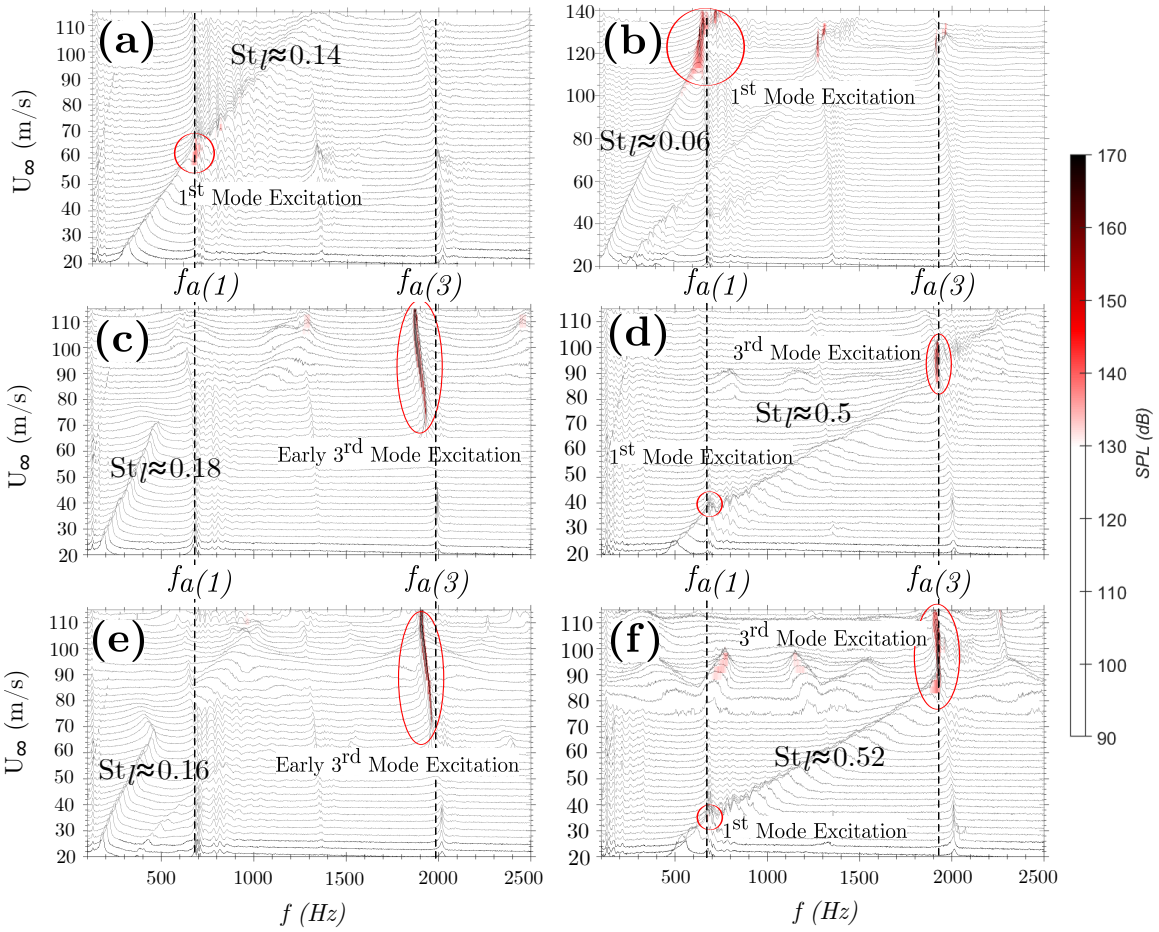

Figure 3.4: Acoustic pressure spectra for;(a) Square (b) Bluff rectangle (c) all-sharp edges rectangle, (d) two-upstream rounded edges rectangle, (e) two-downstream rounded edges rectangle, and (f) all-rounded edges rectangle.

Figure 3.5(a) corresponds to a rod with an aspect ratio of $l/h = 1$. The C_l' starts at around 0.62 and peaks to 0.75 and then drops again to 0.6. Such behavior was reported by Carassale et al. (2014) rounded2014 for the same range of Reynolds numbers referring to this behavior as a switch from subcritical to critical Reynolds number range. During the excitation of the first acoustic mode, the C_l' reached a maximum value of 0.82. Such rise is not significant compared to the off-resonance value. This is a result of the weak excitation in terms of the acoustic pressure. Figure 3.5(b) corresponds to a rod with an aspect ratio of $l/h = 0.5$. Before the onset of

resonance excitation, the C_l' exhibited the same trend as that for the aspect ratio of $l/h = 1$ peaking to a value of 1.7 and then dropping to a value of around 0.8. During the onset of the first acoustic mode excitation, the fluctuating lift coefficient reached a value of 3.2. Such value is 4 times higher than the value before the onset of acoustic resonance. This behaviour matches the same escalation ratio observed for a circular cylinder during acoustic resonance, as reported by Mohany & Ziada (2009) mohnayforce. Figure 3.5(c) corresponds to the all-sharp edges case. The C_l' starts hovering around 0.8 and then peaks to value around 1.2. A sudden decrease in the lift coefficient was observed as soon as early third-mode excitation took place and started to increase again reaching a peak value of 0.61 at the point of peak acoustic pressure. The main shedding mode was progressing before resonance at a Strouhal number $\mathrm{St}_l \approx 0.18$ and the Strouhal number at which the third mode was early excited is calculated and is equal to $\mathrm{St}_l \approx 0.54$. Figure 3.5(d) corresponds to the upstream-rounded edges case. The C_l' started with a value around 0.1. The first acoustic duct mode was excited at the frequency of coincidence between the shedding mode and the first acoustic mode frequency and the value of the C_l' peaked to 0.3 which is three times the value before the onset of resonance. Afterward, the third acoustic duct mode was excited at the frequency of coincidence between the shedding mode and the third acoustic mode frequency, and the value of the C_l' peaked to 0.17. The main shedding mode was progressing before resonance at a Strouhal number $\mathrm{St}_l \approx 0.5$. Figure 3.5(e) corresponds to the downstream-rounded edges case. The C_l' fluctuates around 0.6. A sudden decrease in the lift coefficient was observed as soon as early third mode excitation took place similar to the sharp-edges case and started to increase again reaching a peak value of 0.19. The main shedding mode was progressing before resonance at a Strouhal number $\mathrm{St}_l \approx 0.16$ and the Strouhal number at which third mode was early excited is calculated and is equal to $\mathrm{St}_l \approx 0.51$.

Figure 3.5(f) corresponds to the all-rounded edges case. The C_l' started with a value around 0.1. The first acoustic duct mode was excited at the frequency of coincidence between the shedding mode and the first acoustic mode frequency and the value of the C_l' peaked to 0.49. Afterward, the third acoustic duct mode was excited at the frequency of coincidence between the shedding mode and the third acoustic mode frequency and the value of the C_l' peaked to 0.29. The main shedding mode was progressing before resonance at a Strouhal number $St_l \approx 0.52$. Same as what was observed with the aeroacoustic response, cases (a) and (c) are similar and cases (b) and (d) are similar. During early third-mode excitation, the hydrodynamic loading is observed to have a substantially lower value compared to its value before the onset of early excitation. On the other hand, the hydrodynamic loading seemed to increase during first and third mode coincidence excitation compared to the values before the onset of resonance. Table 3.3 delineates the ratio between the C_l' at the peak of the two acoustic modes which were excited either early excited or excited at the coincidence and the average value outside of acoustic resonance. It is clear that for early excitation cases the ratio is less than one which means less hydrodynamic loading during resonance while for coincidence excitation cases the values are far more than one which means much higher hydrodynamic loading on the rod. This indicates that the early excitation of the 3^{rd} acoustic mode shown in figure 3.5(c, e) causes a sudden change in the wake structure around the rectangular rod.

3.3.3 Dynamic lift force decomposition

In order to self-excite acoustic resonance, the flow field shedding mode has to coincide with a duct resonant mode frequency. Also, the fluid intrinsically has to possess enough energy to excite this resonant mode since the self-excited acoustic resonance materializes based on energy exchange between the acoustic and flow fields. The flow

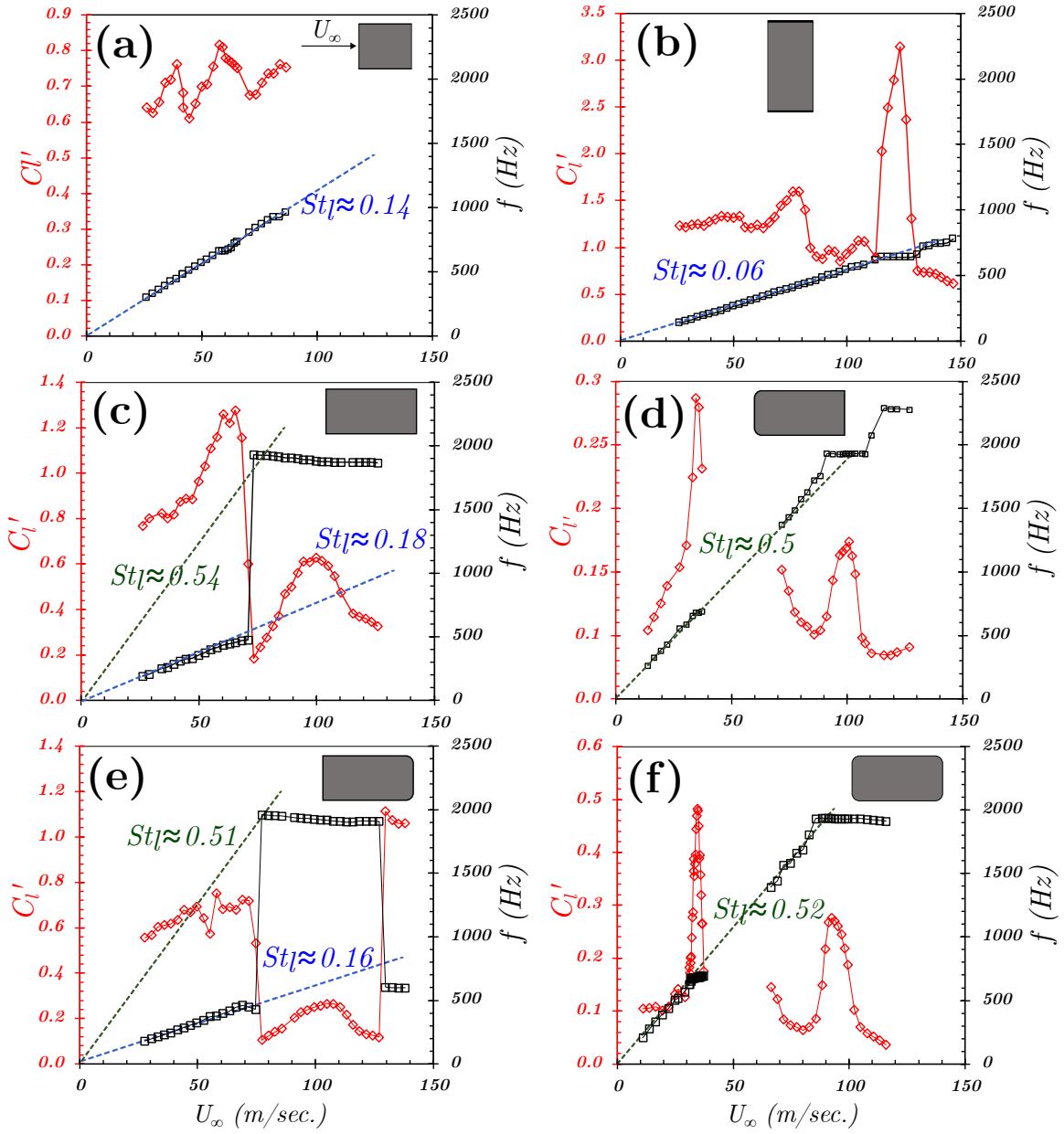

Figure 3.5: RMS of the the fluctuating lift coefficient (C_l') vs free stream velocity (U_∞) with the acoustic pressure dominant frequency superimposed on the secondary axis : (a) Square (b) Bluff rectangle (c) all-sharp edges rectangle, (d) two-upstream rounded edges rectangle, (e) two-downstream rounded edges rectangle, and (f) all-rounded edges rectangle.

Table 3.3: The ratio between the C_l' at the peak of the two acoustic modes which were excited either early or at the coincidence frequency and the average value outside of acoustic resonance.(1C) denotes first acoustic mode excitation at coincidence frequency; (3C) denotes third acoustic mode excitation at coincidence frequency; (3E) denotes early third acoustic mode excitation.

Case	$C'_{l(Average)}/C'_{l(1C)}$	$C'_{l(Average)}/C'_{l(3C)}$	$C'_{l(Average)}/C'_{l(3E)}$
(a) All edges sharp	N/A	N/A	0.75
(b) upstream rounded edges	2.63	1.7	N/A
(c) downstream rounded edges	1.91	N/A	0.33
(d) All edges rounded	4.45	2.63	N/A

field provides the energy needed to induce a dipole source vibrating in the transverse direction producing a high sound pressure level. This sound generated acts as an organizer to the flow field pronouncing more correlated and strong vortices. As shown in Figure 3.5, during acoustic resonance excitation, the hydrodynamic loading on the rod drastically changes which means that the sound field has a direct influence on the hydrodynamic loading on the cylinder. So, it is instructive to decompose the lift force to its out-of-phase and in-phase components to further understand the interaction between the flow and sound fields.

Since there is a distinct peak in the pressure spectrum which resembles the main shedding mode frequency $f_{Shedding}$, we can express the generated acoustic pressure as follows

$$p(t) = P_{\max} \sin\left(2\pi f_{Shedding} t\right) \tag{3.5}$$

From Figure3.3, we can assume that the dynamic lift force exerted on the rod is sinusoidal at the dominant shedding frequency $f_{Shedding}$. So, the dynamic lift force per unit length as a function of time is given as follows

$$F_L(t) = \frac{\rho U_\infty^2}{2} c_l' \sin\left(2\pi f_{Shedding} t + \varphi\right) \tag{3.6}$$

Where c_l' is the dynamic lift force coefficient, and φ is the angle between the dynamic lift force and the acoustic pressure. It is important to note that the phase angle is extracted for the acoustic pressure and lift force signal at the peak frequency $f_{Shedding}$.

Lighthill(1952) [62] stated that the sound observed from an unbounded flow depends on the stress fluctuations within the source region. The Navier-Stokes equation was rearranged in analogy to the aeroacoustics in an ideal flow. The fluctuations in the fluid density ρ is formulated as follows

$$\frac{\partial^2 \rho}{\partial t^2} - c_0^2 \nabla^2 \rho = \frac{\partial^2}{\partial x_i \partial x_i} (T_{ij}) \tag{3.7}$$

Where T_{ij} is the stress tensor including the turbulent, compressive and viscous stresses. c_0^2 is the speed of sound in the medium based on the fluid properties. At relatively low Mach numbers, the flow generates noise, this noise is modeled as a dipole source which resembles the hydrodynamic fluctuating forces that act on the fluid by the boundaries [23].

The difference between the fluid density ρ_o at the free stream and fluid density ρ at a specific point which is away from the sound source by a distance y is as follows

$$\rho - \rho_0 = \frac{1}{4\pi c_0^2} \frac{y_i}{y^2} \frac{\partial}{\partial t} F_i(t) \tag{3.8}$$

Where $F_i(t)$ is the force acting on the fluid by the boundary in the time domain.

So, as per Eqs.(3.5) and (3.6) we can decompose the dynamic lift force coefficient into in-phase orthognal and out-of-phase components:

$$\begin{aligned} c_l(t) &= [c_l' \cos(\varphi)] \sin(2\pi f_{Shedding} t) + [c_l' \sin(\varphi)] \cos(2\pi f_{Shedding} t) \\ &= c_{mh} \sin(2\pi f_{Shedding} t) - c_{dh} \cos(2\pi f_{Shedding} t) \end{aligned} \tag{3.9}$$

Analogous to the flow-induced vibration, the acoustic particle velocity is equivalent to the displacement of the rod [108]. So, the added negative sign in Eq.3.9 takes into consideration the fact that the acoustic particle velocity vector which is responsible for the energy transfer is out of phase with the acoustic pressure vector. The in-phase c_{mh} and out-of-phase c_{dh} components are expressed as follows

$$c_{mh} = c_l' \cos(\varphi) \tag{3.10}$$

$$c_{dh} = -c_l' \sin(\varphi) \tag{3.11}$$

The in-phase component c_{mh} is analogous to an added mass effect which resembles the bulk motion of the acoustic field with the flow momentum. The increase in the c_{mh} value means that the resonant oscillation frequency is expected to be lower. On the other hand, the out-of-phase component c_{dh} is analogous to an added damping effect in which a positive value means that the periodic shedding mode in the wake as a result of the fluid interaction with the rod is not contributing to sustaining the acoustic resonance, while if the value is negative this means the shedding instability is becoming more organized, hence result in a more strong acoustic resonance which is translated to higher sound pressure levels.

Figure 3.6 shows the in-phase c_{mh} and out-of-phase c_{dh} components of the dynamic lift coefficient for all the studied cases. The first column shows the in-phase c_{mh} component. It is clear that for the case of all-edges are sharp and the case of the two-downstream edges rounded that there is a severe dip in the in-phase component during the early third mode excitation. However, the two downstream edges rounded case showed a significant increase in the in-phase component during the first mode excitation. Even though, there is a significant sudden dip at the onset of the third mode, the in-phase component still showed a progressively increasing trend during the

third mode excitation which means that the added mass effect is still present during resonance. This is expected as from Figure 3.5 we can see a severe dip also in the value of the dynamic lift force coefficient during the early third mode excitation while it significantly peaks during the first mode excitation. Such behavior suggests that the shedding mode which early excites the third mode is completely different than the one which excites the first mode. For the two upstream rounded edges and the all-edges rounded case, we can see a significant increase in the in-phase component during the first and third acoustic mode excitation. This aligns with the excitation frequency for both modes which is slightly lower than the duct mode theoretical frequency which means that we have a positive added inertia effect during acoustic resonance. It is important to note that the peak value of the in-phase component for the two upstream edges rounded case is nearly half the peak value for all edges rounded case which is the same reduction ratio observed for the peaks of the acoustic pressure.

The second column shows the out-of-phase c_{dh} component of the dynamic lift force coefficient for all the studied cases. It is clear that for the case of all-edges sharp and the case of the two-downstream edges rounded that the out-of-phase component decrease to a negative value during early third mode excitation. This means that the flow instability is becoming stronger to sustain the acoustic resonance pressure cycle. Also, such observation suggests that the third acoustic mode acts as an external forcing source which is continuously exchanging energy with the flow field targeting the undetectable shear layer instability shedding mode and as soon as this shedding mode frequency coincides with the third acoustic mode frequency, acoustic resonance materialize. For the two upstream-edges rounded and the all-edges rounded cases, the out-of-phase component either increased and became positive or hovered around zero during the first and third mode excitation. Referring to figure 3.4, we can see

that the lock-in range for these two cases compared to the other two is significantly narrower. Similar behavior was observed for the upstream cylinder for two or more inline cylinders ([112], [71]). It is reported that such an increase in the out-of-phase component means that there is a positive added damping effect due to the vortex impingement on the downstream cylinders causing flow distortion in the gap. For these two cases, the Strouhal periodicity observed from the aeroacoustic response in Figure 3.4 is within the shear layer instability range. So, the analogy here is that the shear layer separates from the rod surface and impinges somewhere on the rod surface then interacts with the trailing rounded edge, the same as the shear layer impingement on the downstream cylinders in an inline cylinders arrangement. According to Howes [42], the bluff body leading edge is the main contributor to the acoustic energy generated which is expended in sustaining the flow vorticity. This means that the upstream corners rounding has an attenuation effect on the acoustic energy generated field during resonance which in turn weaken the flow-sound energy exchange. This will be further discussed in the phase-locked flow characteristics section.

3.3.4 Time-averaged flow topology

Time-averaged flow characteristics in the wake of all rod cases with aspect ratio of $l/h = 2$ is studied in this section to further elaborate the effect of different edge rounding on the wake dynamics. Figure 3.7 shows the time-averaged normalized streamwise velocity ($\overline{u}/U_\infty$) contours with streamlines superimposed in the x–y plane at $U_\infty = 27.6m/s$. To outline the recirculation zone, a red contour line is drawn which is defined by $\overline{u}/U_\infty = 0$. The vortex formation length is defined as the distance between the origin and the end of the recirculation region along the x-axis ([59], [147]).

As shown in figure 3.7, all the cases exhibit a symmetric topology in the wake

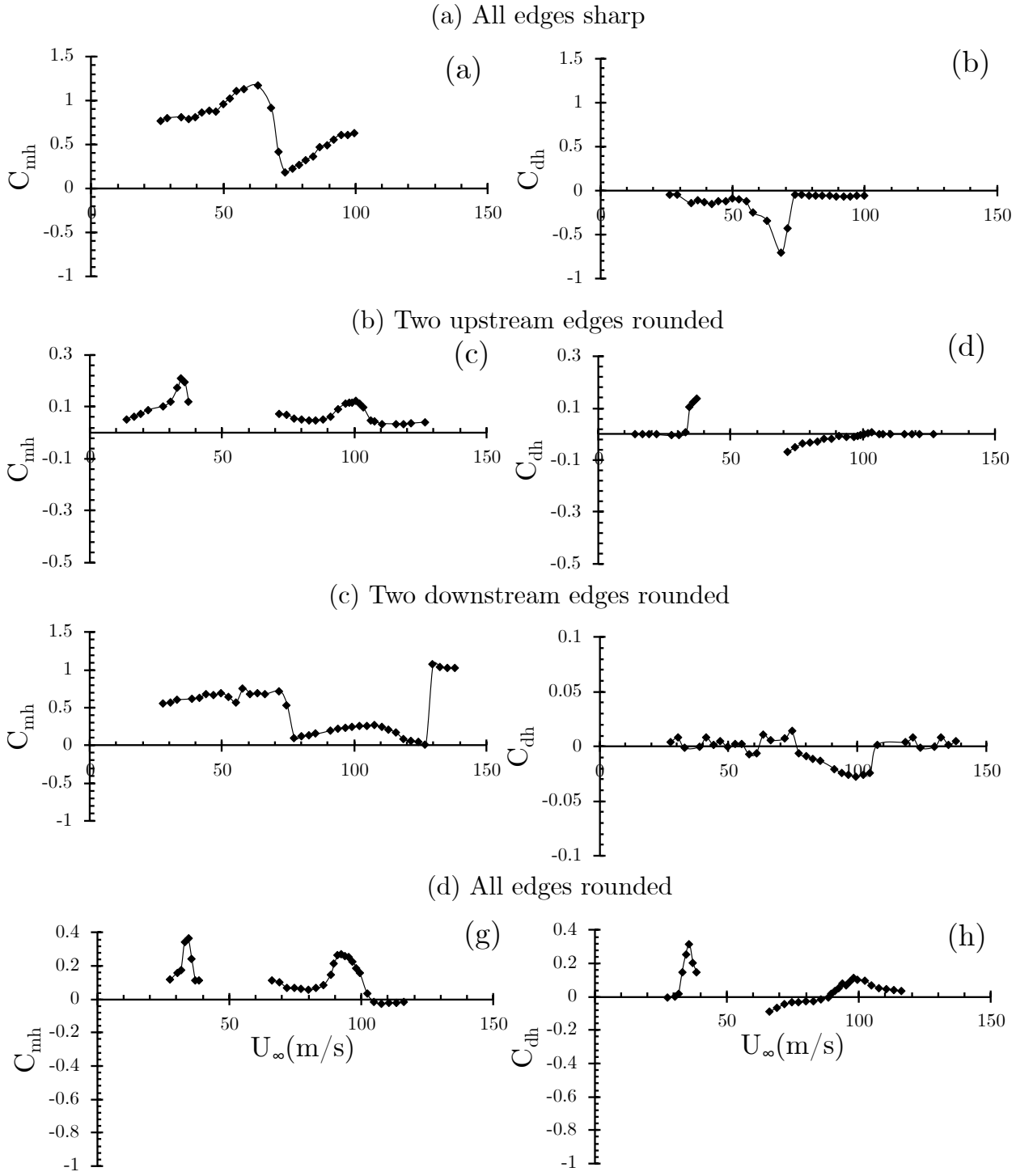

Figure 3.6: In-phase c_{mh} and out-of-phase c_{dh} lift coefficient components for all the studied cases

in terms of the recirculation bubble and velocity recovery. The all-sharp edges case and the two-downstream rounded edges case exhibit a relatively large primary and secondary recirculation region and longer vortex formation length compared to the other two cases. The primary recirculation region is defined as the region on the top and bottom walls of the rod and the secondary recirculation region is defined as the region downstream in the near wake. The presence of such two regions is because of the forced separation of the flow from the leading sharp edge. The strong curvature of the streamlines in both regions generates a severe pressure gradient on the top and bottom walls of the rod which in turn increases the hydrodynamic loading on the rod DNS. This is evident from figure 3.5(c, e) as these two cases showed average C_l' of 0.8 and 0.6, respectively, outside of acoustic resonance. In figure 3.7 comparing cases (b) and (d) with cases (a) and (c), the recirculation region is substantially smaller and less curved and so does the vortex formation length. Also, the primary recirculation region on the rod walls is absent and the velocity recovery in the wake extends over a smaller region in the transverse direction. This results in a lower hydrodynamic loading on the cylinder which is evident from figure 3.5(d) and (f) as these two cases showed approximately the same C_l' values outside of acoustic resonance which was around 0.1. From figure 3.4 we can see that the cases which involved rounding of the upstream edges (d and f) showed a completely different dominant Strouhal number which is close to the shear layer instability values reported in the literature ([85]). This major difference is due to the upstream edge rounding which delays the separation and the main shedding mode switches from vortex shedding to shear layer instability hence, eliminating the primary recirculation region and considerably reducing the vortex formation length.

The shedding process is a result of velocity fluctuations in the near wake which is a result of the complex interaction between the free stream and the rod. The

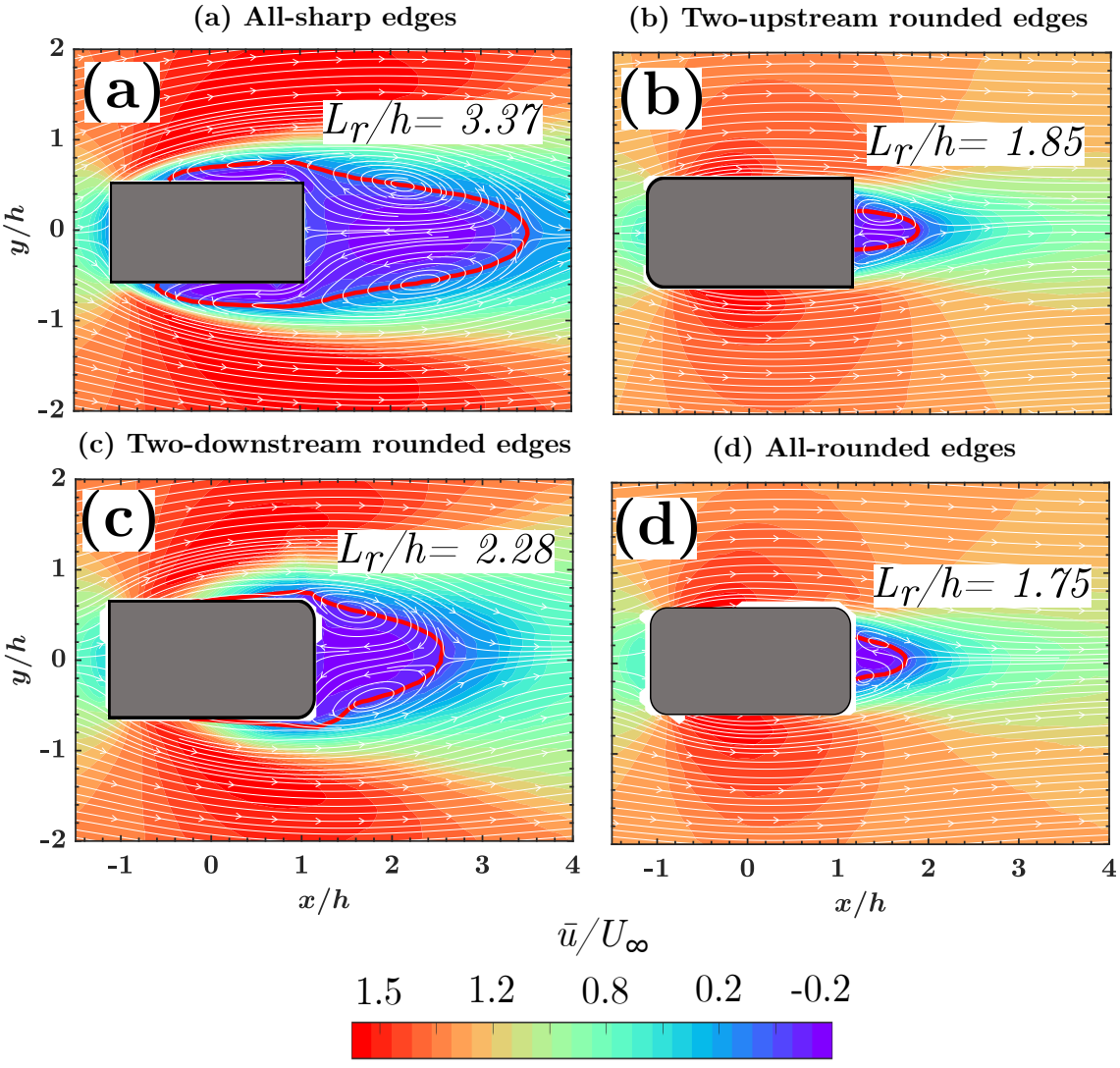

Figure 3.7: Time-averaged normalized streamwise velocity ($\bar{u}/U_\infty$) contours with streamlines superimposed in the x–y plane at $U_\infty = 27.6 m/s$. (a) all-sharp edges, (b) two-upstream rounded edges, (c) two-downstream rounded edges, and (d) all-rounded edges. The red contour line represents $\bar{u}/U_\infty = 0$, which outlines the recirculation region. The streamlines are represented by contour lines.

shear and normal Reynolds stresses in the wake are an explicit interpreter of the velocity fluctuations. So, to further understand the shear layer interaction with the rod's different edges rounding, shear Reynolds stress and normal Reynolds stress are shown in figure 3.8. The figure clearly shows that the cases cluster into two groups. all-sharp edges and the downstream-rounded edges exhibit nearly the same behavior, while the two upstream rounded edges and all edges rounded cases manifest the same behavior. This observation agrees well with figure 3.7.

The first column of Figure 3.8 shows the streamwise normalized Reynolds stress ($\overline{u'u'}/U_\infty^2$) fluctuations. Figure 3.8(a, e) show a lobe-like structure emanating from the leading edge with high Reynolds stress values which is symmetric about the rod centreline. This lobe outlines the shear layer which is separated from the upstream sharp edges. The gradient increases from the inner to the outer envelope due to the formation of vortices and the primary recirculation bubble. It is important to note that figure 3.8(a) which corresponds to all-sharp edges showed relatively lower shear Reynold stress values inside the lobes compared to figure 3.8(e). This suggests that the rounding of the downstream edges enhances the rolling of the inner shear layer into the wake. However, the sharp edges disrupt the inner shear layer rolling and decrease the shear layer momentum [61]. Such Reynolds stress distribution in the wake emphasizes the fact that the vortices formation for these two cases is due to the separation of the shear layer from the leading edge and rolling in an alternate manner in the near wake forming the large-scale vortex shedding single street. On the other hand, figure 3.8(c) and (g) show a different distribution compared to the two former discussed cases. The lobe-like structure is absent and the high Reynolds stress values are concentrated downstream of the rod in the wake. This suggests that upstream edges rounding delays the leading edge separation. This will be further corroborated in the next section showing the POD phase-averaged vorticity field.

The second column of figure 3.8 shows the transverse normalized Reynolds stress ($\overline{v'v'}/U_\infty^2$) fluctuations. The red line denotes the boundary of the recirculation region and is plotted by extracting the points of $u = 0$ and outlining these points by an iso-contour. The maximum value of the $\overline{v'v'}/U_\infty^2$ is located along the wake centreline for all the investigated cases. Figure 3.8(d, h) which involve a sharp leading edge showed a much narrower Reynolds stress contour compared to the other two cases which involve a rounded leading edge. On the other hand, the two cases which involved downstream edge rounding showed a relatively higher maximum $\overline{v'v'}/U_\infty^2$ compared with the two other cases which possess a sharp downstream edge. This suggests that the downstream rounding increases the cross-stream velocity fluctuations.

Table 3.4 shows the value and location ($L_{\overline{v'v'}/U_\infty^2}/h$) of the peak normal Reynolds stress ($\overline{v'v'}/U_\infty^2$) and the C_l' value at the velocity ($U_\infty = 27.6m/s$) at which the time-averaged analysis is conducted. We can see that there is a strong positive correlation between the location of the peak normal Reynolds stress ($\overline{v'v'}/U_\infty^2$) and the C_l' value. As the location of the peak normal Reynolds stress is further downstream, the gradient of velocity fluctuation downstream extends across a longer distance which causes a stronger curvature in the streamlines inside the secondary recirculation region which in turn induces a stronger pressure gradient which increases the fluctuating hydrodynamic load on the rod. This agrees well with the streamlines shape in figure 3.7. It is worth noting that the location of the peak normal Reynolds stress ($\overline{v'v'}/U_\infty^2$) does not coincide with the end of the recirculation zone for all the cases since the flow entrainment inside the recirculation region decreases the velocity fluctuations due to the more uniform flow circulation.

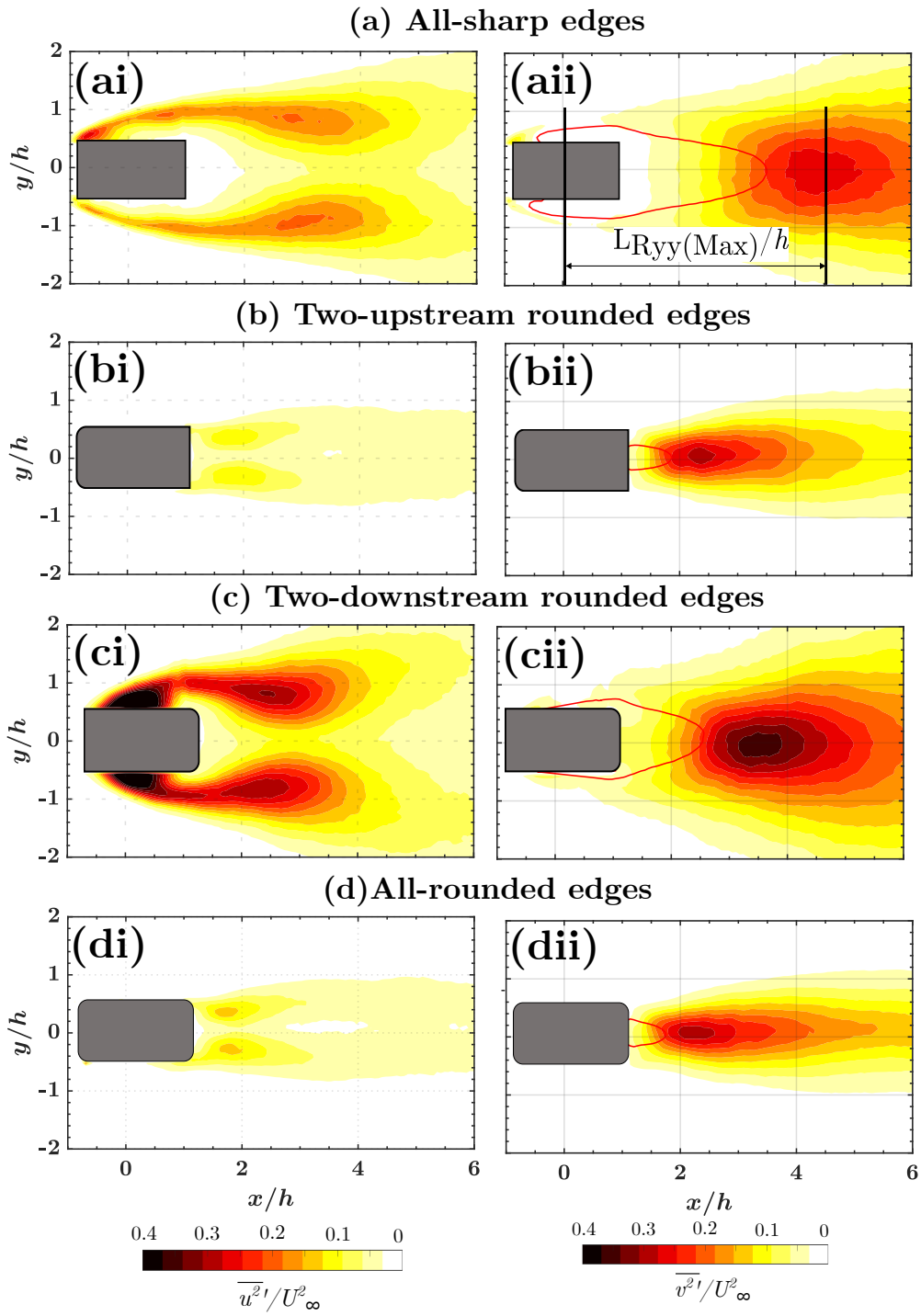

Figure 3.8: Time-averaged Reynolds shear stress ($\overline{u'u'}/U^2_\infty$) and normal stress ($\overline{v'v'}/U^2_\infty$) at $U_\infty = 27.6m/s$. (a, b) all-sharp edges, (c, d) two-upstream rounded edges, (e, f) two-downstream rounded edges, and (g, h) all-rounded edges. The red contour line represents $\overline{u}/U_\infty = 0$, which outlines the recirculation region.

Table 3.4: The value and location ($L_{\overline{v'v'}/U_\infty^2}/h$) of the peak normal Reynolds stress ($\overline{v'v'}/U_\infty^2$) and the C_l' value at the time-averaged analysis velocity ($U_\infty = 27.6m/s$)

Case	$L_{\overline{v'v'}/U_\infty^2}/h$	$\overline{v'v'}/U_\infty^2$	C_l'
(a) All edges sharp	3.91	0.26	0.79
(b) upstream rounded edges	2.22	0.28	0.12
(c) downstream rounded edges	3.06	0.38	0.59
(d) All edges rounded	1.69	0.32	0.1

3.3.5 Phase-averaged flow topology

This section discusses the intrinsic flow topology in the near wake of the rounded edge cases in comparison with the sharp edge case for the aspect ratio of $l/h = 2$. To construct the unsteady flow characteristics in the near wake, proper orthogonal decomposition (POD) analysis [117] is conducted based on the progressive snapshots of the flow field using the PIV system. For each case, 1200 snapshot-based on POD are captured for each case. The goal is to capture each mode energy, the temporal evolution of the flow structures in the wake, and the spatial flow features. In order to achieve that goal, the POD modes $\Psi_k(x)$, eigenvalues (λ_k), and time coefficients (a_k) are obtained ([138], [125]) The mode number (k) depicts the contribution of each mode to the wake turbulent kinetic energy ([134], [95]) figure 3.9(a, b) present the absolute and cumulative mode energies, respectively. For bluff body wakes, the first two POD modes capture the preponderance of the intrinsic turbulent kinetic energy in the flow ([50], [134]). As shown in figure 3.9, for the four investigated cases, the first two modes represent 42-53% of the total turbulent kinetic energy. These two POD modes are associated with the main shedding mode in the wake. The rest of the modes resemble about 5% of the total kinetic energy which is generated from small-scale vortical structures before coalescence and random turbulent motion. For the sharp edges case and the upstream edges rounding case, the first POD modes

pair captures 42% of the total turbulent kinetic energy. However, for the downstream edges rounding and all edges rounding cases the first POD modes pair captures 53% and 47% of the total turbulent kinetic energy, respectively. Rounding the downstream edge increases the susceptibility of the shear layer interaction between the upstream and downstream edges. As a result, there is more turbulent kinetic energy generation. This is evident by referring to figure 3.8 and 3.4, the two cases which involved downstream edges rounding showed relatively higher Reynolds stresses in the streamwise and transverse directions compared with the other two cases. The Reynolds stresses in both directions are a direct measure of the velocity fluctuations which are directly correlated to the wake turbulent kinetic energy.

The POD method proposed by van Oudheusden et al. (2005) [134] is implemented to obtain the phase-averaged data. Luckily, the majority of the TKE is concentrated in the first POD mode pair. So, a low-order model could be enacted to obtain the periodic phase-averaged component of the flow. To do so, the mean flow along with the first pair of the POD modes are utilized to obtain the reconstructed flow field(U_{rec}), so, it becomes:

$$U_{rec}(x,\phi) = \overline{U}(x) + a_1(\phi)\psi_1(x) + a_2(\phi)\psi_2(x) \tag{3.12}$$

where $\psi_n(x)$ is the spatial features , a_n is the temporal coefficient, and $\overline{U}$ is the time-averaged velocity vector. $n = 1, 2$ denotes the first pair of POD modes that are implemented in the analysis as stated later. Figure 3.9(c) shows a scatter plot of the temporal coefficients (a_1 and a_2) from the snap-shot POD post-analysis data for the sharp edges case. The data is scattered shaping an ellipse having the following equation:

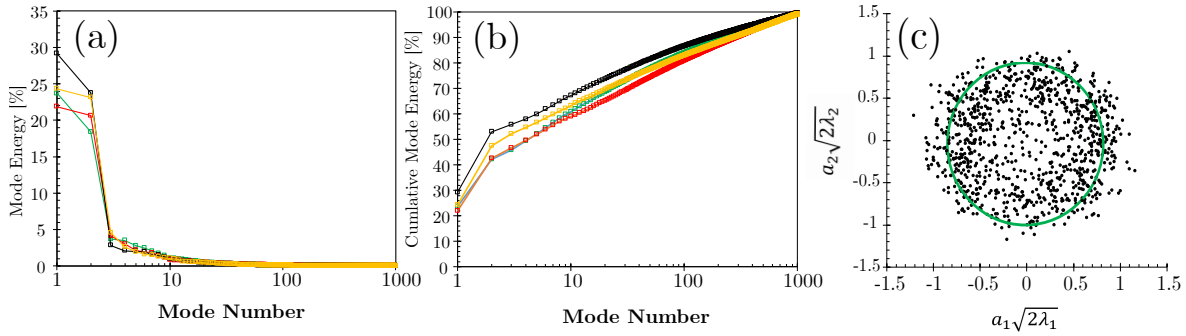

Figure 3.9: Energy distribution of the POD modes in the turbulent kinetic energy: (a) mode energy (λ_k), (b) cumulative mode energy, and (c) Scatter plot of the temporal coefficients a_1 and a_2 from the POD analysis performed on the PIV data for the all edges sharp case. Black open square-downstream rounded edges; yellow open square-all edges rounded; green open square-sharp edges; red open square-upstream rounded edges

$$\frac{a_1^2}{2\lambda_1} + \frac{a_2^2}{2\lambda_2} = 1 \tag{3.13}$$

λ_1 and λ_2 are the eigenvalues of the first pair of POD modes. To obtain the instantaneous flow field phases, the following equation is used:

$$\phi = \tan^{-1}\left[\frac{\sqrt{\lambda_2}a_1}{\sqrt{\lambda_1}a_2}\right] \tag{3.14}$$

All the instantaneous flow field data is sorted into a number of bins. Eqn.4.5 is utilized to obtain the number of bins. In order to capture the evolution of the shear layer and its rolling into the wake, all the instantaneous flow fields are separated into 16 bins. As a result, the phase difference between every two consecutive phases is 22.5°.

To further analyze the shedding modes in the wake and understand the vortex formation and propagation in the wake, figure 3.10 and 3.11 shows four equidistant phase-averaged snapshots of the vorticity field with the flow streamlines superimposed at $U_\infty = 27.6m/s$. It is clear that again the four cases cluster into two groups,

the all-sharp edges and downstream-rounded edges cases showed a similar wake and shear layer behavior, while the upstream rounded edges and all edges rounded cases pronounced almost the same shedding pattern. The first group which involved a sharp leading edge showed the separation of the shear layer from the leading edge with no interaction with the rod surface or the trailing edges, then rolling up into the wake forming positive and negative vortex cores in the wake. Gerrard (1966) [35] stated that this is a result of mutual induction between the two separated shear layers from the leading edge and rolling into the wake. The shear layer starts rolling approximately between 2.5 to 3.5 rod heights downstream, which agrees with the results shown in figure 3.7 in terms of the vortex formation length. Moreover, the streamlines distortion and movement in the transverse direction are more pronounced and stronger for these two cases. This match the findings in figure 3.8 as these two cases have higher global normal Reynolds stress in the transverse direction compared with the other two cases which is translated to a much higher fluctuating lift coefficient compared with the other two cases.

The second group which involved upstream edges rounding showed the formation of vortex cores right at the trailing edges forming a two-street vortex shedding in the wake having relatively smaller vortex cores compared to the other group. The rounding of the upstream edge eliminates the definitive separation point which forces the formation of the free shear layer, instead, it triggers the instability of the shear layer impinging on the rod surface and interacting with the trailing edge forming weaker vortices in the wake.

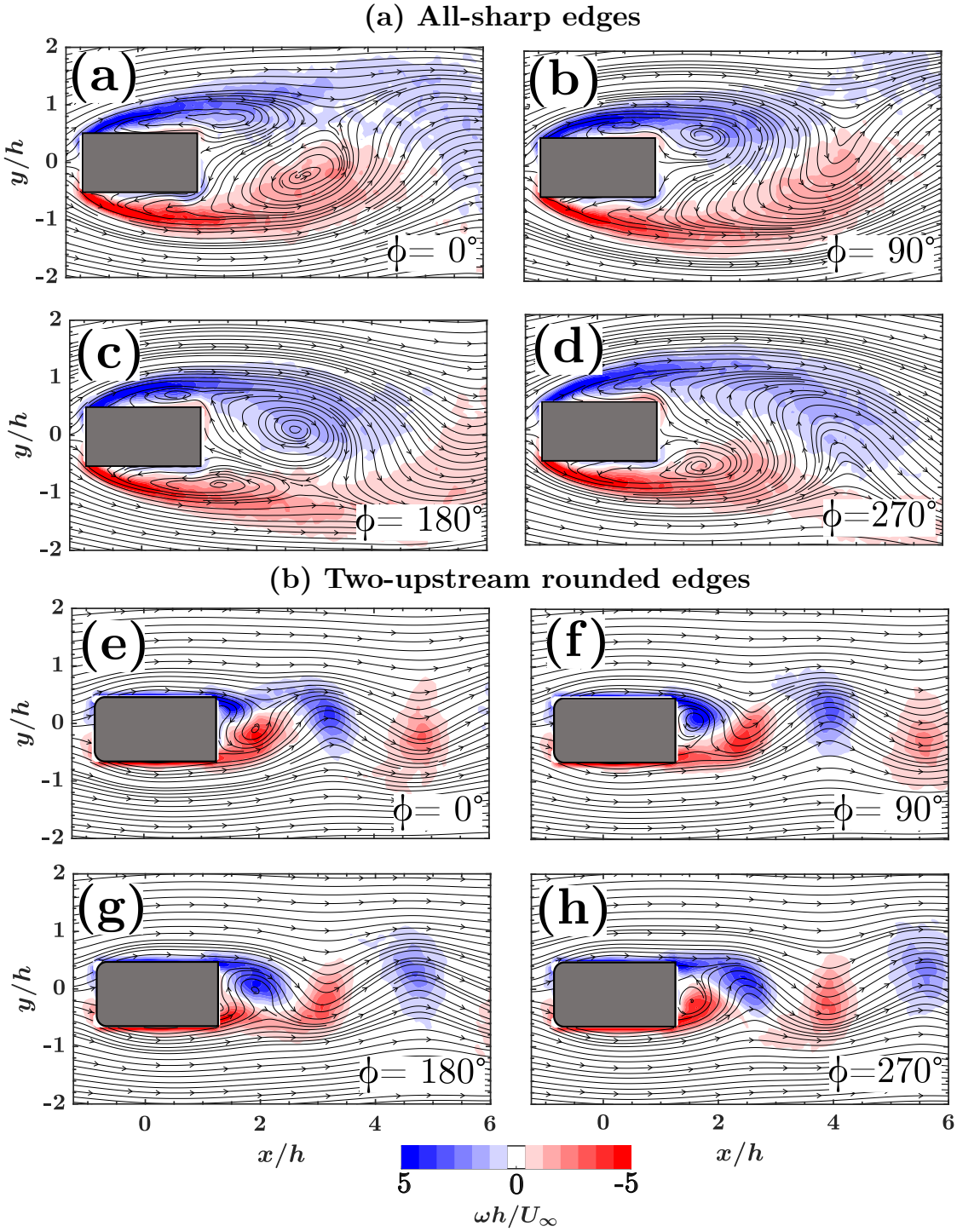

Figure 3.10: Four equidistant Phase-averaged vorticity fields with the flow streamlines superimposed at $U_\infty = 27.6m/s$. (a) all-sharp edges, (b) two-upstream rounded edges.

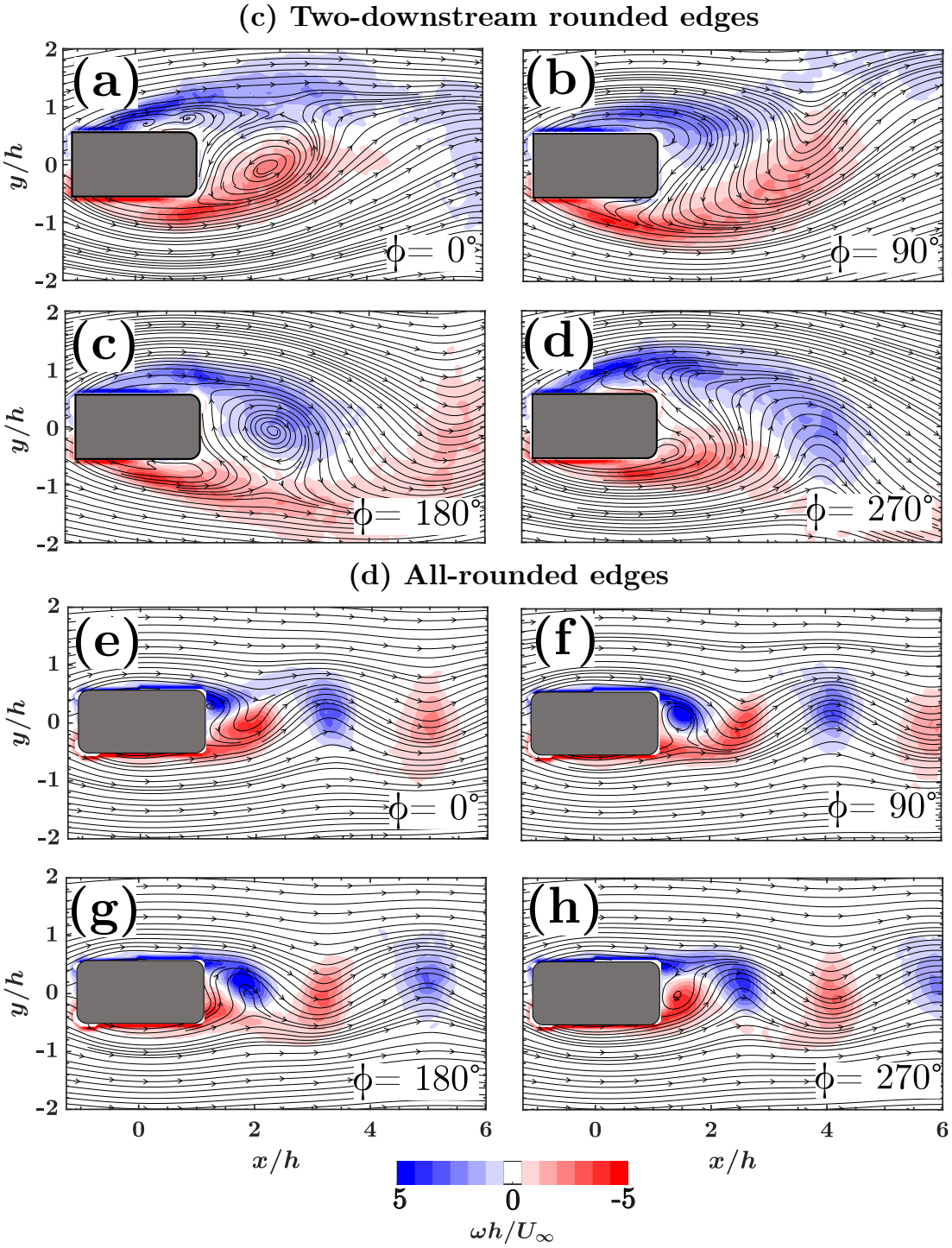

Figure 3.11: Four equidistant Phase-averaged vorticity fields with the flow streamlines superimposed at $U_\infty = 27.6m/s$ (c) two-downstream rounded edges, and (d) all-rounded edges.

3.3.6 Phase-locked flow topology during self-excited acoustic resonance

Figure 3.10 shows the phase-locked vorticity field over one acoustic pressure cycle at the peak of acoustic pressure value during the third mode excitation for the cases with upstream-rounded edges and downstream-rounded edges. In order to effectively distinguish individual vortices, we employ the Q-criterion, a tool that accentuates regions of high vorticity correlating with distinct vortex formations. Originating from the velocity gradient tensor, the Q-criterion delineates regions where the vorticity magnitude surpasses the rate of strain. In our analysis, we establish a Q-value threshold of 0.005. This designated value facilitates the robust detection of large-scale vortices characterized by significant recirculation patterns. Both showed the same vortical structure in the wake. Vortices form on the rod surface and interact with the trailing edges forming a two-street shedding pattern. However, before the onset of resonance, we can see from figure 3.10 that the downstream-rounded edges case exhibits a single shedding street. . Bearman and Obasaju (1982) [8] observed the same switching in the shedding pattern downstream for a square rod during forced-induced vibration at a reduced velocity equal to 4 and a forced oscillation amplitude of only 10% of the rod length, l. Moreover, the pressure coefficient in the centre of the base changed from - 1.6 when the body was stationary to -0.54 when the body was forced to oscillate. This yields to a reduction ratio of about 3 in the base pressure which is close to the reduction ratio observed in the fluctuating lift coefficient shown in figure 3.5(c). This is a striking similarity between the mechanisms of flow-induced vibration and flow-induced acoustic resonance. Noteworthy, similar analogy was observed by Mohany and Ziada (2009) [72]. They observed that the phase jump between the acoustic pressure and the lift force during acoustic resonance excitation exhibits

the same behaviour as that between the lift force and the cylinder displacement for the case of forced-induced vibration reported by Carberry et al. (2001) [17]. Such finding confirms that the dominant shedding mode for the rod case with upstream-rounded edges, which is named shear layer instability mode, is what triggers early excitation of the third acoustic mode for the rod case with downstream-rounded edges. This suggests that this mode is intrinsically present but masked out before resonance excitation by the dominant vortex shedding mode downstream of the rod.

Comparing the vorticity field downstream of the two cases, it is obvious that the downstream-rounded edges case has a more defined vortex structure with less distortion in the cylindrical structure and enhanced vorticity content. This is interesting since for the case of the downstream-rounded edges the third acoustic mode was excited by a completely weak masked instability. However, in the case of upstream-rounded edges it is excited by the dominant wake shedding mode. According to Howes (1980) [42], the bluff body leading edge is the main contributor to the acoustic energy generated which is expended in sustaining the flow vorticity. This means that the upstream corners rounding has an attenuation effect on the generated acoustic energy during resonance which in turn weaken the flow-sound energy exchange and this yields a weaker and distorted vorticies which is confirmed from figure 3.12.

3.4 Conclusion

In this chapter, the characteristics of the shedding modes and dynamic lift force of rectangular rods with different aspect ratios and edge geometry subjected to cross-flow were experimentally investigated during and before the onset of different transverse duct acoustic modes excitation. Direct measurements of the dynamic lift force were conducted. Phase-averaged and phase-locked PIV measurements were carried out to

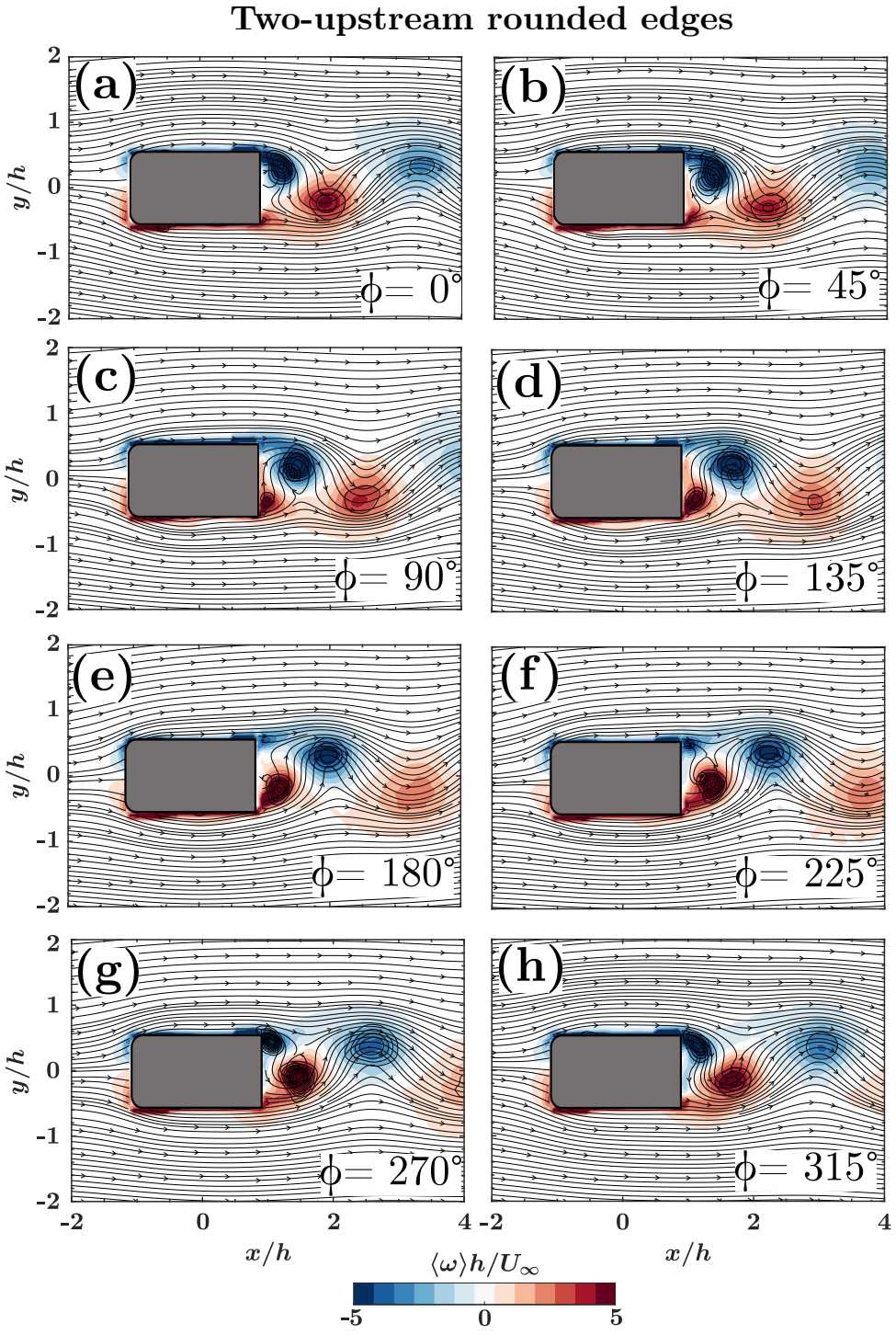

Figure 3.12: Eight equidistant phase-locked vorticity fields with the flow streamlines superimposed in the wake during third acoustic mode excitation over an acoustic pressure cycle at its peak value for the two upstream rounded edges case

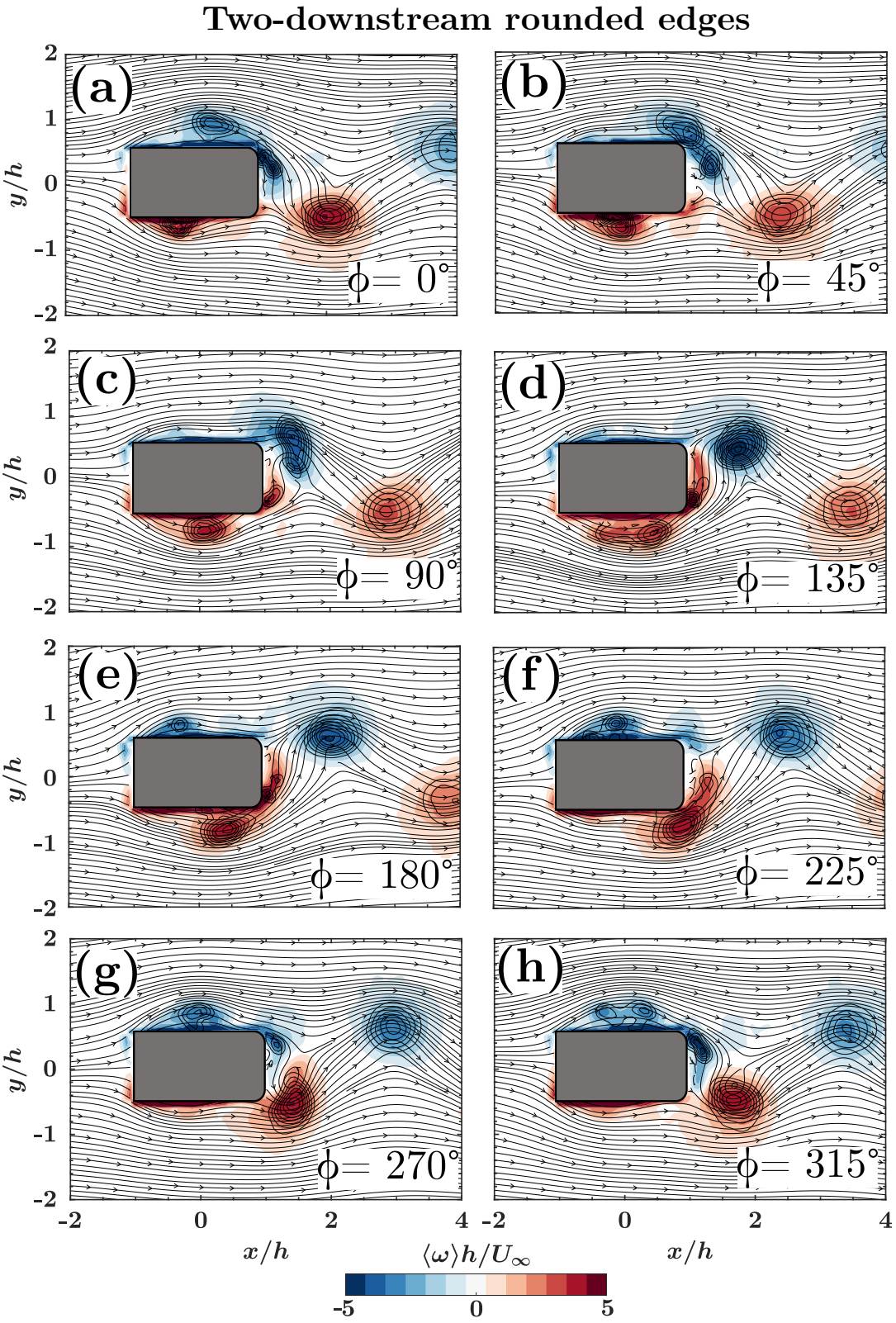

Figure 3.13: Eight equidistant phase-locked vorticity fields with the flow streamlines superimposed in the wake during third acoustic mode excitation over an acoustic pressure cycle at its peak value for the two downstream rounded edges case.

characterize the time-averaged and phase-locked flow topology in terms of the main shedding modes and the shear layer behavior. The main findings of this investigation are illustrated in Figure 3.14 and summarized as follows:

1. The case of $l/h = 1$ and $l/h = 0.5$ showed typical vortex shedding progression and lock-in to the first acoustic mode with Strouhal numbers equal to 0.14 and 0.06, respectively.

2. For the cases of $l/h = 2$, the all-sharp edges and the downstream-rounded edges cases showed similar aeroacoustic response. Both showed a Strouhal number of $\mathrm{St}_l \approx 0.16 - 0.18$ and sudden excitation of the third acoustic mode. On the other hand, the upstream-rounded edges case and the all-rounded edges case showed a Strouhal number of $\mathrm{St}_l \approx 0.5 - 0.52$ and normal excitation of the first and the third acoustic modes at the frequency coincidence with the wake shedding.

3. The coupling mechanism between the duct higher acoustic modes and the masked shear layer instability depends on the rod length, l. So, to early excite the third transverse acoustic mode of the duct, the rod length l must be sufficiently long.

4. Before the onset of resonance, the upstream edge rounding seemed to have a significant reduction effect on the dynamic lift force as both cases which involved upstream edge rounding had $C_l' \approx 0.1$ while the other two cases that had sharp upstream edges reported $C_l' \approx 0.8 - 0.6$.

5. During acoustic resonance excitation, there was a significant reduction in the dynamic lift coefficient for the two cases which early excited the third acoustic mode compared to the values before the onset of resonance.

6. Phase-averaged PIV measurements showed that outside of acoustic resonance excitation, the sharp-leading edge plays a vital role in the shear layer separation and pronouncing a specific shedding mode in the wake. Rounding the leading edge resulted in producing shear layer instability mode in the wake of the rod eliminating the primary recirculation region, while the sharp leading edge case showed the typical shear layer separation from the leading edge and rolling up into the wake shedding vortices.

7. Phase-locked PIV measurements confirmed that the early excitation of the third acoustic mode for the sharp-edges and the downstream-rounded edges cases is due to the coupling between the shear layer instability shedding mode with the duct acoustic mode, although this mode was completely masked before the onset of the early third mode excitation, the third acoustic mode acted as an external forcing source that enhanced this mode and coupled with it to materialize acoustic resonance.

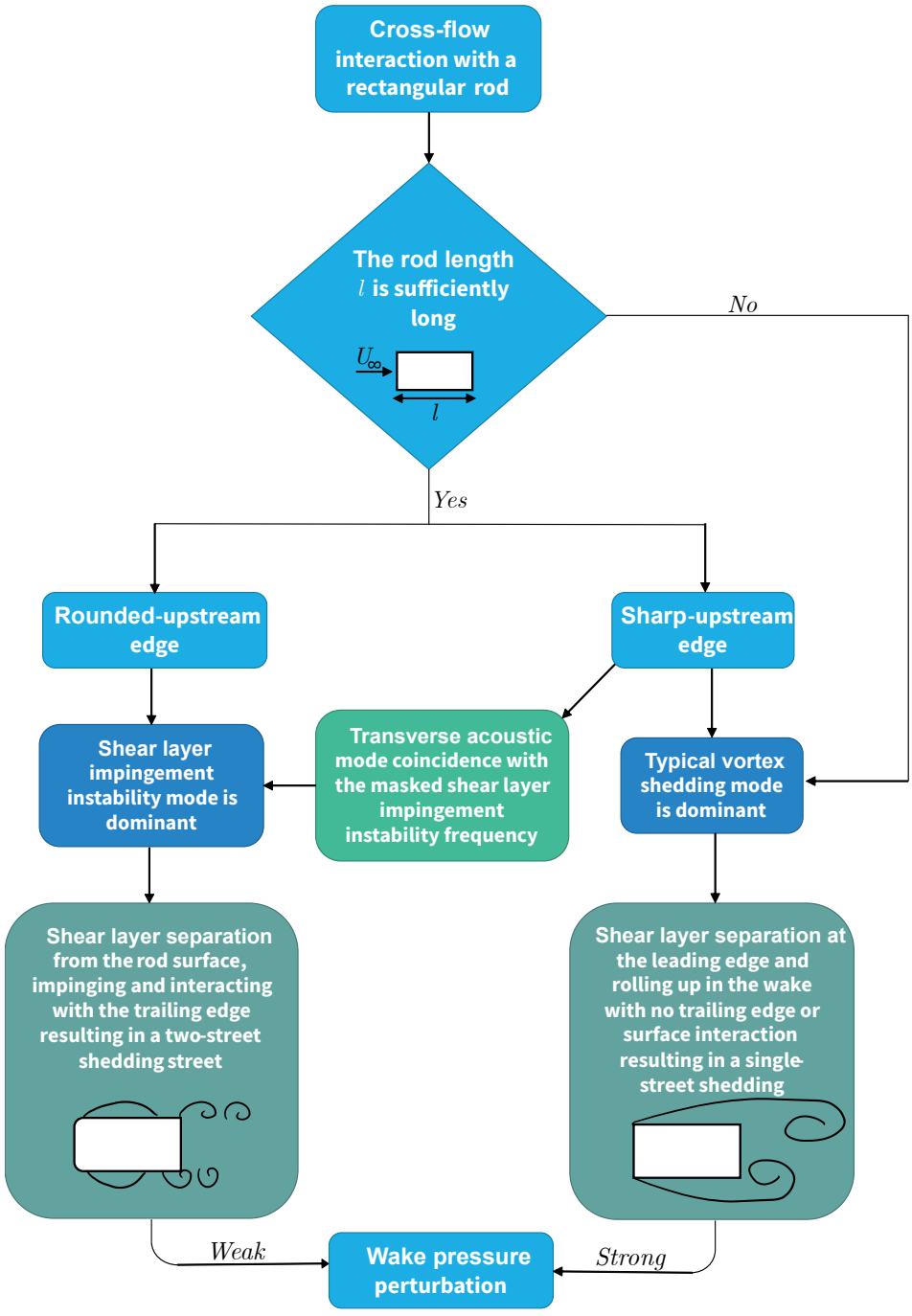

Figure 3.14: A Schematic that shows the effect of the rod length in the flow direction, upstream edge rounding, and the acoustic excitation on pronouncing different shedding modes in the wake of rectangular rods.

Chapter 4

Self-selection of Flow Instabilities by Acoustic Perturbations Around Rectangular Cylinder in Cross-Flow

This chapter is submitted to Journal of Fluid Mechanics under the name: A. Mohany, A. Shoukry , and L. Pastur. Self-selection of Flow Instabilities by Acoustic Perturbations Around Rectangular Cylinder in Cross-Flow. Journal of Fluid Mechanics (2023)

4.1 Introduction

Numerous studies have been conducted to reveal the underlying flow physics in the wake of bluff bodies in cross-flow. Bluff bodies exhibit complex flow structures in their wakes due to the unsteady flow separation and impinging mechanism that re-

sults in the formation of periodic vortex streets. Better understanding of these intrinsic flow features will clarify their effect on the surface and wake pressure distributions which directly influence the hydrodynamic loading on the bluff body. Such knowledge is crucial for the development of more efficient flow control techniques and consequently preventing undesirable coupling between the vorticiy shedding from the bluff body with an acoustic or a structural vibration mode. Most of the studies that have been conducted on bluff bodies over the last few decades have concentrated on circular cylinders ([96], [37], [115], [141]) and square cylinders ([135], [9], [84], [98]; [126], [57], [63], [130]), while relatively less attention was given to rectangular cylinders in cross-flow despite their wide use in various industrial applications. Rectangular cylinders are commonly utilized in trashracks placed at hydraulic intakes of hydropower plants to serve as filters and prevent debris from entering hydraulic systems, pylons, bridge decks, towering structures, offshore platforms, etc. Some of these applications have experienced failures due to a coupled interaction between the flow instabilities around the rectangular cylinders with a structural vibration mode [see for example: [22], [54], [137]]. Therefore, the main objective of this work is to investigate the flow instabilities around rectangular cylinders at different flow incidence angles and demonstrate experimentally, for the first time, the ability of acoustic perturbations to self select and modulate the flow instabilities to engage in a feedback loop of oscillation.

One fundamental distinction between circular and rectangular cylinders arises from the presence of four well-defined separation points located at the edges of the rectangular cylinder, resulting in flat wall surfaces between the adjacent edges. Consequently, the wake flow becomes more intricate due to the presence of two predominant separation regions in the shear layer (i.e. the leading edge (LE) separation and the trailing edge (TE) separation). For elongated rectangular cylinders with an aspect

ratio $AR = l/h > 3$, where the aspect ratio (AR) represents the ratio between the streamwise dimension (l) and the cross-stream dimension (h), both the LE and TE shed vortices at high Reynolds numbers. The shedding from both edges exhibits synchronization to the same frequency, indicating the existence of a feedback loop between the pressure perturbations at the TE caused by vortex roll and formation, and the separation of the shear layer at the LE. Additionally, it is observed that the Strouhal number demonstrates a stepwise behavior with respect to the aspect ratio (AR) ([84], [77], [91], [68], [127]). The stepwise behviour is attributed to a locked feedback mechanism between the frequency of the LE and TE vortices, with a wavelength that is directly correlated to the streamwise dimension of the cylinder. The mode progression is associated with the parameter "n", representing the number of vortices present on the lateral face of the rectangular cylinder between the leading and trailing edges. For rectangular cylinders with aspect ratios (AR) between 3 and 5, the first mode of the impinging leading-edge vortex (ILEV) is manifested, characterized by one LE vortex on the lateral faces (i.e. $n = 1$). As the aspect ratio increases, the wavelength also increases until reaching a threshold that allows for the transition to the second ILEV mode (i.e. $n = 2$), which means two distinct vortex cores are formed along the lateral face.

In their pioneering work, Nakamura & Nakashima (1986) [77] introduced the concept of the leading edge (LE) vortex shedding and termed the overall shedding mechanism as impinging-shear-layer instability. They proposed that this instability is independent of the mutual induction between the two shear layers originating from the lateral faces of the cylinder. To verify this hypothesis, a splitter plate was inserted into the wake of a rectangular cylinder with an aspect ratio (AR) of 5. Remarkably, the shedding frequency remained unchanged both before and after the insertion of the splitter plate. Similarly, Shabaan & Mohany (2022) [114] recently observed the same

shedding mode during self-excited acoustic resonance for a rectangular cylinder with an AR as low as 2. These findings underscore the presence of this shedding mode even at low aspect ratios and further highlight its nature as a resonant oscillation of the fluid.

Naudascher & Rockwell (1994) [81] classified three distinct vortex shedding regimes for rectangular cylinders based on the aspect ratio (AR). Type I, known as leading-edge vortex shedding (LEVS), is characterized by a separation bubble at the leading edge of the body. Type II, referred to as "impinging leading-edge vortex (ILEV) instability," involves the shedding of leading-edge (LE) vortices from the separation bubble at the leading edge, which subsequently interact with the trailing-edge (TE) vortices. Type III is trailing-edge vortex shedding (TEVS), where vortices detach from the trailing edges of the rectangular cylinder. Hourigan et al. (2001) [41] later discovered a hybrid shedding type that can occur at Reynolds numbers below 2000, representing a combination of the ILEV and TEVS shedding modes. They observed that the TE vortices are forced to modulate their frequency to align closely with the shedding frequency, enabling the shedding of LE vortices within one complete shedding cycle with proper phasing. This accommodation of the full shedding cycle wavelength along the length of the cylinder occurs due to the synchronization between the LE and TE shedding modes.

Building upon Nakamura& Nakashima (1986) [77] work, the ILEVS mode is considered a resonant oscillation of the fluid that can be triggered by coupling with a resonant acoustic wave within an enclosure. The feedback control is established through the pressure perturbation originating from the flow field discontinuity at the trailing edge, which is a result of vortex production at the cylinder's trailing edge. The formation of the LE vortices occurs due to the interaction of the shear layer with the leading edge. When the LE vortex passes the TE, a localized pressure pulse is

generated due to strain concentration at a specific point. This pulse subsequently travels upstream, triggering the shedding of a LE vortex from the leading edge shear layer.

Parker & Welsh (1972) [93] revealed in their study that there could be four possible vortex shedding patterns depending on the cylinder's aspect ratio. (I) cylinders with ($AR < 3.2$) experience flow separation that occurs at the LE with no reattachment to the plate's surface and the LE separated shear layer rolls into the wake forming a regular vortex shedding street, which is in other words named LEVS. (II) cylinders with ($3.2 < AR < 7.6$) exhibit a trailing edge interaction with the LE vortices producing ILEV/TEVS mode. (III) cylinders with ($7.6 < AR < 16$) experiences shear layer reattachment somewhere on the lateral face before the trailing edge which forms a separation bubble that sheds vortices randomly. This shear layer behavior is said to produce irregular shedding patterns with no distinct vortex shedding street. (IV) cylinders with ($16 < AR$) experiences similar behavior to those in (III) however, the vortices shedding from the separation bubble dissipate before reaching the trailing edge. Additionally, they observed a regular shedding pattern exist under acoustic resonance conditions for high aspect ratios. [79] suggested that although for high aspect ratios ($AR > 12$) there is no organized shedding pattern that can be detected, the organized shedding pattern observed by Stokes & Welsh (1986) [121] is a manifestation of the ILEV inherited in the flow but the acoustic field acted as an external forcing source to excite it. Contrarily, Mills et al. (2003) [67] put forth a contrasting hypothesis referred to as the trailing-edge shedding. They contested that the shedding pattern, detected under resonant conditions in the study of Stokes & Welsh (1986) [121], was not an instance of ILEV shedding as proposed by Nakamura et al. (1991) [79] but rather a different shedding mechanism. Thus, one of the primary objectives of our research is to navigate through these conflicting viewpoints

and clarify the effect of the acoustic resonance on the unsteady flow structures around a rectangular cylinder. Such an endeavor will deliver a more unified understanding of the underlying shedding mechanisms at both resonant and non-resonant conditions.

For higher Reynolds numbers, two studies conducted by Okajima (1982a) [84] and Igarashi (1984) [49] have revealed that flow characteristics and aerodynamics remain relatively insensitive to the upstream Reynolds number beyond a value of approximately 10^4. However, the angle of incidence has a notable effect on shifting the separation points, thereby altering the free shear layer separation and resulting in wake rolling. This shift in separation points can ultimately impact the hydrodynamic loading, the Strouhal number of dominant shedding patterns, and heat transfer coefficients. Furthermore, several studies have reported that changes in the shedding pattern in the wake can occur due to variations in shear layer separation dynamics caused by the angle of incidence ([118]; [144]). Kinsely (1990) [57] thoroughly reviewed Strouhal number data from the literature for various aspect ratios and incidence angles. The general trend observed in most cases showed a rapid increase in the Strouhal number and a significant decrease in the aerodynamic forces at small angles of attack ($\alpha < 15°$). This trend is thought to be associated with the shear layer separation and subsequent reattachment to the cylinder's windward lateral face. The reattachment of the shear layer reduces pressure fluctuations in the wake, reducing the aerodynamic forces imposed on the rod. Other studies reported similar trends for Strouhal number and aerodynamic forces ([105]; [29]; [107]).

Compared to the studies reporting on vortex shedding modes and aerodynamic forces, fewer investigations have focused on characterizing the velocity field and wake dynamics of rectangular cylinders. Work by several authors ([28], [64], [65], [90], [45], [60]) employed various flow visualization techniques, such as particle image velocimetry (PIV) and laser Doppler velocimetry (LDV), to accurately construct the near

and far wake velocity fields, time-averaged turbulence properties, and phase-averaged streamline patterns. These approaches provide valuable insights into the wake flow topology, allowing for choosing the optimum configuration for different industrial applications and the development of effective techniques for suppressing vortex shedding. Igarshi (1984) [49] implemented surface-oil flow and smoke to study the flow around a square cylinder at different angles of incidence. He divided the wake flow patterns into four different regimes based of the incidence angle, i.e., (I) $0° \leq \alpha \leq 5°$: symmetric flow with perfect separation, (II) $5° \leq \alpha \leq 13°$: asymmetric flow with separation, (III) $14° \leq \alpha \leq 35°$: reattachment flow type, and (IV) $35° \leq \alpha \leq 45°$: wedge flow type. [134] reported the velocity field around a square cylinder using particle image velocimetry at four different angles of incidence. For $\alpha = 0°$ the boundary layer bifurcates into two branches from the midpoint on the square section in the cross-stream direction and then separates from the two leading sharp edges. The free shear layer rolls into the wake forming two distinct recirculation regions. A primary region in the wake which is due to the large-scale vortex formation in the wake and a secondary region at the cylinder's lateral faces in the stream-wise direction. Between $\alpha = 5°$ and $\alpha = 10°$ the two recirculation regions merged together into one region in the wake. Flow reattachment was observed between $\alpha = 10°$ and $\alpha = 15°$. The topological analysis of this study did not precisely match the flow topology equation outlined by [48] due to the difficulties in capturing the near-surface flow topology because of the laser reflections and insufficient spatial resolution or image count in the PIV window size. To compensate for the flow visualization challenges, multiple investigators have conducted computational fluid dynamics studies on square cylinders to capture the near-surface, wake topology, and unsteady flow characteristics ([129], [106], [20]).

In light of the previous discussion, for square and rectangular cylinders, the shear

layer behavior and the periodic flow structures in the wake are found to be sensitive to the aspect ratio and angle of incidence. However, most of the studies focused on high aspect ratios ($3 < A.R < 16$) as it is assumed that below this range the shear layer is said to be stable with natural shedding process occurring in the wake. Thus, the objective of this study is to employ particle image velocimetry (PIV) techniques in a high-speed wind tunnel to investigate the flow around a rectangular cylinder with an aspect ratio $AR = 2$ with different angles of incidence under different conditions: during self-excited acoustic resonance and outside of resonance excitation. In an attempt to explore whether the excited resonant mode reported by Stokes % Welsh (1986) [121] is due to a coupling with the inherent 'ILEV' instability as reported by Nakamura et al. (1991) [79] or it is a different vortex shedding mechanism as proposed later by Mills et al. (2002) [67]. This will help us gain a comprehensive understanding of the flow dynamics and vortices' impingement mechanisms from various edges of the rectangular plates, which will provide valuable insight into how an acoustic resonant field can influence and alter the interaction of vortices with different edges. Furthermore, it will shed light on the modulation occurring between the leading and trailing edge vortices. Acoustic resonance, being a global feedback mechanism, plays a crucial role in modulating the overall system frequency. The detailed analysis and observations from this study will contribute to a better understanding of the complex flow behavior and the impact of acoustic resonance on the flow patterns around rectangular cylinders.

4.2 Experimental Setup

4.2.1 Wind tunnel facility

Experiments were conducted within an open-loop wind tunnel. The wind tunnel consists of a test section measuring 762 mm in length, 254 mm in height, and 127 mm in width. This test section is made out of acrylic to allow for flow visualization.

Figure 4.1 presents a schematic representation of the case examined in the study with the faces and nodes label that will be used throughout the study. In order to ensure uniform flow distribution in the spanwise direction, pressure measurements were conducted at 11 different locations along the span of the cylinder, covering a wide range of Reynolds numbers. The findings indicated that the mean base pressure coefficient exhibited minimal spanwise variation, falling within the experimental uncertainty of the measurements. All tested cases were positioned at a distance of 381 mm from the parabolic bell mouth entrance. At this specific location, hot-wire measurements were conducted, revealing that the transverse flow uniformity deviated by a maximum of 1% from the free stream velocity. The FFT of the natural turbulence spectrum showed no observable peaks within the frequency range of interest. Throughout the velocity range, the maximum turbulence intensity was carefully measured and determined to be below 0.8%. The experiments were conducted under controlled environmental conditions, maintaining a temperature of $25°C$ and 50% humidity. Monitoring of the indoor climate was carried out using an indoor climate sensor to ensure consistent conditions throughout the experiments. To achieve accurate control of the incidince angle, a precisely laser-cut acrylic window is utilized in conjunction with a dial mechanism. The dial allows for rotation and locking at specific orientations by employing a countersunk screw and a nut externally to the wind tunnel. Careful attention is given to ensure seamless integration of the dial and

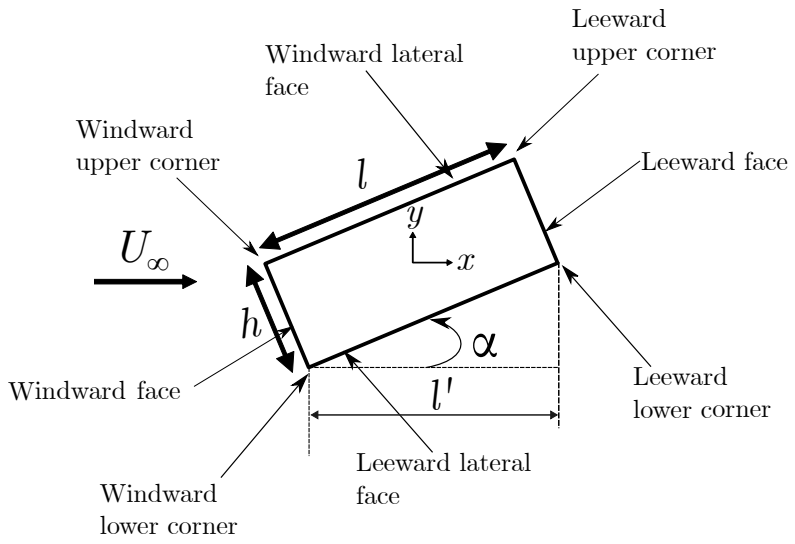

Figure 4.1: Schematic of the rectangular cylinder geometry with faces and nodes label

window, both of which were meticulously aligned with the acrylic walls of the test section. This alignment was implemented to promote smooth airflow and minimize turbulence intensity within the test section.

4.2.2 Acoustic pressure measurements

Acoustic pressure signal is recorded for 120 seconds for each measurement throughout the entire velocity range, encompassing speeds from 20 m/s to 150 m/s, with incremental steps of 2.76 m/s. The velocity range corresponds to a Reynolds number, based on the streamwise length, ranging from $Re_l = 3.5 \times 10^4$ to 2.5×10^5, when the cylinder's angle of incidence is zero. This is achieved with the aid of a flush-mounted pressure microphone which is strategically positioned on the top wall of the wind tunnel right above the middle of the rod. This position corresponds to the maximum pressure amplitude of the transverse acoustic mode. This was determined in a separate experiment using an array of flush-mounted microphones on the top wall at different streamwise positions. The details are not shown here for the sake of brevity.

A sampling frequency of 20 kHz is employed which is far below the targeted shedding frequencies. Welch's modified periodogram method, incorporating a 50% overlap and a resolution of 1 Hz, is employed to analyze the pressure signal and generate the frequency spectrum using Fast Fourier Transform. To isolate and accurately capture the desired pressure values, a band-pass filter with a range of ±50 Hz centered around the dominant frequency peak is applied. This filtering process allows for the extraction of the relevant pressure information. The resulting filtered pressure signal is then utilized to calculate the root mean square value of the pressure (P_{rms}) which is then normalized and given as P^* using the following equation:

$$P^* = \frac{2P_{rms}c}{\rho U_\infty^3}, \tag{4.1}$$

where c is the speed of sound (m/s), ρ the air density (kg/m^3), and U_∞ the mean flow speed (m/s).

As the shedding patterns develop in the cross-stream direction inducing pressure perturbations in the transverse direction, the cylinder is exactly placed in the middle of the duct height (i.e. acoustic particle velocity antinodes of the $\lambda/2$, $3\lambda/2$ and $5\lambda/2$ modes). So, only the odd-numbered transverse acoustic modes can be excited. Figure 4.2 illustrates a schematic representation of the acoustic pressure distribution within the duct for the excited odd-numbered transverse modes. The theoretical value of these modes can be calculated using the following equations:

$$f_{a(1)} = \frac{c}{2H}, f_{a(3)} = \frac{3c}{2H}, f_{a(5)} = \frac{5c}{2H} \tag{4.2}$$

Moreover, it provides a direct measurement of the frequencies at which vortex shedding occurs in the wake. When the frequency of the vorticity shedding coincides with the natural frequency of an acoustic duct mode, resonance may be established.

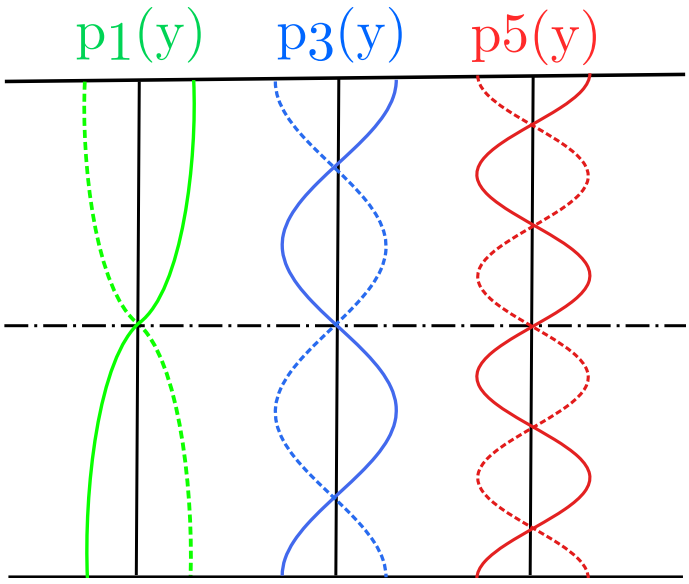

Figure 4.2: Schematic representation of the acoustic pressure distribution inside the duct for the odd-numbered transverse modes.

If the flow excitation energy is higher than the acoustic damping of the system. When acoustic resonance materializes a feedback loop between the flow and sound fields, results in the amplification of acoustic energy and the generation of audible acute noise. The interplay between the flow dynamics and acoustic phenomena has a profound effect in shaping the wake topology during resonance excitation.([12], [70], [52]).

4.2.3 Particle image velocimetry (PIV)

In this study, LaVision system is employed (Particle Image Velocimetry) to capture and analyze the instantaneous velocities of the flow field within the two-dimensional laser sheet domain. Figure 4.3 shows the full PIV setup. The utilization of the PIV system ensures precise and comprehensive velocity measurements, facilitating a thorough investigation of the flow dynamics under resonant and non-resonant conditions.

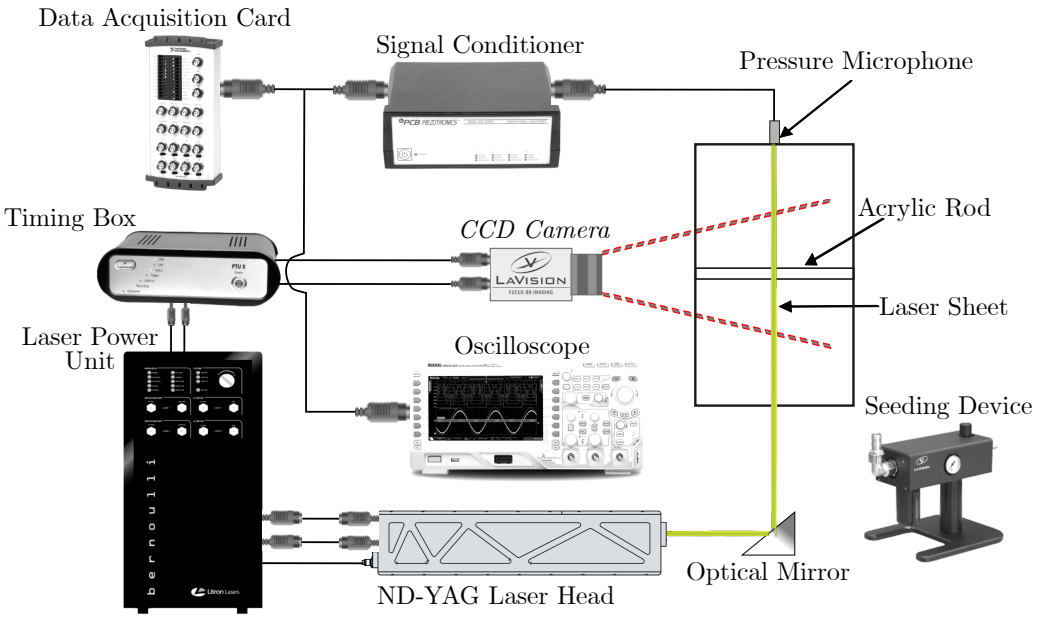

Figure 4.3: Schematic of the full PIV setup.

Flow field seeding and illumination

The flow seeding in this study involved the use of atomized Di-Ethyl-Hexyl-Sebacat, with a maximum particle size of $2\mu m$. To illuminate the two-dimensional plane, a Double-head 532 nm ND:YAG laser operating in a double pulse mode was employed. The laser was set to a frequency of 15 Hz with a peak power output of 200 mJ. To achieve a thin and well-defined laser sheet, the laser beam was directed towards an optical mirror, which efficiently scattered the laser light. A precise linear actuation mechanism was employed to position the laser sheet in the middle of the x-y plane. The laser sheet illuminated the test section from the bottom, passing through an optical-grade acrylic wall. To control the pulse duration, a mechanical shutter was incorporated into the laser head, enabling phase-locked measurements at specific frequencies. This allowed for accurate synchronization of the PIV measurements with the flow dynamics. For data processing, autocorrelation techniques were employed. Image pairs from two successive frames were processed, with specific regions such as

the cylinder area and surface reflections, if any, masked out to ensure accurate analysis. This ensured the extraction of reliable velocity information from the captured images.

Image capturing and acquisition

To capture the flow images, a 12-bit camera operating in a double frame mode was utilized. The camera had a maximum resolution of 2752x2000 pixels. In order to enhance the image acquisition process, a green light filter was installed on the camera, matching the wavelength of the laser used. The camera was directly connected to a PC, enabling real-time image transfer and analysis. The camera shutter was synchronized with the laser pulsing, ensuring precise timing for capturing the flow field. This synchronization was achieved through the DaVis software, which facilitated the coordination between the camera and the laser. To improve the accuracy of the flow measurements, dynamic filters were applied during the data processing stage. These filters were designed to eliminate background noise and remove any false vectors from the analyzed flow field. The filters relied on the image intensity variation as a criterion for identifying and deleting faulty vectors, ensuring that only reliable and meaningful data points were retained for further analysis.

To conduct measurements during off-resonance conditions, a series of images were captured representing various shedding cycles. To reconstruct a consistent shedding cycle, Proper Orthogonal Decomposition (POD) analysis was employed using a dataset comprising 1200 images. This allowed for the identification and extraction of the dominant flow structures and shedding patterns.

Phase-locked Particle Image Velocimetry (PIV) measurements are performed during self-excited acoustic resonance to capture the shedding mode in a synchronized manner. To achieve this synchronization, the acoustic pressure cycle is used as a ref-

erence signal. This signal is captured by the flush-mounted microphone in real-time and displayed on an oscilloscope for visualization. The signal gain is adjusted through the oscilloscope to optimize the timing. A timing box then locks the frequencies of the camera and the laser to the acoustic pressure cycle frequency. By dividing the acoustic pressure cycle into eight phases, the camera captures pairs of images at consistent intervals. Specifically, 250 instantaneous pairs of images are captured, with each pair corresponding to a phase interval of 45 degrees on the acoustic pressure cycle. This approach ensures that the PIV measurements are performed at precise and consistent phases of the acoustic resonance.

Imaging and post processing

The image acquisition and post-processing are carried out using DaVis 10.0 software. To extract accurate velocity information, the interrogation window technique is applied in two steps. In the first step, a single pass is performed with an initial interrogation window size of 64×64 pixels and a 50% overlap. This step helps capture the overall flow features and provides an initial estimation of the velocity field. For the second step, four passes are performed using a smaller interrogation window size of 24×24 pixels with a 50% overlap. This finer resolution allows for a more detailed analysis of the flow field and improves the accuracy of velocity measurements. To ensure high-quality results, post-processing techniques are employed. Faulty vectors are identified and removed, and denoising filters are applied to obtain a smooth flow field. In regions where illuminated particles are missing, dynamic interpolation techniques are utilized to estimate particle displacements based on the surrounding particles' motion. Spatial sliding filters are also applied to further enhance the quality of the flow field. Depending on the specific requirements of each case, different sliding filters such as Gaussian, minimum, and maximum filters are utilized to optimize the results.

These filters help in reducing noise and refining the spatial distribution of the velocity field.

4.3 Results and discussion

4.3.1 Flow under non-resonant condition

Strouhal number of natural vortex shedding

Figure 4.4 illustrates the Strouhal number $St_{h'}$, normalized by the projected streamwise dimension, corresponding to the natural vortex shedding periodicity from a rectangular cylinder at different flow incidence angle. The Strouhal number, derived from the Fast Fourier Transform (FFT) analysis of the acoustic pressure signal, accurately mirrors the dominant shedding mode. Initially, the Strouhal number stands at a value of 0.9 for zero angle of incidence. As the cylinder begins to tilt, the Strouhal number sharply ascends to around 0.18, indicating substantial alterations in the wake flow characteristics, which are discussed in detail in this section. At an incidence angle of approximately $\alpha \approx 60°$, the Strouhal number trend shows an inflection point and begins to descend, reaching a value of about 0.15 at $\alpha = 90°$. This observation underscores a significant transformation in the flow topology beyond the symmetric wedge angle, which is around $\sim 63°$ for cases with an aspect ratio (AR) of 2. The Strouhal number aligns well with existing literature, reflecting both the values and the trend associated with changes in the angle of incidence as reported by Kinsely (1990) [57].

Time-averaged flow topology

The time-averaged flow characteristics are studied under non-resonant conditions, at different angles of incidence to understand how the cylinder tilting influences the

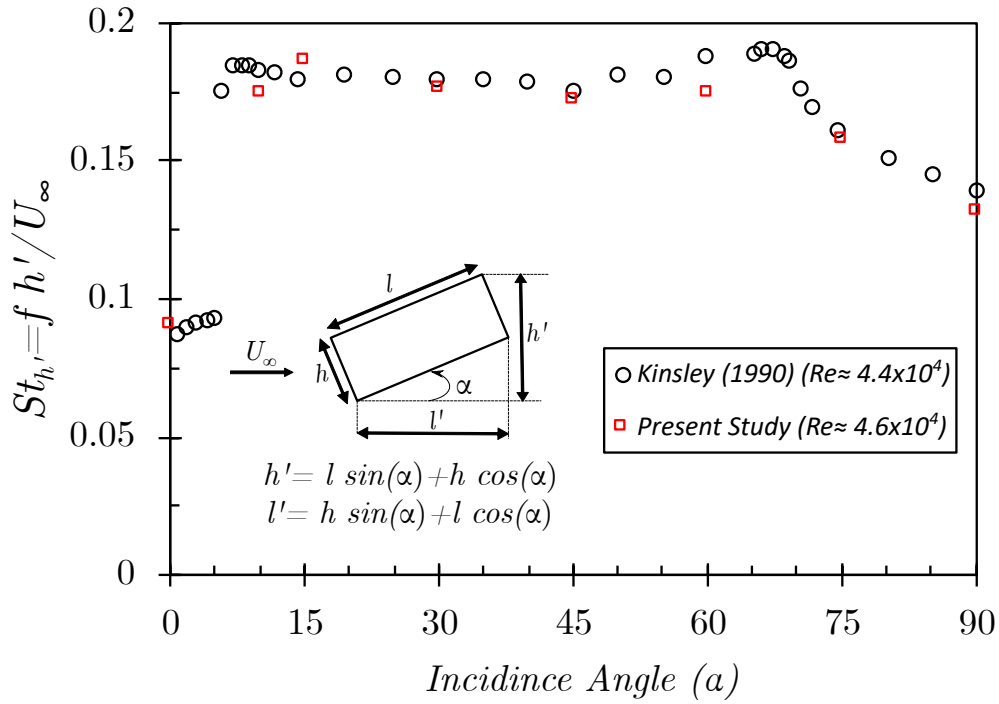

Figure 4.4: Strouhal number of natural shedding measured under non-resonant conditions at different angles of incidence.

steady flow characteristics. This will provide a baseline comprehension of the flow topology when we discuss the flow-induced acoustic resonance later in section 4.3.2

Figure 4.5 depicts the contours of time-averaged normalized streamwise velocity ($\overline{u}/U_\infty$) in the x-y plane at a flow velocity of $U_\infty = 19.32\,\mathrm{m/s}$. This specific flow velocity is chosen because it ensures non-resonant conditions for all the tested incidence angles. Streamlines are superimposed on the contours to provide further visualization of the flow patterns. The red contour line represents the recirculation zone's boundary, defined by $\overline{u}/U_\infty = 0$. The length of the vortex formation region is determined as the distance from the origin to the end of the recirculation region along the x-axis ([59]).

The diagram depicted in Figure 4.5(a) (representative of a zero angle of incidence) conspicuously presents a considerably large primary and secondary recirculation region, both demonstrating an extended vortex formation length relative to the remain-

ing cases. The primary recirculation region is delineated as the zone situated on the lateral faces of the cylinder, while the secondary recirculation region is designated as the zone immediately downstream in the wake of the cylinder. These dual regions manifest due to the compelled separation of the flow instigated by the leading sharp edge of the structure. This structural aspect leads to a pronounced curvature of the streamlines within both regions, consequently generating an extreme pressure gradient on the upper and lower surfaces of the cylinder. This gradient subsequently amplifies the hydrodynamic loading exerted upon the cylinder [131]. In Figure 4.5(b) ($\alpha = 5°$), the absence of a recirculation bubble on the windward lateral face is noticeable. However, there is still a decrease in the velocity near that surface, indicating a velocity deficit. Moreover, the contour line representing $\overline{u}/U_\infty = 0$ intersects precisely at the leeward upper edge. This suggests that the flow reattachment occurs on the windward face, while flow separation takes place at the leeward upper edge. This observation aligns with Figure 4.10(b), where no dominant peaks are observed outside of the acoustic resonance. Such observation suggests that the flow reattachment disrupts the traditional vortex shedding mechanism as a consequence of the mutual induction between the counteracting shear layers from the lower and upper sides of the cylinder. This occurrence parallels the effect observed when a splitter plate is introduced into the wake, acting to isolate the interacting shear layers from the lateral faces of the cylinder. For Figure 4.5(c) ($\alpha = 10°$), figure 4.5(d) ($\alpha = 15°$), and figure 4.5(e) ($\alpha = 30°$), the velocity contour shows no velocity deficiency on the windward lateral face which means that the flow is fully attached. Also, the recirculation region contour line intersects the leeward face of the cylinder slightly below the leeward upper edge which emphasizes on the fact that there are TE (trailing edge) vortices that shed from this edge. The elliptical stagnation points are no longer on the same cross-stream line which in turn alters the recirculation bubble streamwise elliptical

topology and creates the asymmetric wake shape. This is a result of the asymmetry of the body. It is important to note that the elliptical stagnation point is defined as a point in the flow that resembles a local minimum or maximum of the stream function. Upon comparison, Figure 4.5(a) ($\alpha = 0°$) and figure 4.5(g) ($\alpha = 90°$) share a striking resemblance, both embodying symmetric geometries. At first glance, one might be led to believe that the recirculation regions for both configurations extend the same length and exhibit identical downstream lengths. However, for the case where $\alpha = 0°$, the primary recirculation is conspicuously absent. Furthermore, the recirculation bubble topology for the case of $\alpha = 90°$ exhibits significantly less elliptical characteristics compared to the recirculation bubbles observed for the $\alpha = 0°$ scenario.

Figure 4.6 represents the normalized component $\overline{v'v'}$ of the Reynolds stresses. Such quantity resembles the variance of the vertical velocity fluctuations. It measures the intensity of the turbulent fluctuations in the vertical direction of the flow. It is important to note that the prime denotes a fluctuating quantity. It further helps to illustrate the vertical intensity and structure of the turbulence, which can be crucial in understanding how the wake behaves as the angle of incidince is varied. The boundary of the recirculation bubble is superimposed, accompanied by a prominent red dot. This dot denotes the position of the maximum $\overline{v'v'}/U_\infty^2$, with its value explicitly stated. Upon looking at all of the cases, the apex of $\overline{v'v'}/U_\infty^2$ consistently aligns with the wake's centreline. This line embodies the equilibrium induction boundary. The detachment of large-scale vortices, bearing the greatest vorticity content and hence substantial velocity fluctuations, occurs when the large-scale vortex core coincides with this line. As the shear layer undergoes alternation across this line, it endures the most pronounced transverse fluctuations, hence, an increase in the intensity of the fluctuating kinetic energy. For incidence angles $\alpha = 0°$ and $\alpha = 5°$, the apex of

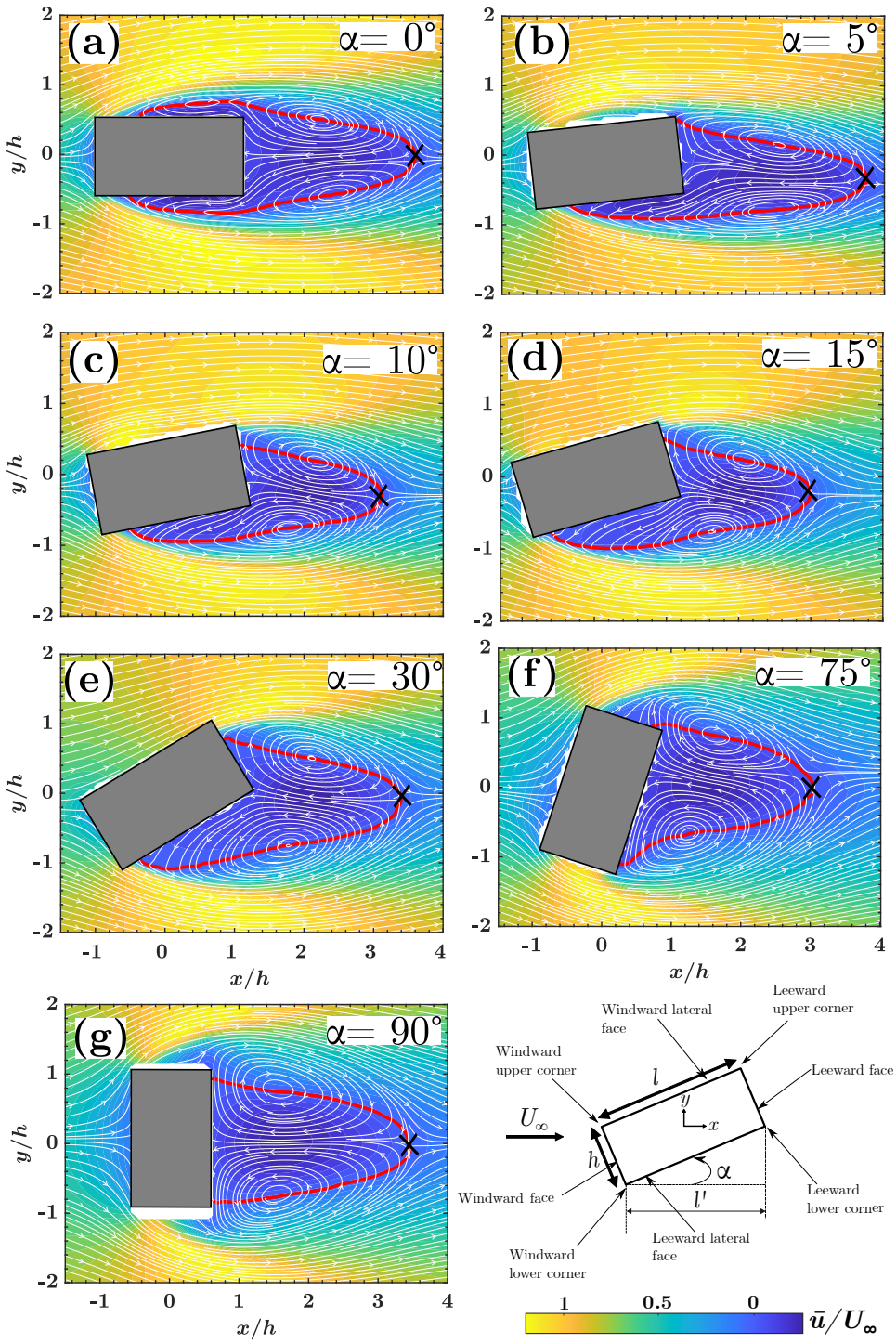

Figure 4.5: Time-averaged normalized streamwise velocity ($\bar{u}/U_\infty$) contours with streamlines superimposed in the x–y plane at $U_\infty = 19.32m/s$. The red contour line represents $\bar{u}/U_\infty = 0$, which outlines the recirculation region. The streamlines are represented by contour lines. The 'X' outlines the end of the recirculation region

$\overline{v'v'}/U_\infty^2$ is not in coincidence with the recirculation bubble boundary. This means that there is a spatial separation between the region of the highest turbulence intensity and the flow reattachment point. This might be attributed to the long streamwise length of the cylinder. Increasing the incidence angle, the apex of $\overline{v'v'}/U_\infty^2$ starts coinciding with the recirculation bubble boundary, and its value sore significantly. This means that as the cylinder bluffness increases (AR decreases) there is more synchrony between the region of most intense turbulence and the flow reattachment point which induce strong cross-stream turbulence, suggesting large-scale mixing in the wake and potentially contributing to the wake widening. Such finding correlates with the less elliptical recirculation bubble topology at high angles of incidence shown in Figure 4.5.

Phase-averaged flow topology

After studying the time-averaged flow characteristics, now, it becomes constructive to explore the shedding topology in greater detail through the construction of a phase-averaged flow field. This approach furnishes us with a profound understanding of the shear layer behavior, particularly in relation to the flow separation, impingement, and the formation of large-scale vortical structures. To unravel the unsteady flow characteristics in the near wake, a proper orthogonal decomposition (POD) analysis POD4 is implemented at the same flow velocity at which the time-averaged analysis is performed ($U_\infty = 19.32\,\mathrm{m/s}$). This method leverages progressive snapshots of the flow field, gathered using the Particle Image Velocimetry (PIV) system. For each case, a total of 1200 snapshots are captured to construct the POD modes. The overarching objective here is threefold: (i) to quantify the energy associated with each mode, (ii) to chronicle the temporal evolution of the wake flow structures, and (iii) to map out the spatial characteristics of the flow. To fulfill this objective, the POD

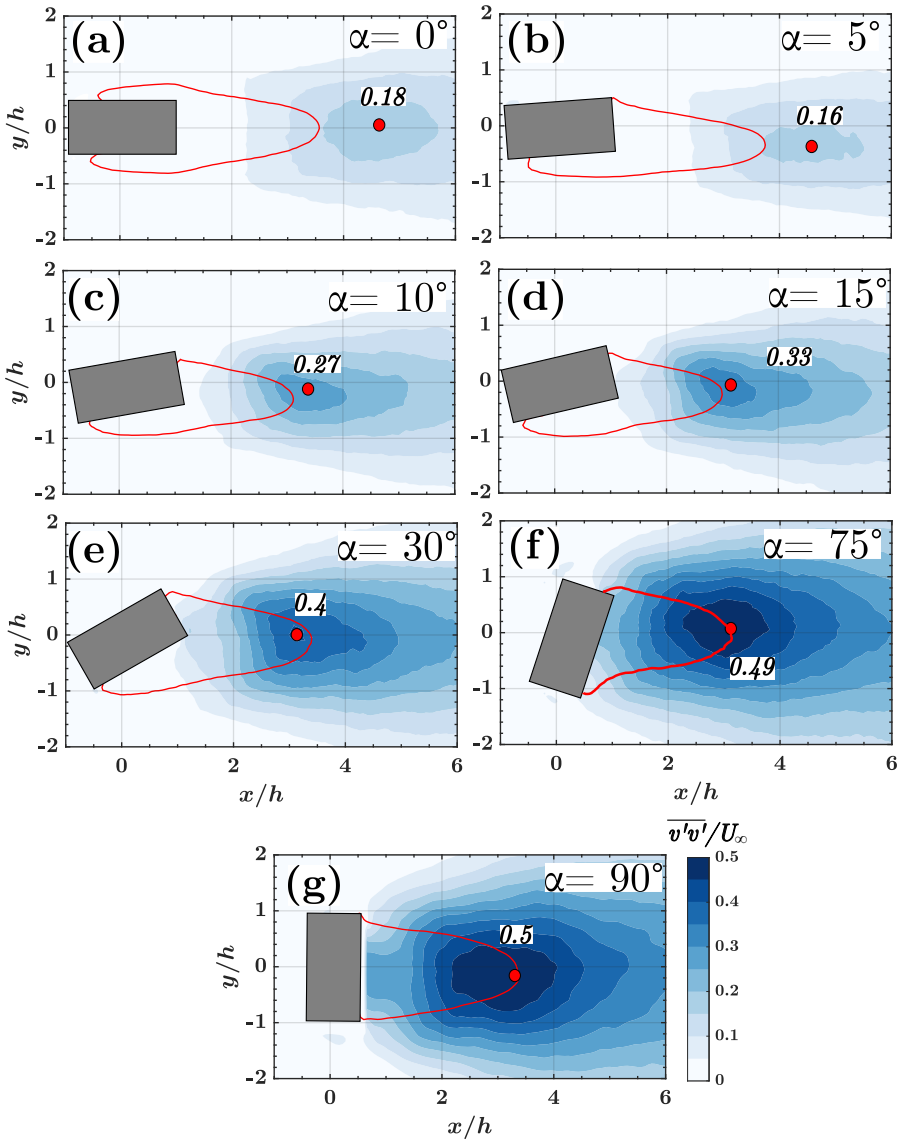

Figure 4.6: Time-averaged transverse Reynolds stress ($\overline{v'v'}/U_\infty^2$) at different angle of incidence α.

modes are extracted denoted by $\psi_k(x)$, eigenvalues (λ_k), and temporal coefficients (a_k), as outlined in previous studies ([138], [125]). The mode number (k) serves as a representation of each mode's contribution to the turbulent kinetic energy within the wake ([134], [95]). In the context of bluff body wakes, the dominant pair of POD modes encapsulates the majority of the inherent turbulent kinetic energy resulting from the high vorticity content of the large-scale vortices shed in the wake ([50], [134]).

The POD method is implemented as proposed by van Oudheusden et al. (2005b) [134] to procure phase-averaged data. Fortuitously, the bulk of the turbulent kinetic energy (TKE) is consolidated within the first pair of POD modes as evident from Figure 4.7(a). As a result, a low-order model can be enacted to derive the periodic phase-averaged component of the flow. This is achieved by combining the mean flow with the leading pair of the POD modes to reconstruct the flow field (U_{rec}). Therefore, the equation is as follows:

$$U_{rec}(x,\phi) = \overline{U}(x) + a_1(\phi)\psi_1(x) + a_2(\phi)\psi_2(x), \tag{4.3}$$

Where $\overline{U}(x)$ is the mean flow field averaged over ϕ. The notation $n = 1, 2$ is indicative of the leading pair of POD modes employed in the analysis, as further delineated. Figure 4.7(b) presents a scatter plot of the temporal coefficients (a_1 and a_2), derived from the snapshot POD post-analysis data for the angle of incidence $\alpha = 0^\circ$ case. This data scatter to form an ellipse, conforming to the following equation:

$$\frac{\overline{a_1(\phi)}^2}{2\lambda_1} + \frac{\overline{a_2(\phi)}^2}{2\lambda_2} = 1, \tag{4.4}$$

Where $\overline{a_j(\phi)}$ is the mean value of the time coefficient a_j in phase ϕ, shown as a red circle in Figure 4.7(b). The terms λ_1 and λ_2 correspond to the eigenvalues of the leading pair of POD modes. To ascertain the phases of the instantaneous flow field,

the subsequent equation is employed:

$$\phi(t) = \tan^{-1}\left[\frac{\sqrt{\lambda_2}a_1(t)}{\sqrt{\lambda_1}a_2(t)}\right] \tag{4.5}$$

The entirety of the instantaneous flow field data is classified into several bins, with the quantity determined by Eq.(4.5). To encapsulate the evolution of the shear layer and its subsequent roll into the wake, the instantaneous flow fields are parsed into 16 bins. Consequently, there is a phase difference of 22.5° degrees between every pair of successive phases.

As depicted in Figure 4.7(a), the principal pair of modes accounts for a range of 38% to 56% of the total turbulent kinetic energy. Notably, for the incidence angles $\alpha = 0°$ and $\alpha = 5°$, the total energy within the first pair is significantly lower compared to the other angles of incidence. Of these, $\alpha = 5°$ specifically demonstrates the least energy encapsulated within the first pair of modes. This finding corroborates the data in Figure 4.10(b), which lacks a prominent peak outside of resonance excitation. As the incidence angle increases, there is a corresponding increase in the energy contained within the first pair of modes. This implies that the shedding process at the initial two incidence angles might be subject to perturbations from turbulence, flow reattachment, or flow instabilities. However, beyond these angles, the shedding pattern exhibits enhanced coherence, with reduced random turbulence and fewer formations of small-scale vortical structures. These observations are consistent with the data presented in Figure 4.6, which shows an increase in transverse Reynolds stress as the incidence angle increases.

Presented in Figure 4.8 is the phase-averaged vorticity field with the streamlines superimposed, which is constructed employing the first pair of POD modes. These particular modes epitomize the fluctuations that are associated with the dominant

shedding pattern within the wake. There exists a phase difference of 180° between the columns on the left and right, this exact phase shift is selected due to its vivid illustration of the shear layer alternation and flapping behavior. A point of hyperbolic stagnation, indicated by a red dot, is introduced to the diagram. This point, which represents a saddle in the stream function $\nabla^2\psi = -\omega_z$, can be visually discerned from the distribution of the wake streamlines. Owing to its inherent instability and the consequent flow divergence, the hyperbolic stagnation point serves as a valuable tool for pinpointing the instant of large-scale vortex separation from the shear layer. For Figure 4.8(a) and (b) ($\alpha = 0$), the flow separates from the leading edges (windward edges) with no evidence of flow reattachment or impingement to the lateral faces of the cylinder. The shear layer rolls into the wake forming large-scale vortices by mutual induction between the flapping shear layers which manifest a pure leading edge vortex shedding (LEVS) mode. Moving to $\alpha = 5°$ the shear layer separated from the windward upper edge mainly rolls into the wake but there is a partial shear layer reattachment to the windward lateral face evident from the shear layer evolution from the leading edge and streamlines paths. However, the shear layer separated from the windward lower edge has no interaction with the cylinder, and the vortex detaches further downstream. Starting from $\alpha = 10°$ up until $\alpha = 30°$ the upper shear layer is completely attached to the windward lateral face and the vortices shed from the trailing edge while the lower shear layer separates from the windward lower edge and sheds into the wake. It is clear that the leeward lower edge plays a role in shaping the lower shear layer vortex. The shedding pattern can be identified as hybrid LEVS/TEVS mode for these cases. The predominance of the same shedding mode and shear layer behavior for these cases can be attributed to the range of these angles. This angle range is above the threshold for flow reattachment, approximately 5° ([57]), but remains below the symmetric wedge angle of incidence. This positioning

between these two crucial angles explains why these cases nearly manifest the same behavior. Moving to Figure 4.9, at $\alpha = 75°$, the lower shear layer separates from the windward upper edge and impinges on the trailing edge. This is evident from the streamlines distribution at the windward face and the vortex formation region at the windward lower edge at $\phi = 180°$. The upper shear layer separates at the leeward upper edge with no evidence of flow reattachment. The vortex cores are significantly larger compared to the previous cases. This is attributed to the fact that this angle of incidence is beyond the symmetric wedge angle of incidence. Beyond, this angle, the lower shear layer reattaches to the windward face near the TE, and the windward lateral face acts as an impinging surface rather than having the flow fully attached to it. So, the shedding mode can be designated as LEVS/ILEVS mode from the upper and lower shear layers respectively. At an angle of incidence of $\alpha = 90°$, a spatio-temporal symmetry manifests owing to the inherent symmetry of the cylinder resulting in LEVS mode, similar to the case at $\alpha = 0°$. However, the vortex cores appear notably larger and less elliptical in shape. This occurrence can be attributed to two primary reasons. Firstly, a reduced streamwise dimension amplifies the momentum of the shear layer as it rolls into the wake, fostering the formation of a vortex with enhanced vorticity content. Secondly, the expanded cross-stream dimension allows for a more substantial gap between the separation edge and the wake centerline, providing a wider spatial range for the vortex to form.

4.3.2 Flow under resonant condition

Flow-sound interaction response

This section focuses on the aeroacoustic response of the rectangular cylinder at various angles of incidence. The objective is to understand as well as gain insights into the

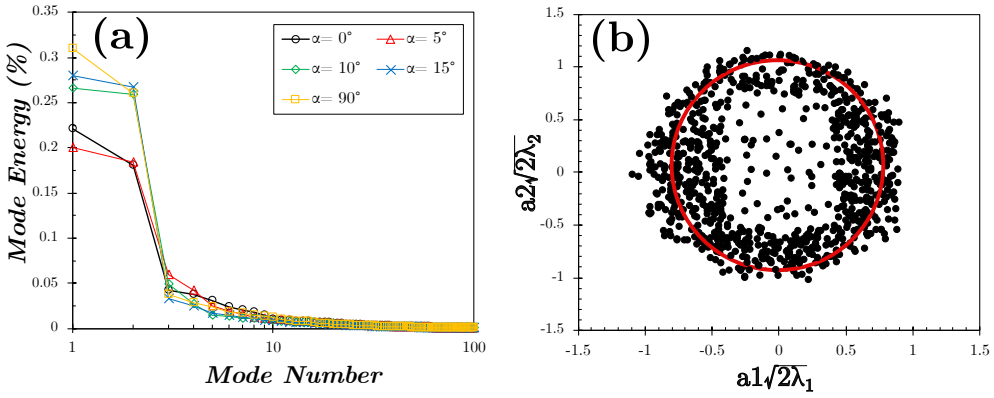

Figure 4.7: Energy distribution of the POD modes in the turbulent kinetic energy: (a) mode energy (λ_k), and (b) Scatter plot of the temporal coefficients a_1 and a_2 from the POD analysis performed on the PIV data for the angle of incidence $\alpha = 90°$. The definition of the red circle is given by Eq.(4.4).

self-selection of different shedding modes in response to acoustic transverse modes.

This will help us understand the mechanisms underlying the shedding process and how they are influenced by the angle of the cylinder. Furthermore, the aeroacoustic response identified the flow velocities at which the phase-locked PIV measurements are performed. This enables a thorough examination of the shedding pattern changes and provides valuable information about the correlation between the flow and acoustic fields.

Figure 4.10 delineates the normalized acoustic pressure plotted on the y-axis. The secondary x-axis represents the peak frequency detected in the Fast Fourier Transform (FFT) of the acoustic pressure signal. The green shade resembles a region at which self-excited acoustic resonance is observed. The acoustic pressure is a result of the velocity perturbations caused by the shedding process. Therefore, the peak frequency detected in the FFT corresponds to the dominant shedding pattern frequency, which generates pressure perturbations and produces acoustic sound. To extract the root mean square value of the acoustic pressure, a narrow band-pass filter is applied to the pressure signal, specifically around the peak frequency. This filtering step helps

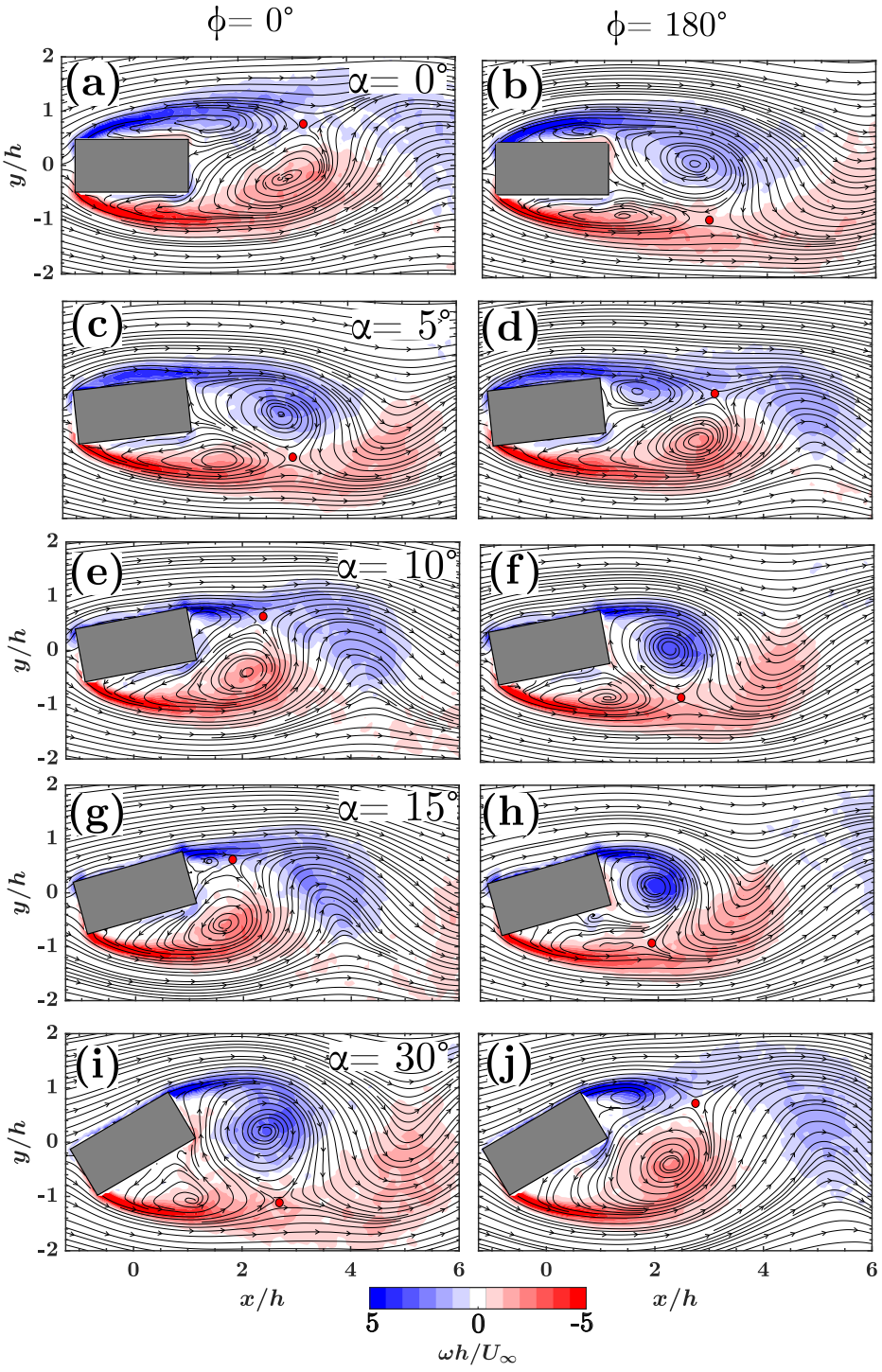

Figure 4.8: Phase-averaged vorticity field with the streamlines superimposed at $U_\infty = 19.32\ m/s$ for all the tested incidence angles

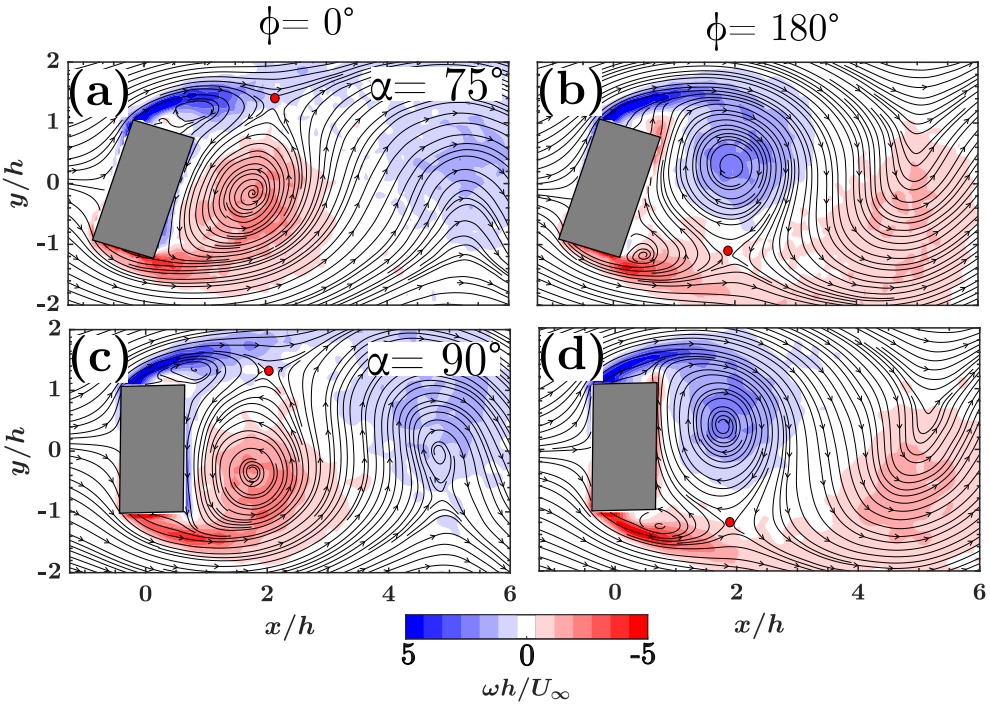

Figure 4.9: Phase-averaged vorticity field with the streamlines superimposed at $U_\infty = 19.32\ m/s$ for all the tested incidence angles (Continued)

eliminate any noise contamination.

Figure 4.10(a) illustrates the shedding progression of the rectangular cylinder at zero angle of incidence up to a flow velocity of $U_\infty = 73.41$ m/s. Up to this velocity, the shedding frequency gradually increases in a consistent manner. However, at this specific flow velocity, a sudden frequency jump occurs, accompanied by a rapid increase in the normalized acoustic pressure. The shedding frequency experiences a significant jump, increasing approximately fourfold from $f_s = 469$ Hz to $f_s = 1931$ Hz, which is close to the frequency of the third acoustic transverse mode of the duct. The observed frequency is slightly lower than the theoretical acoustic mode frequency which is attributed to the added mass effect, as discussed in previous studies ([71], [73], [111]). This clear frequency lock-in suggests the occurrence of self-excited acoustic resonance. Parker & Welsh (1979) [140] observed a similar phenomenon with a rectangular cylinder possessing an aspect ratio (AR) of 5. In-

triguingly, they reported a sudden stimulation of the duct's primary transverse mode, with the frequency abruptly doubling. This event was ascribed to what they termed "excited" vortex shedding. Nevertheless, a definitive source of this excitation was not substantiated, as the study lacked the implementation of modern flow visualization techniques. Nakamura et al. (1991) [79] later stated that this is attributed to 'ILEV' being excited. They stated two main reasons for his speculation, firstly, this is an intrinsic masked characteristic of coherent flow structures in turbulent flows ([128]) which can be excited by an externally tuned source. Secondly, the frequency at which the jump took place matches the natural ILEVS frequency. The Strouhal number which matches the jump in our case is $St_{l'} = 0.6$ which is exactly equal to the first mode of the ILEV for elongated rectangular rods with AR ranging from 3 to 5 reported in the literature ([84], [77], [91], [68]). This scenario prompts a crucial question: Is the detected frequency jump indicative of another stable natural vortex shedding mode, or does it signify shear layer instability? To resolve whether this constitutes an inherent ILEV or is reflective of a natural vortex-shedding mode, flow-sound phase-locked PIV measurements of the flow field will be discussed in the forthcoming sections.

Looking at Figure 4.10(b) which shows the aeroacoustic response at $\alpha = 5^\circ$ one can notice that there are only data points during resonance excitation and no data points outside acoustic resonance excitation. This is because outside of acoustic resonance, no distinct peaks are observed in the spectra of the acoustic pressure signals. Rockwell (1977b) [101] reported that there are no distinct peaks in the velocity fluctuations spectrum for a square cylinder at an angle of incidence $\alpha = 14^\circ$ which means that there is no detectable contribution to the vortex shedding process. However, for higher α values the distinct peaks reappear again. He stated that this is a result of the flow reattachment. Since the rectangular cylinder employed in our study has

$AR = 2$, this phenomenon occurs at a substantially lower α. Even though this case shows no dominant peaks in the acoustic pressure spectra, the POD analysis can identify organized turbulent fluctuations that form this shedding mode. However, the flow reattachment destabilizes the mode and that is why this case showed the least turbulent energy in the first two modes as shown in Figure 4.7. Multiple acoustic modes are excited all coinciding with two main Strouhal lines, corresponding to $St_{l'} = 0.6$ and $St_{l'} = 1.21$, respectively. It is intriguing to observe that the transitions between the different shedding modes occur instantaneously without any lock-out periods. The switch between the first and third modes, as well as the fifth and third modes, happens abruptly. During acoustic resonance excitation, the vortices exhibit spanwise correlation ([93], [121]), and the vortex shedding process is significantly enhanced, masking any minor or masked instabilities. This enhancement is evident from the acoustic pressure spectra, which exhibits a sharp peak with a high-quality factor. However, it is important to note that higher mode flow instabilities are still able to synchronize with higher acoustic transverse modes. This implies that even during self-excited acoustic resonance, other shedding modes or instabilities are inherently present and can engage in continuous energy exchange with the nearest acoustic resonant mode. When comparing these values to the prior case of $\alpha = 0°$, the Strouhal line with the lesser slope coincides with the steeper line for the $\alpha = 0°$ case, both aligning with the ILEV periodicity for aspect ratios (AR) within the range of 3 to 5 as indicated in the existing literature. Intriguingly, the steeper Strouhal line for $\alpha = 5°$ aligns with the values for the second mode ($n = 2$) of the ILEV periodicity, which was previously observed exclusively for AR values ranging from 6 to 9. This observation necessitates further exploration and flow visualization which we will delve into in a subsequent section.

Figure 4.10(c) corresponds to an incidence angle of $\alpha = 10°$ and displays a similar

behavior, with two shedding modes where one dominates and matches the natural vortex shedding Strouhal number, while the higher Strouhal periodicity emerges only when it coincides with an acoustic duct mode frequency. From an incidence angle of $\alpha = 15°$ onwards, the higher Strouhal periodicity appears to diminish, leaving only the dominance of natural vortex shedding with a characteristic resemblance to the first acoustic mode at the coinciding frequency. The trend of the maximum normalized acoustic pressure demonstrates an increasing pattern, except for a drop observed at $\alpha = 75°$. This suggests a significant change in the vortex formation and the wake dynamics at this particular angle, which will be further discussed later in the chapter. The flow-sound interaction response provides clear evidence that for incidence angles $\alpha < 15°$, the dominant shedding mode outside of acoustic resonance excitation is the natural vortex shedding. However, there exists an instability or higher-order shedding mode that couples with the third and fifth acoustic transverse modes. The insights gleaned from these findings encourage us to visualize the flow dynamics under specific resonant conditions, thereby aiming to gain a more profound comprehension of the self-selection mechanism that governs the different shedding modes. By scrutinizing the flow behavior under resonant conditions, we can elucidate the complex processes that provoke the excitation of these distinctive shedding modes. Ultimately, a better understating of the underlying mechanisms driving the observed phenomena can be established.

Flow-sound phase-locked flow topology

To address the pivotal question posited in the previous section, a detailed investigation of the vorticity field during self-excited acoustic resonance is carried out. The acoustic pressure signal is used to trigger the laser to visualize the flow over one complete acoustic pressure cycle dividing it into 8 consecutive phases. In order to identify

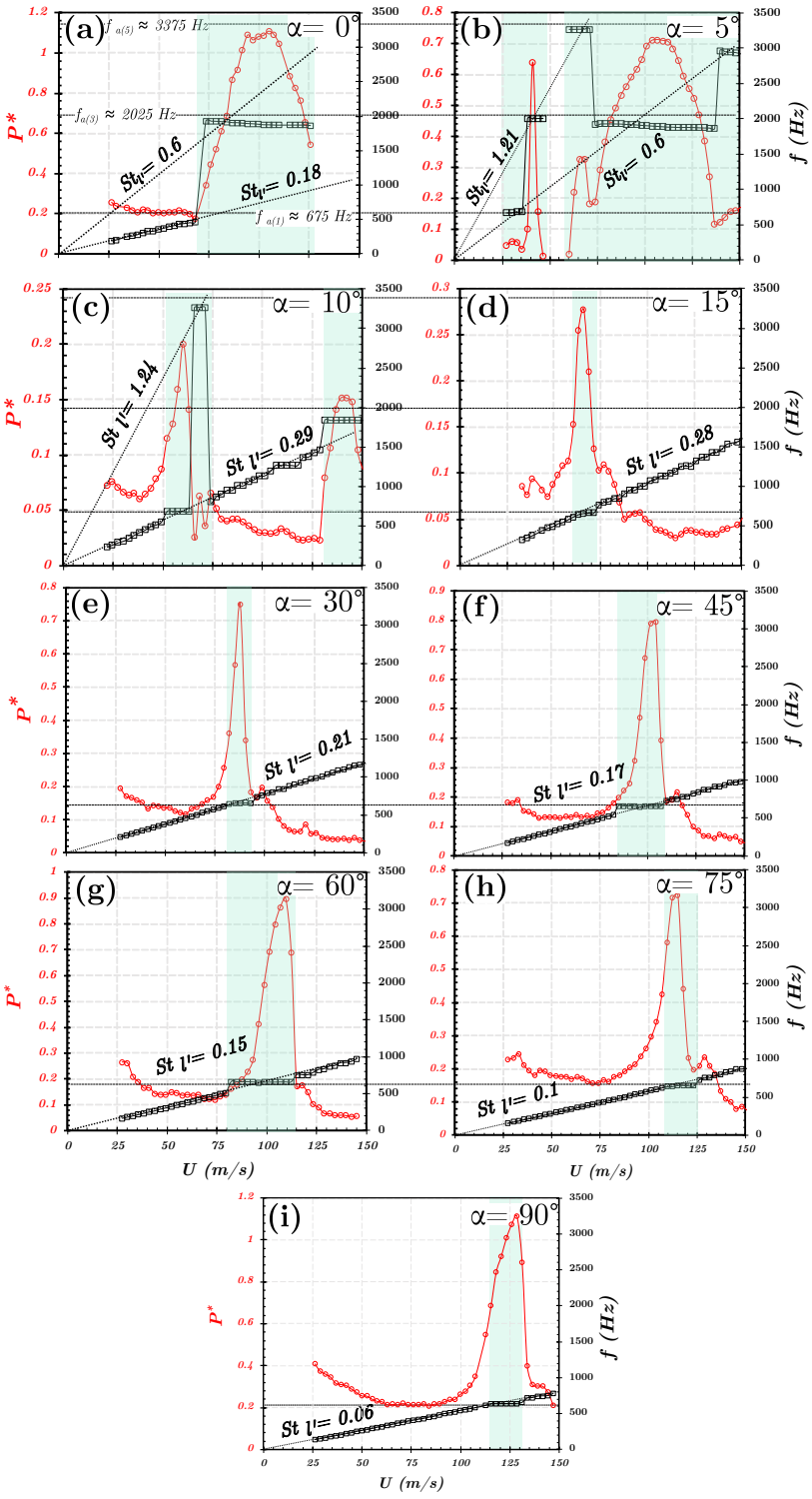

Figure 4.10: Aeroacoustic response of a rectangular cylinder with aspect ratio $AR = 2$ at different angle of incidence α

discrete vortices, the Q-criterion is utilized to outline the circulation in the high vorticity regions which correspond to a separate vortex. The Q-criterion derived from the velocity gradient tensor identifies the regions where the vorticity is higher than the strain with a specific value which is set to $Q > 0.005$ in our case. Such value allows robust identification of large-scale vortices with significant recirculation. Figure 4.11 depicts a Phase-locked vorticity field with the streamlines superimposed over a complete acoustic pressure cycle during the third mode excitation (f_{a3}) for $\alpha = 0°$ with the Q-criterion as a black marker. The Strouhal number which matches this case is $St_{l'} = 0.6$ as shown previously in Figure 4.10. It is clear at the first glance that the shedding pattern is completely different from the shedding pattern observed outside of resonant condition (Figure 4.8(a)). At $\phi = 0°$, which corresponds to the zero phase of the acoustic pressure cycle, there is one clear LE vortex within the upper and lower shear layer both separated by a phase shift and convecting downstream. At the same instant, there is a TE vortex already formed and partially rolled on the leeward face toward the wake centerline. At $\phi = 45°$ the LE vortex from the upper shear layer impinged on the trailing edge combining with the TE vortex which was already formed from the previous phase. At $\phi = 90°$, the combined vortex detached and shed in the wake forming a hyperbolic saddle point. At $\phi = 135°$ a TE vortex is already forming and the vortex shed in the wake from the upper shear layer has a completely different topology with enhanced vorticity content and more circular topology. This is attributed to the flow-sound interaction occurring under resonant conditions, during which there is an exchange of energy leading to heightened acoustic pressure levels and an enhancement of flow correlation. The resonance conditions effectively serve as a platform for energy transfer, thereby amplifying the acoustic pressure levels and enhancing the flow correlation. At $\phi = 180°$, the LE vortex is formed within the upper shear layer and the TE vortex significantly grew from the last phase. Afterward, the

symmetric alternation takes place until the acoustic pressure cycle is complete.

Now, let us focus on the formation phase of the LE and TE vortices within the lower shear layer, which rotates in an anticlockwise direction. The TE vortex takes shape between $\phi = 90°$ and $\phi = 135°$. Assuming it forms equidistant between these two phases, the formation phase of the TE vortex can be approximated to be at $\phi \approx 112.5°$. Regarding the LE vortex, it materializes between $\phi = 315°$ and $\phi = 0°$. Adopting the same assumption, the LE vortex formation phase approximates to $\phi \approx 337.5°$. Consequently, a phase difference of $\phi \approx 135°$ can be observed between the LE and TE vortices. Figure 4.12 shows one complete cycle of the acoustic pressure signal discretized at an arbitrary phase from the time series. It is clear that there are two distinct peaks which are distant by $\phi_a \approx 135°$. This phase shift exactly matches the phase shift between the LE and TE vorticies calculated from the vorticity field. This is a clear evidence that this shedding pattern is an ILEV/TEVS shedding pattern with $n = 1$ which is controlled by the acoustic resonance which excites and modulates the feedback between the TE and LE within the acoustic pressure cycle. Indeed, it is modulated and masked by the natural shedding mode. Interestingly, the ILEV mode has been documented in the literature to emerge from an aspect ratio (AR) of 3, with a corresponding stepwise increase in the Strouhal number as the AR escalates. This signifies that in our case ($AR = 2$) the resonant condition imparts an added streamwise length effect on the cylinder, thereby enabling the manifestation of the instability. This is clear evidence that this shedding pattern is an ILEV/TEVS shedding pattern with $n = 1$ which is controlled by the TE vortices. This is evident from $\phi = 90°$ at which there is an LE vortex within the lower shear layer and no TE vortex formed. Moving to $\phi = 180°$ the TE vortex is formed because of the suction pressure caused by the detached vortex from the upper face at the previous phase. So, the TE vortex formation is self-sustained, and as it sheds after impingement the

pressure perturbation caused by this vortex stimulates the LE to shed a new vortex. The acoustic resonance excites and modulates the feedback between the leading and trailing edge. The reason why this mode is not detectable under non-resonant conditions is that the feedback pressure perturbation between the two edges is weak and its frequency is significantly less than the natural shedding mode frequency. Indeed, it is modulated and masked by the natural shedding mode. This suggests a coupling of the acoustic mode with the pressure feedback loop that exists between the leading and trailing edges. This coupling effectively 'locks' the system, engendering sound at its resonant frequency and subsequently modulating the global instability. As a result, this mechanism allows for the dominance of the shear layer instability. Such finding aligns with Nakamura et al. (1991) [79] comment on [121] self-excited acoustic resonance experiment and contradicts Mills et al. (2003) [67] statement that the excited pattern is a natural shedding mode.

Figure 4.13 illustrates the phase-locked vorticity field for $\alpha = 5°$ at the peak coincidence between the Strouhal line $St_{l'} = 1.21$ and the third transverse acoustic mode of the duct. Evidently, a unilateral shedding street is present, devoid of any vortex alternation in the wake. Steady separation bubbles form in the wake, similar to those observed in the time-averaged velocity contour (Figure 4.5(b)). In the upper shear layer (rotating clockwise), the shear layer experiences complete separation, with no boundary-layer fluid originating from the windward upper edge, leading to vortex formation within the shear layer. Subsequently, this vortex impinges just before the trailing edge, prompting the formation and shedding of a TE vortex into the wake, and the initiation of a new vortex at the LE. In contrast, for the lower shear layer, vortices shed at the windward lower edge and are convected downstream, with the shear layer drifting in the same direction. Over a single complete acoustic pressure cycle, two vortices are shed from both the upper and lower the windward edges.

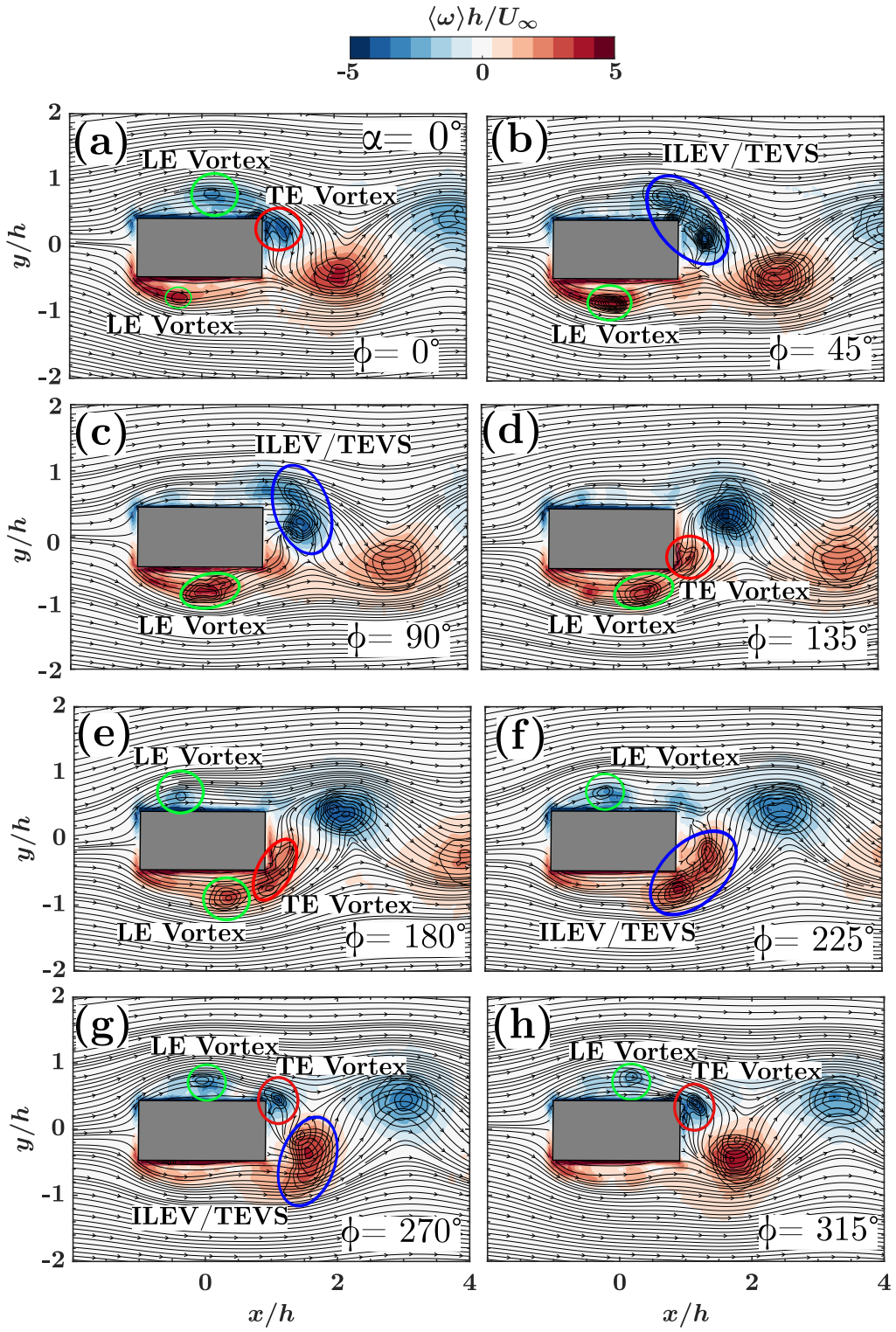

Figure 4.11: Phase-locked vorticity field with the streamlines superimposed over a complete acoustic pressure cycle during acoustic third mode excitation f_{a3} for $\alpha = 0°$ at $St_{l'} = 0.6$

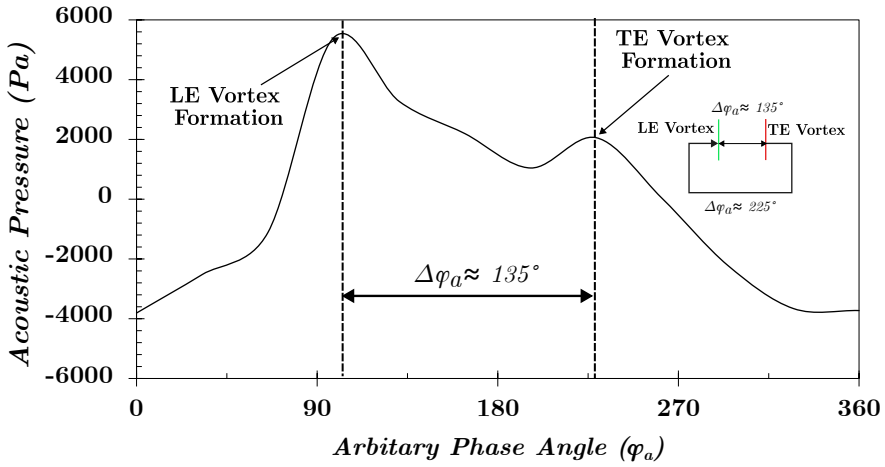

Figure 4.12: Single complete acoustic pressure cycle discretized at an arbitrary phase ϕ_a during third mode excitation f_{a3} for $\alpha = 0°$ at $St_{l'} = 0.6$

Notably, a novel hybrid mode is observed, termed ILEV/LEVS, that has not been reported in the existing literature. However, the matching Strouhal number equates to that for ILEV/TEVS at $n = 2$, which has been previously noted for elongated cylinders ($6 < AR < 9$) in the literature.

Figure 4.14 portrays a single complete acoustic pressure cycle, discretized at an arbitrary phase ϕ_a during the third acoustic mode excitation f_{a3} for $\alpha = 5°$ at $St_{l'} = 1.21$. It is clear that the signal is a pure sinusoidal wave, reinforcing the observation that the ILEV at the upper shear layer is not modulated by a feedback loop between the discrete TE and LE vortices. But rather by the impinging LE vortex on the TE with the absence of the formation of the TE vortices. Considering the sinusoidal characteristic of the acoustic pressure signal, the shedding of leading edge (LE) vortices from the lower shear layer is instigated and regulated by a global acoustic perturbation, thereby producing a spatiotemporally symmetric wake.

Analogously, Nakamura & Nakashima (1986) [77] conducted an experiment on a rectangular cylinder with $AR = 5$, both with and without a splitter plate in the wake, discovering that the instability mechanism and the shedding frequency were

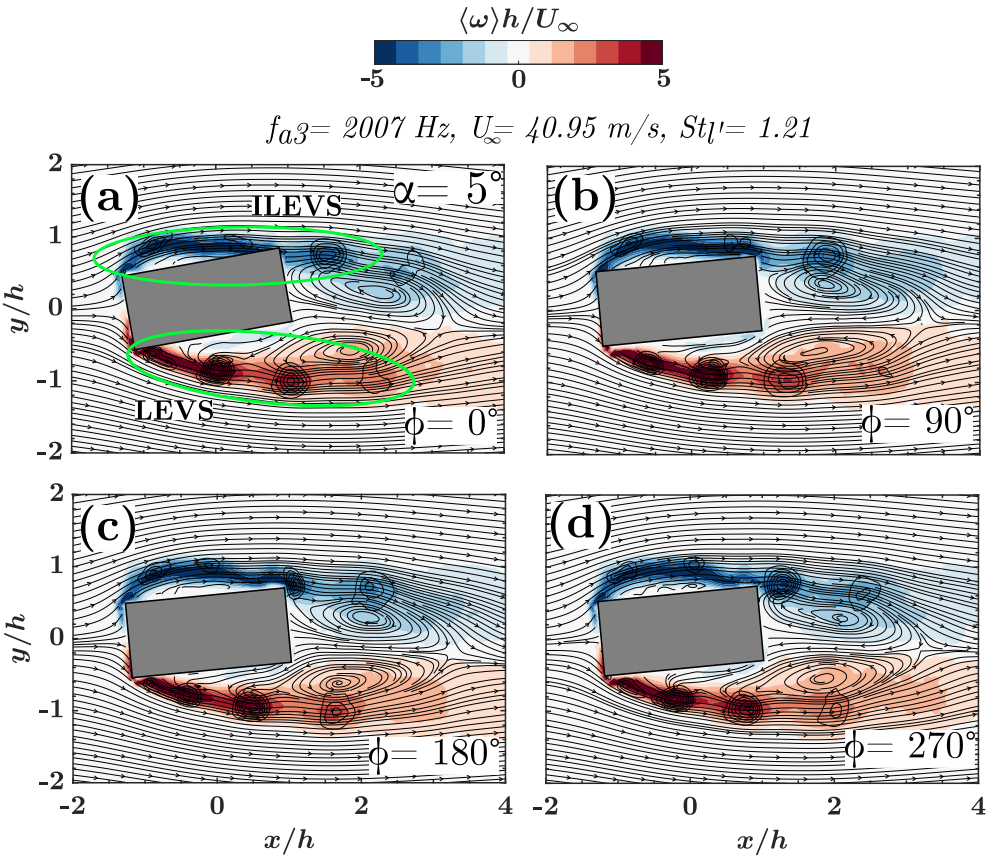

Figure 4.13: Phase-locked vorticity field with the streamlines superimposed over a complete acoustic pressure cycle during acoustic third mode excitation f_{a3} for $\alpha = 5°$ at $St_{l'} = 1.21$

not influenced by the splitter plate positioned at the TE. In this instance, the small incidence angle introduces this pseudo isolation in the wake even though the cylinder is not symmetric in the cross-stream direction. This provides compelling evidence that the instability observed here is the ILEV instability which is globally modulated by acoustic perturbation under resonant conditions.

Figure 4.15 depicts the phase-locked vorticity field at an incidence angle of $\alpha = 5°$, at the coincidence between the Strouhal line $St_{l'} = 0.6$ and the third transverse acoustic mode of the duct. This Strouhal number aligns with the excitation case for $\alpha = 0°$. Despite the similarity in the coupling with the third acoustic mode as

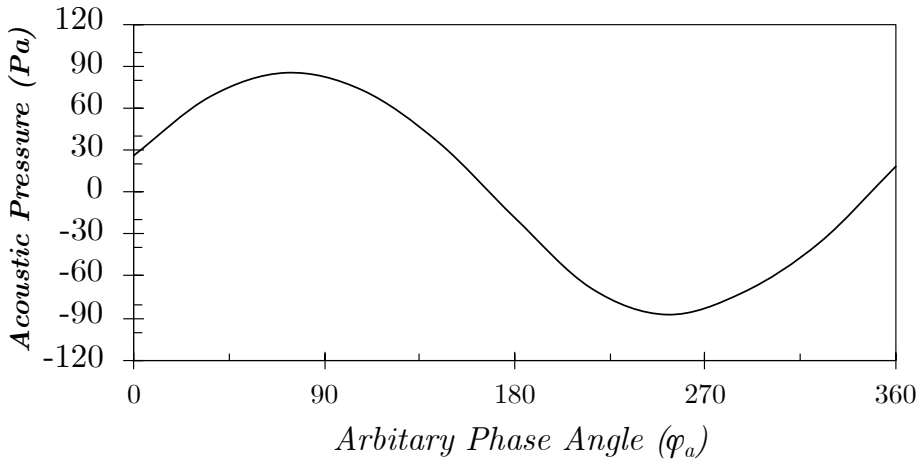

Figure 4.14: Single complete acoustic pressure cycle discretized at an arbitrary phase ϕ_a during third mode excitation f_{a3} for $\alpha = 5°$ at $St_{l'} = 1.21$

in the previous case, the characteristics of the flow and the mechanism of vortex shedding differ substantially. Evidently, the vortex-shedding mechanism of the upper and lower shear layers significantly differs. Looking at the upper shear layer, the ILEV/TEVS mechanism is present. However, the boundary-layer fluid is significantly more attached to the windward lateral face compared to the $\alpha = 0°$ case. This is due to the incidence angle, which stimulates the shear layer to attach to the windward lateral face. Furthermore, the Leading Edge (LE) vortex exhibits less vorticity content and is smaller in comparison to the $\alpha = 0°$ case. Conversely, the mechanism for the lower shear layer is primarily LEVS, characterized by a vortex forming at the windward lower edge and convecting within the shear layer. Interestingly, the vortex impinges on the leeward lower edge (trailing edge), but this interaction does not disrupt the vortex circulation. Instead, it modifies the vortex topology into a more elliptical shape. Nevertheless, the vortex regains its circular topology in the wake due to the correlation with the acoustic resonance.

Figure 4.16 shows one complete cycle of the acoustic pressure signal discretized at an arbitrary phase from the time series. A very similar cycle trend to the case of

$\alpha = 0°$ with also a phase shift between the two peaks equals $\phi_a \approx 135°$ which matches the TE and LE vorticies phasing from the phase-locked vorticity field. Interestingly, even though, the shedding mechanism is not symmetric from the upper and lower shear layer, the ILEV/TEVS still dominates the frequency response and the acoustic resonance modulates the two mechanisms from both shear layers to reproduce an organized vortex shedding street in the wake.

Therefore, in the case where $\alpha = 5°$, the interaction with the third acoustic mode occurred at two distinct flow velocities, corresponding to the coincidence of two separate Strouhal lines with the acoustic mode. Nonetheless, the mechanisms of excitation in both cases differ markedly which is evident from the flow topology and the acoustic pressure signal. These observations highlight the principle that although acoustic perturbation serves as an external stimulus, the flow self-selects and sustains its instability, contingent on favorable frequency alignments with the inherent flow instability. Comparing the flow topology for the cases of $\alpha = 0°$ and $\alpha = 5°$ during resonant conditions and before resonant conditions in Figure 4.8, the flow topology is substantially different. This emphasize on the fact that, at low incidence angle during resonant conditions, the flow self-selects an inherent flow instability which is masked by the coherent turbulent structures and the organised natural vortex shedding.

Figure 4.17 depicts the phase-locked vorticity field corresponding to an incidence angle of $\alpha = 10°$, aligning with a Strouhal number of $St_{l'} = 0.6$. This number corresponds to the lower-slope Strouhal line from Figure 4.10. Capturing the phase-locked flow field for the higher-slope line coincidence was not achievable due to the narrow lock-in range and weak excitation. The Strouhal number for this case aligns with the natural vortex shedding range, evident from the vorticity field displaying natural shedding in the wake. The upper shear layer is fully attached to the windward lateral face and sheds from the TE, while the shear layer separates entirely from the

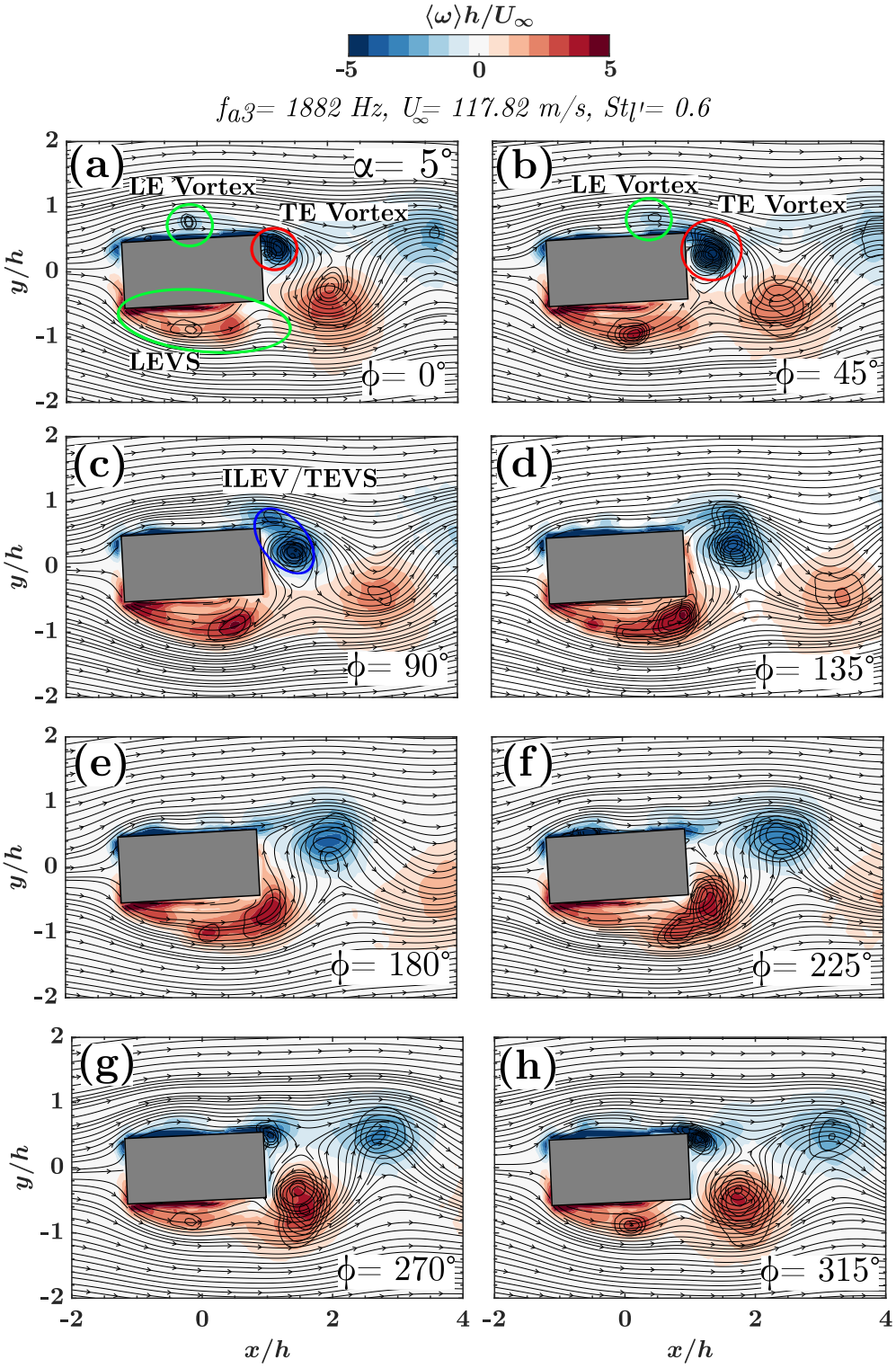

Figure 4.15: Phase-locked vorticity field with the streamlines superimposed over a complete acoustic pressure cycle during acoustic third mode excitation f_{a3} for $\alpha = 5°$ at $St_{l'} = 0.6$

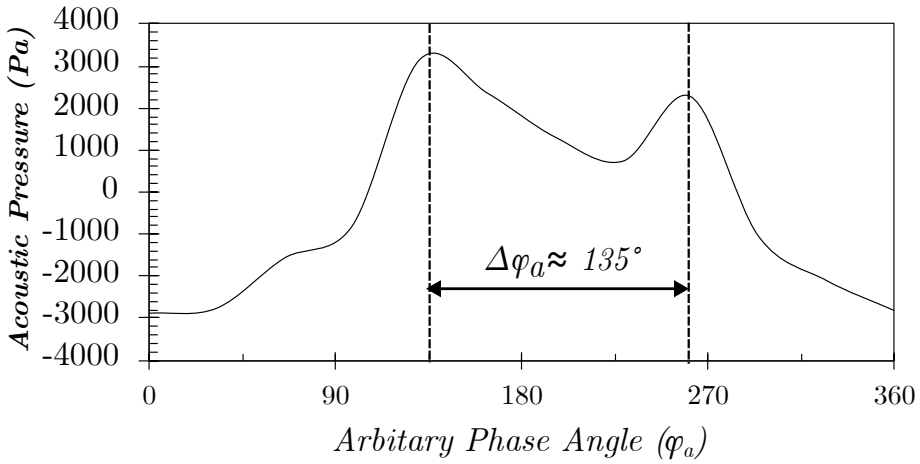

Figure 4.16: Single complete acoustic pressure cycle discretized at an arbitrary phase ϕ_a during third mode excitation f_{a3} for $\alpha = 5°$ at $St_{l'} = 0.6$

windward lower edge, forming a vortex and a recirculation zone bounded by the leeward lateral face. This shear layers interaction results in a LEVS/TEVS mode with the acoustic mode modulating the shedding frequency and locking it to the acoustic mode frequency over a range of velocities. Intriguingly, the phase difference in vortex formation between the upper and lower shear layers is virtually nil. Upon examining Figure 4.18, a pronounced and broad peak is apparent. This peak distinctly illustrates the synchronized formation of counter-rotating vortices. This synchronization is attributable to that specific incidence angle, which isolates the upper and lower shear layers. Consequently, the formation of a hyperbolic stagnation point, responsible for vortex detachment, takes place one time through the shedding cycle after the lower shear layer vortex has almost passed the cylinder. At this juncture, corresponding to $\phi = 0°$ in our case, both vortices detach, with the upper shear layer vortex leading spatially because of the difference in the size of the counter rotating vorticies.

Figure 4.19 illustrates the case where $\alpha = 15°$. Here, the shear layer is fully attached to the windward lateral face, with vortices being shed from the leeward upper edge. The shear layer extends spatially downstream, with the TE vortex forming at a

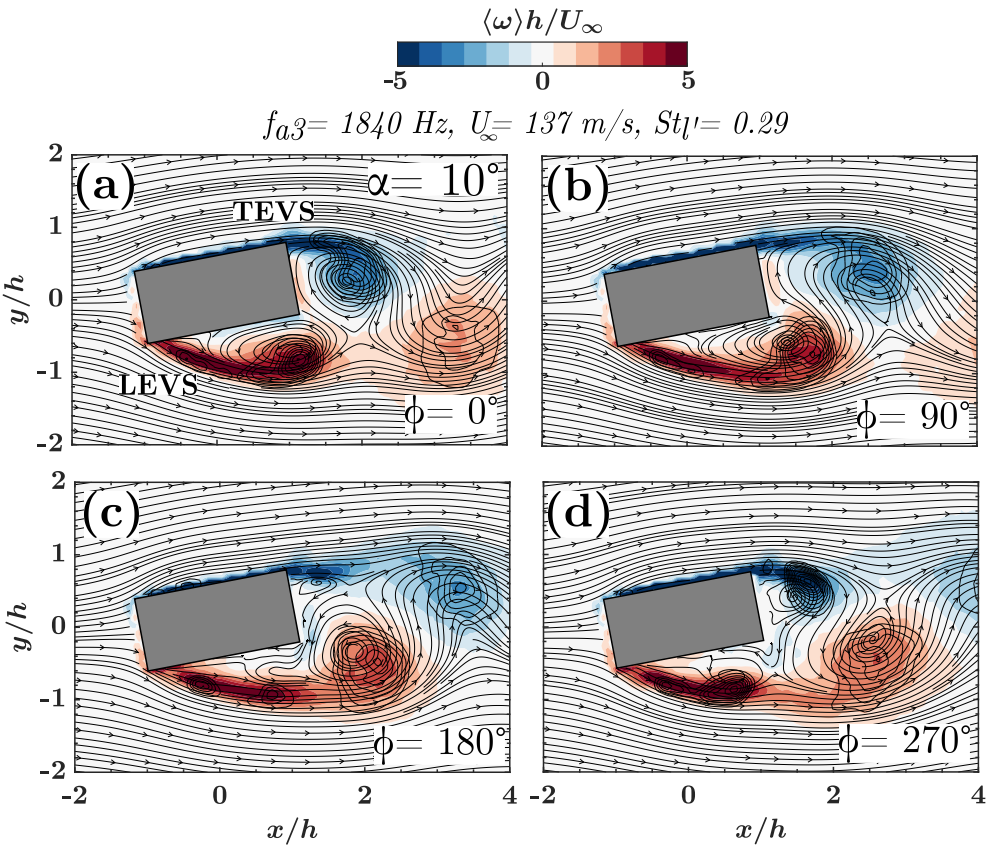

Figure 4.17: Phase-locked vorticity field with the streamlines superimposed over a complete acoustic pressure cycle during acoustic third mode excitation f_{a3} for $\alpha = 10°$ at $St_{l'} = 0.29$

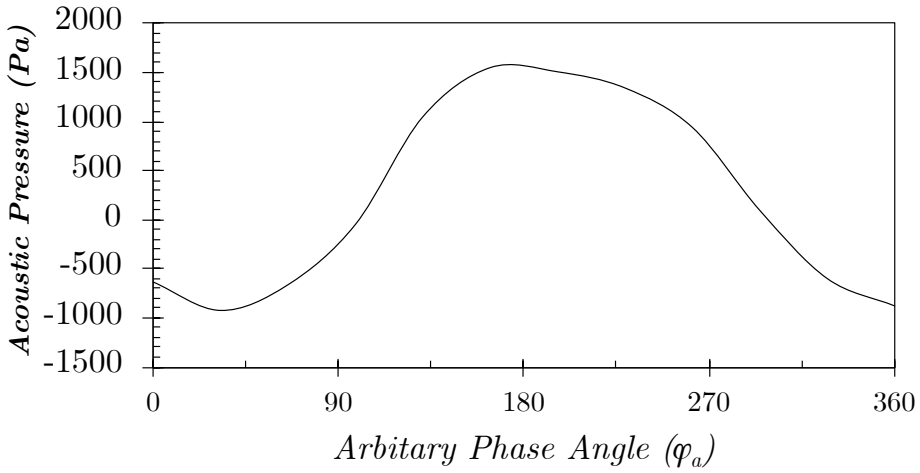

Figure 4.18: Single complete acoustic pressure cycle discretized at an arbitrary phase ϕ_a during third mode excitation f_{a3} for $\alpha = 10°$ at $St_{l'} = 0.29$

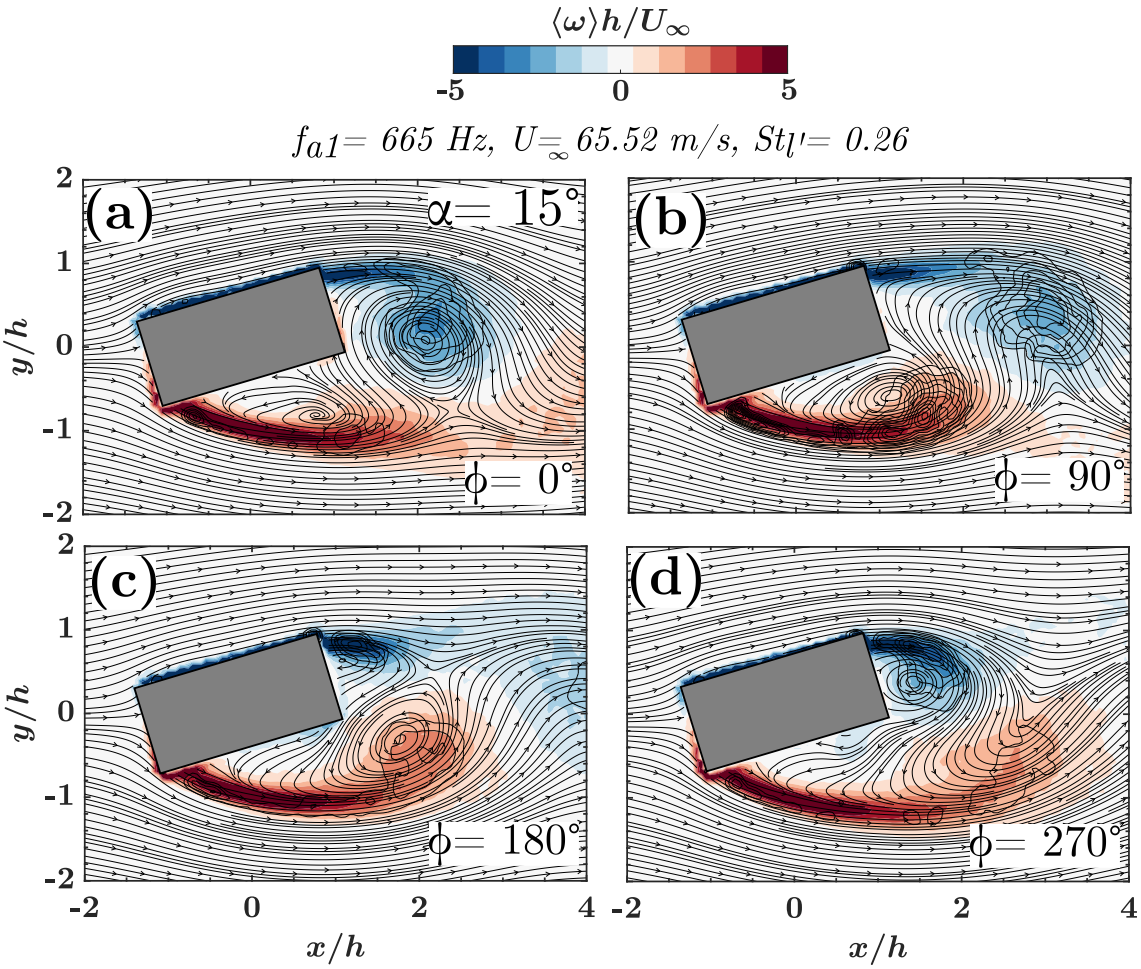

Figure 4.19: Phase-locked vorticity field with the streamlines superimposed over a complete acoustic pressure cycle during acoustic first mode excitation f_{a1} for $\alpha = 15°$ at $St_{l'} = 0.26$

certain distance from the leeward face. This configuration results from the incidence angle which, as with the previous case, segregates the upper and lower shear layers and shifts the formation of a hyperbolic stagnation point further downstream. However, in this case ($\alpha = 15°$), the vortex formation is out of phase. This is attributed to the higher incidence angle which allows for a longer vortex formation length for the lower shear layer, enabling it to interact with the forming upper shear layer vortex. This interaction induces the creation of a saddle point in an out-of-phase manner.

For the case where $\alpha = 75°$, the flow topology within the wake varies significantly

compared to the previously discussed cases of $\alpha = 10^\circ$ and $\alpha = 15^\circ$. As depicted in Figure 4.20, the flow impacts the windward lateral face for this scenario, separating fully from the windward upper edge and rolling into the wake to form a large-scale vortex. However, the flow partially separates from the windward lower edge, with the vortex forming at the leeward lower edge (trailing edge), as evident from Figure 4.20(a). Increasing the incidence angle to $\alpha = 90^\circ$, the wake becomes spatially symmetric in the cross and streamwise directions. The two shear layers experience significant flapping in the streamwise direction. The leading edge separation induces the formation of vortical structures. Due to the large suction pressure in the wake, the shear layer is diverted toward the upper and lower faces and the large-scale vortex forms at the cylinder trailing edge and starts growing until its centre passes through the wake centreline at which it detaches from the shear layer and shedding alters its direction.

The larger vortex cores are due to the larger crosswise cylinder length, which allows the shear layer to entrain more flow, inducing a higher suction pressure. Furthermore, since the incidence angle exceeds the symmetric wedge angle, there is significantly less interaction between the large-scale vortices and the leeward edges. This lack of interaction allows the growth of vortex circulation to be more pronounced.

Comparing the flow topology for the cases of $\alpha > 5^\circ$ under resonant and non-resonant conditions, the flow topology is not changed but only becomes more coherent and correlated. The absence of the shear layer instability modes is due to two main reasons. Firstly, due to the unsymmetrical geometry which does not signify any flow instability but rather prompts the natural vortex shedding mode. Secondly, the reduced streamwise length of the rod as the angle of incidence increases makes the vortex shedding mode dominant.

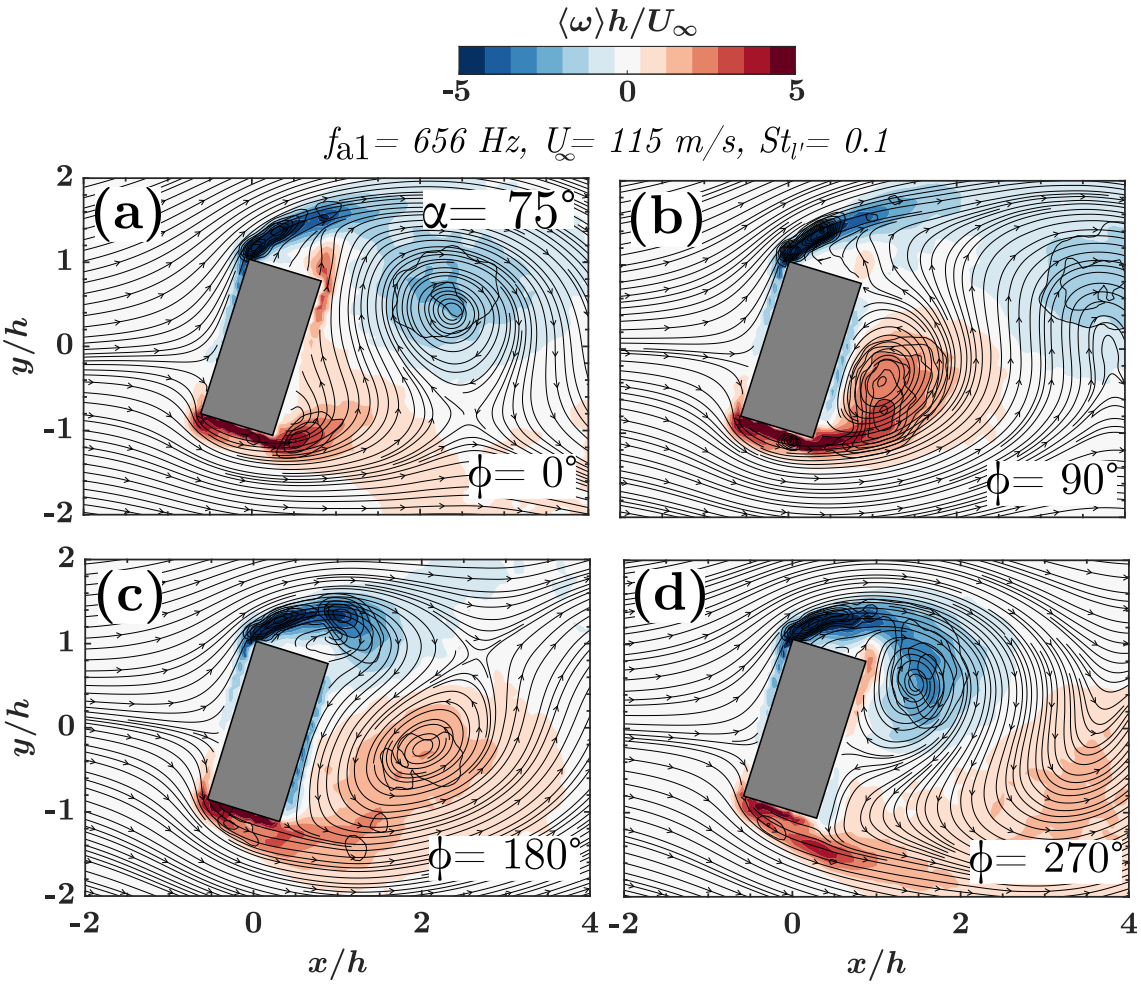

Figure 4.20: Phase-locked vorticity field with the streamlines superimposed over a complete acoustic pressure cycle during acoustic first mode excitation f_{a1} for $\alpha = 75^{\circ}$ at $St_{l'} = 0.1$

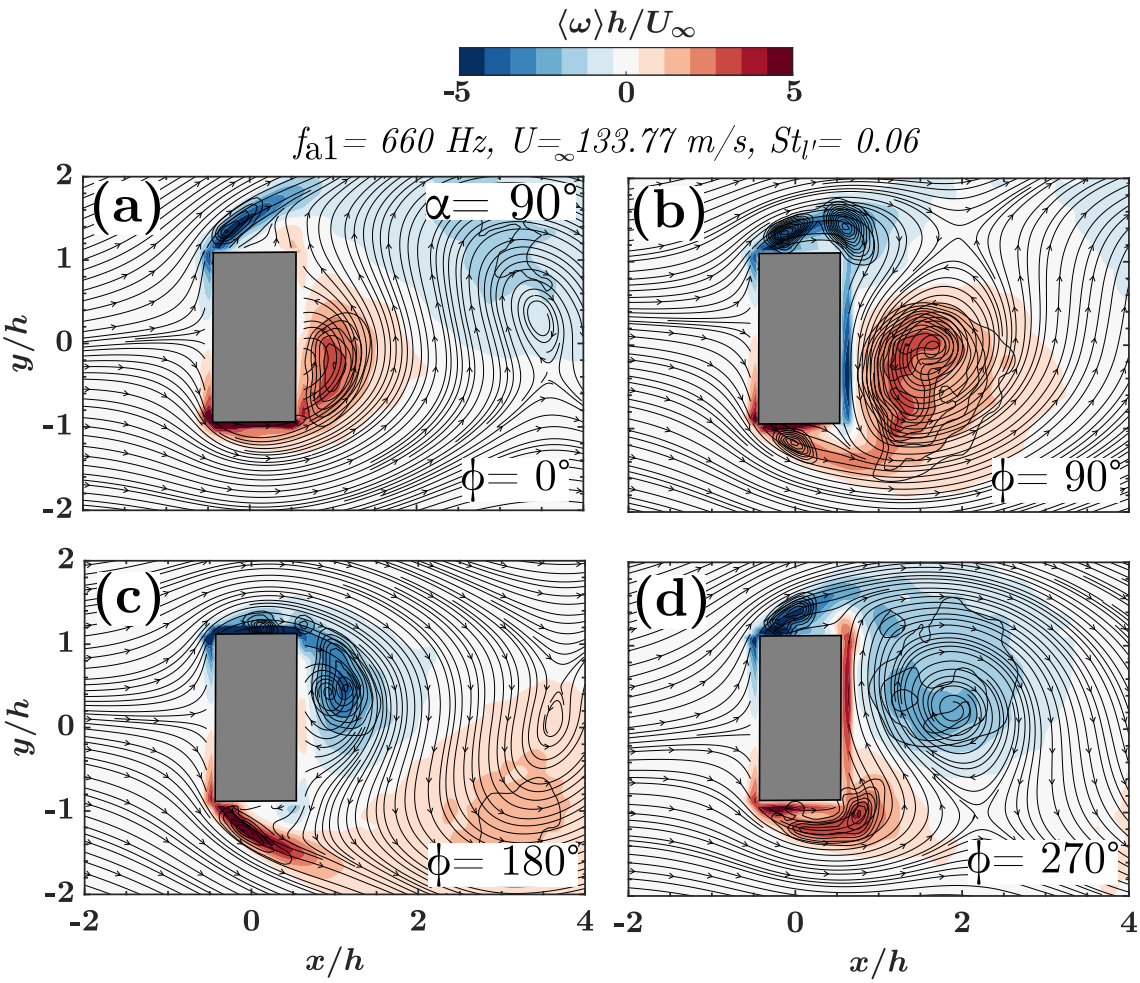

Figure 4.21: Phase-locked vorticity field with the streamlines superimposed over a complete acoustic pressure cycle during acoustic first mode excitation f_{a1} for $\alpha = 90°$ at $St_{l'} = 0.06$

Flow-sound energy transfer under resonant conditions

In our quest to unravel the complex interplay between flow and sound under resonant conditions, and to illuminate the self-selection mechanism of the inherent flow instabilities, a hybrid model that combines numerical and experimental parameters is employed. This model assesses the transfer of aeroacoustic energy between the fluid flow and the resultant acoustic field by implementing Howe (1980) [43] integral formulation of aerodynamic sound. The sound generated as a result of fluid flow is as follows

$$\frac{\partial^2 \rho}{\partial t^2} - c_0^2 \nabla^2 \rho = \frac{\partial^2}{\partial x_i \partial x_j} \left(\rho v_i v_j + p_{ij} - c_0^2 \rho \delta_{ij} \right). \tag{4.6}$$

Where v_i and v_j are the components of the fluid velocity in the i and j directions, respectively, p_{ij} represents the perturbed stress tensor of the fluid, and δ_{ij} is the Kronecker delta function, which equals 1 when $i = j$ and 0 otherwise. The term $\frac{\partial^2 \rho}{\partial t^2}$ describes the temporal acceleration of density fluctuations and the term $c_0^2 \nabla^2 \rho$ reflects the spatial variation of these density fluctuations. It's effectively the spatial "spread" of the acoustic wave.

It is important to note that the density ρ inherits fluctuations which are dependent on the spatial turbulent stress tensor. The challenge of deriving definitive solutions for Eq.(4.6) is anticipated, given that this formulation represents an integral variation of the Navier-Stokes equation. The source term within this equation embodies several aspects of fluid dynamics and acoustic interactions. It encompasses not only the generation of sound but also accounts for self-modulation brought about by acoustic non-linearity, convective influences from the flow, refractive shifts related to variations in sound speed, and attenuation stemming from thermal and viscous effects. Howe (1997) [44] seminal work proposed that the sound generation resulting from the fluctuating fluid forces driven by a vorticity field can be effectively modeled as

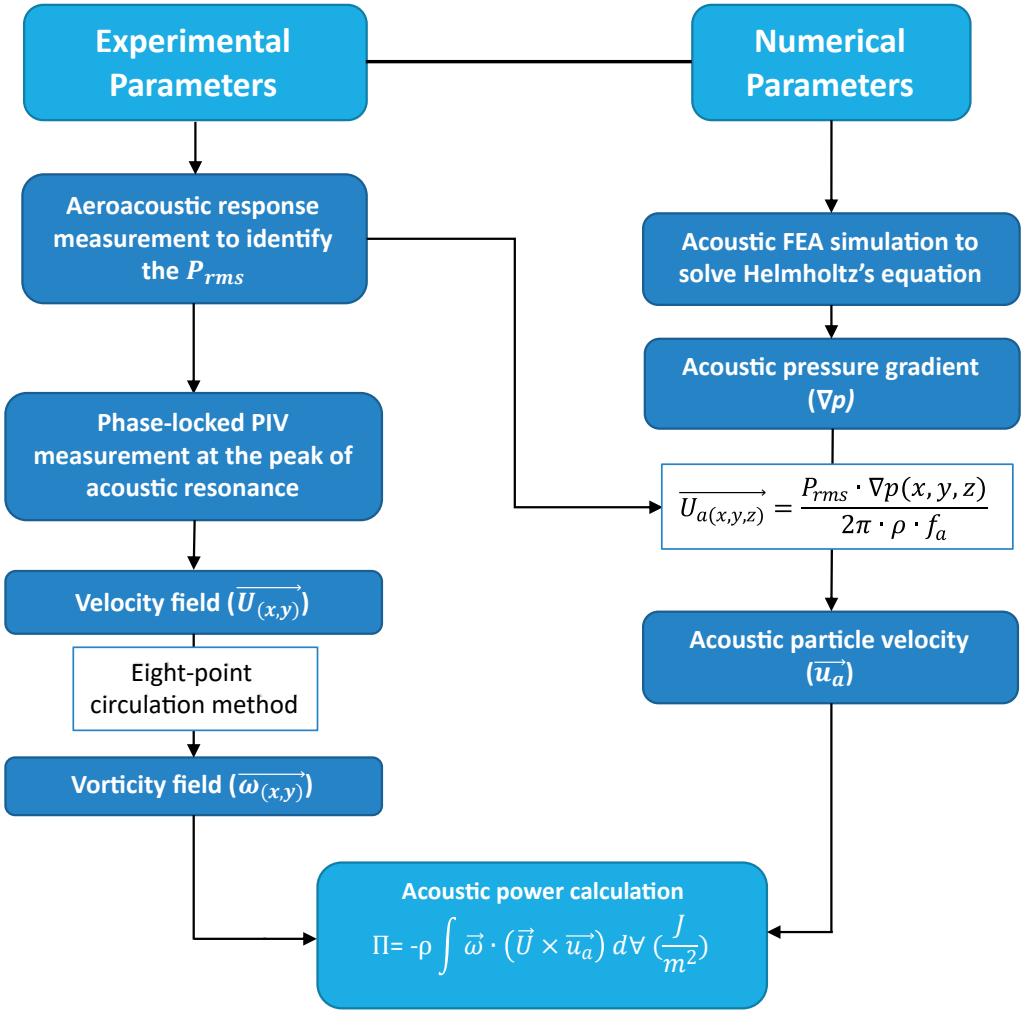

Figure 4.22: Hybrid experimental/numerical methodology implemented to compute the acoustic power production.

a dipole source. In a scenario with an incompressible flow field, characterized by vorticity $\vec{\omega}$, acoustic particle velocity $\vec{u}_a$, the acoustic pressure p, which is radiated from a localized dipole source, can be quantified as per the subsequent equation:

$$\frac{\partial^2 p}{\partial^2 t} - \nabla^2 p = c_0 \rho_0 \nabla \cdot (\vec{\omega} \times \vec{u}_a) \,. \tag{4.7}$$

Thus, to calculate the acoustic power, denoted as Π, evaluation of the integral (over a unit area) of the dot product of the vorticity vector $\vec{\omega}$ and the cross product of the instantaneous flow velocity vector $\vec{U}$ and the acoustic particle velocity vector $\vec{u}_a$ is performed. This result is then multiplied by the fluid local density to derive the final acoustic power Π (J/m^2).

$$\Pi = -\rho \int \vec{\omega} \cdot \left(\vec{U} \times \vec{u}_a \right) d\forall \tag{4.8}$$

The algorithm is designed to calculate both the spatial distribution of net and instantaneous acoustic sources and sinks in proximity to the rectangular cylinder during self-excited acoustic resonance. This methodology assists in pinpointing the regions where large-scale vortices function as acoustic sources and the areas where they serve as sinks. By distinguishing these regions, a deeper understanding is obtained of the dynamic behavior of vortices in different flow conditions and their influence on self-excited acoustic resonance. In order to carry out this method, an experimental measurement of the acoustic pressure during resonance is required to ascertain the acoustic pressure (P_{rms}). Phase-locked Particle Image Velocimetry (PIV) is conducted at eight distinct phases of the acoustic pressure cycle to define the two-dimensional velocity field. Subsequently, the vorticity field ($\vec{\omega}$) is computed using the eight-point circulation method suggested by Raffel et al. (2018) [97].

Next, a numerical simulation is carried out to derive the two-dimensional spatial

distribution of the acoustic particle velocity at the mid-plane, which aligns with the plane where the PIV measurements are conducted. The solution to the Helmholtz equation, calculated through a finite element analysis (FEA), provides the distribution of both acoustic pressure and acoustic particle velocity at the selected plane for various acoustic transverse modes. The Helmholtz equation for sound pressure in a moving fluid is given as follows:

$$\nabla^2\varphi + k^2\varphi = 0, \tag{4.9}$$

where ∇^2 is the Laplacian operator and the $k = 2\pi f_a/c$ is the wavenumber. The acoustic pressure as a function of time can be modeled as a simple harmonic wave as follows:

$$p(x, y, z, t) = \varphi(x, y, z)e^{i(2\pi f_a)t} \tag{4.10}$$

Solving Eq. (4.9) and (4.10) over the two-dimensional domain with $30l$ upstream and downstream distance to employ the zero acoustic pressure boundary condition. The domain is discretised with quadrilateral mesh. Euler's equation is used to derive the acoustic particle velocity distribution from the acoustic pressure distribution

$$\rho\frac{\partial\vec{u}_a}{\partial t} = -\nabla p \tag{4.11}$$

To obtain the spatial field of the acoustic particle velocity $\vec{U}_a$ at the frequency of excitation, equation (4.11) is integrated giving the following

$$\vec{U}_a(x, y, z) = \frac{\nabla\hat{p}(x, y, z)}{2\pi \cdot \rho \cdot f_{a1,a3,a5}}, \tag{4.12}$$

Where P_{rms} is acoustic pressure (rms) obtained experimentally and $\hat{p}(x, y, z, t)$ is the spectral amplitude of the pressure distribution obtained after solving Eq. (4.9) and (4.10) numerically. It is important to note that the acoustic particle velocity $\vec{U}_a$

leads the acoustic pressure by 90° during acoustic resonance ([3]). Thus, the acoustic particle velocity vector as a function of time $\vec{u}_a(x, y, z, t)$ is calculated as follows over the acoustic pressure cycle

$$\vec{u}_a(x, y, z, t) = \vec{U}_a(x, y, z)e^{i(2\pi f_a t + \pi/2)}. \tag{4.13}$$

Afterward, all the needed parameters are plugged into Eq. (4.8) to compute the instantaneous and net acoustic pressure $\Pi(x, y, t)$. Figure 4.22 summarizes the methodology used to compute the acoustic power production.

Figure 4.23(a, b) shows the instantaneous acoustic power (Π) calculated at two instants of the acoustic pressure cycle $\phi = 0°$ and $\phi = 180°$ respectively along with the computationally obtained acoustic particle velocity distribution for the case $\alpha = 0°$. Figure 4.23(c, d) resembles the normalized net acoustic power. To compute the net acoustic power, the acoustic power is integrated within a transverse spatial bound $y = \pm 2h$ and streamwise spatial bound $-2 < x/h < 4$. Plotting the acoustic energy transfer can provide valuable understanding of the vortex formation process and the areas where positive or negative energy exchange occurs between the flow and the sound field. Positive acoustic power values indicate that the region is acting as an acoustic source. This implies that the flow is continuously transmitting energy to the sound field to maintain a resonant condition. On the other hand, a negative value of the acoustic power highlights a region where there is a local acoustic sink as the flow is absorbing energy from the flow field to correlate and sustain the large-scale vortical structures. In the discussed cases, the third acoustic mode is excited, where the acoustic particle velocity is in the negative direction around the cylinder at acoustic pressure phase $\phi = 0°$ and positive at acoustic pressure phase $\phi = 0°$. As shown in Figure 4.23(a), an acoustic sink is present within the upper vicinity of the rod and at

the upper TE. This matches the finding in Figure 4.11(a), as this phase corresponds to the formation of a trailing edge vortex and the convection of a LE vortex within the upper span of the cylinder. Afterwards this vortex turns into an acoustic source as it shed downstream at $\phi = 180°$. Looking at the net normalized acoustic power distribution in Figure 4.23(c, d), alternating acoustic sources and sinks are present within the span of the cylinder, which is attributed to the LE vortex alternating between being a source and a sink as the acoustic particle velocity is alternating. This is a strong evidence that the LE vortex fully forms at the LE and, as it convects downstream to the TE, it contributes to the acoustic field. A strong acoustic sink is present just downstream of the cylinder. This is attributed to the formation of TE vorticies as the vortex formation process absorbs energy from the acoustic field. Such findings elucidate the synchronization between the LE vorticies, TE vorticies and the acoustic field to sustain the ILEV/TEVS instability.

Moving to the case of $\alpha = 5°$ at $St_{l'} = 1.21$, Figure 4.24 shows that at the two out of phase instants, there is a stream of acoustic sources and sinks within the shear layer alternating between the upper and lower shear layers as the acoustic particle velocity switches its direction. This is because the vortex production is continuous and is within the shear layer as evident from Figure 4.13. Looking at the net acoustic power distribution, local alternating sources and sinks are present with the upper and lower shear layers. This outlines the isolation between the upper and lower shear layers, since there is no spatially extended source or sink in the transverse direction. Interestingly, a significant acoustic source is present at the upper TE of the cylinder. Looking back at Figure 4.13, it is obvious that this point is a shear layer impingement point that generates sound and acts as an acoustic source over the pressure cycle. Moreover, Figure 4.24(d) depicts two sinusoidal net acoustic power alternations compared to only one observed for the previous case. This is attributed

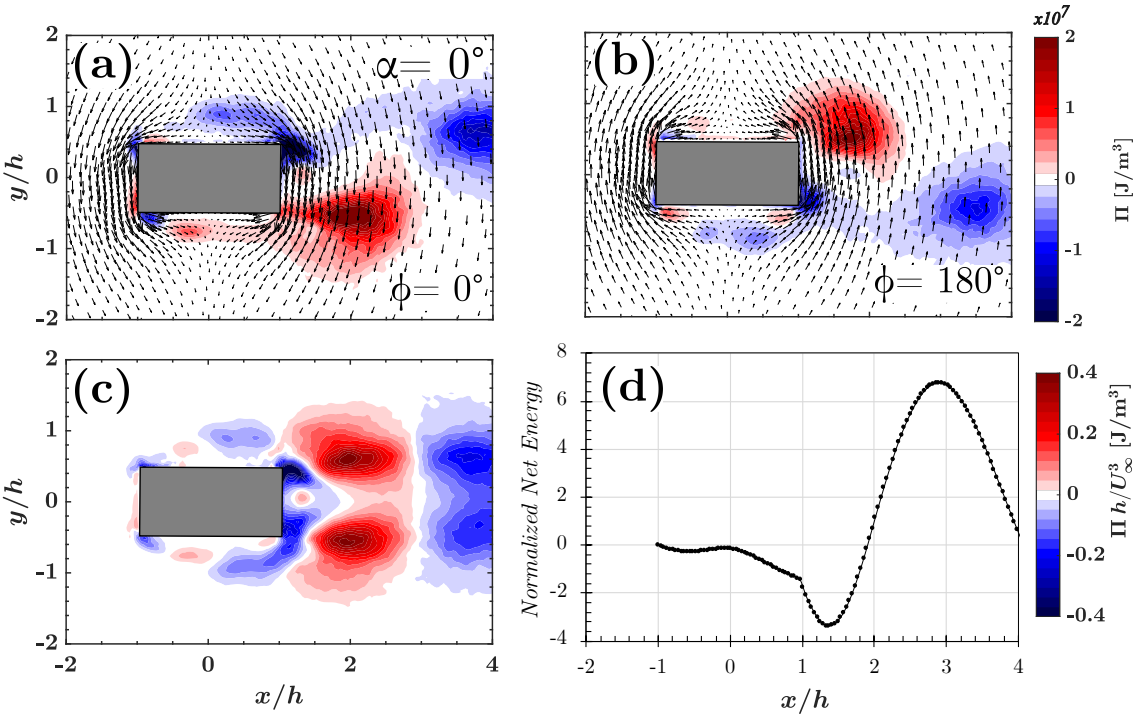

Figure 4.23: Instantaneous acoustic power (Π) calculated at two instants of the acoustic pressure cycle $\phi = 0°$ and $\phi = 180°$ respectively with the acoustic particle velocity U_a vectors superimposed (a, b); normalized net acoustic power over one pressure cycle ($\Pi h/U_\infty^3$) (c, d) during third acoustic mode excitation f_{a3} for $\alpha = 0°$ at $St_{l'} = 0.6$.

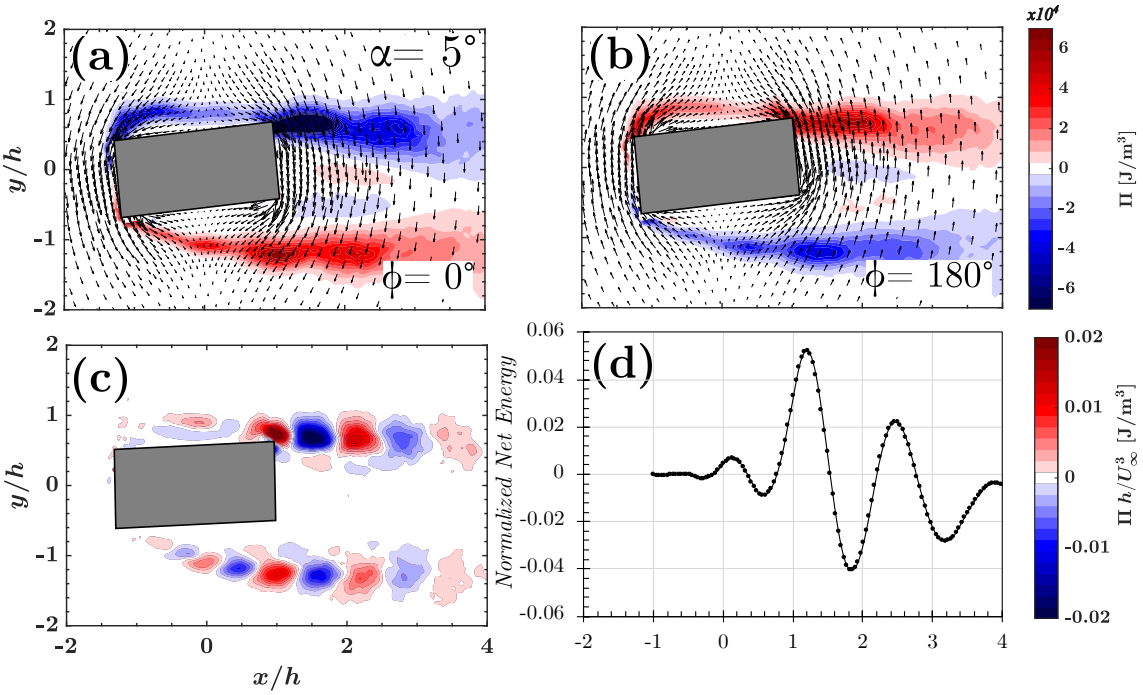

Figure 4.24: Instantaneous acoustic power (Π) calculated at two instants of the acoustic pressure cycle $\phi = 0°$ and $\phi = 180°$ respectively with the acoustic particle velocity U_a vectors superimposed (a, b); normalized net acoustic power over one pressure cycle ($\Pi h/U_\infty^3$) (c, d) during third acoustic mode excitation f_{a3} for $\alpha = 5°$ at $St_{l'} = 1.21$

to the different mode number of ILEVS/TEVS shedding mode associated with each case. Figure 4.25 shows the instantaneous and total acoustic power for the same angle of incidence $\alpha = 5°$ but at the point of coincidence with $St_{l'} = 0.6$. The acoustic source and sinks are similar to the case of $\alpha = 0°$ with a strong acoustic sink forming at the TE at $\phi = 0°$ which corresponds to the formation of the TE vortex. This emphasizes on the fact the shedding mechanism for these two cases at these point of coincidence is the same which is ILEV/TEVS with n=1.

At $\alpha = 10°$, which corresponds to a natural shedding mode, the net acoustic power is negative in the near wake due to the formation of large-scale vortices. However, there is no net power production or absorption along the span of the cylinder as evident from Figure 4.26. This is due to the absence of LE vortices which is evident

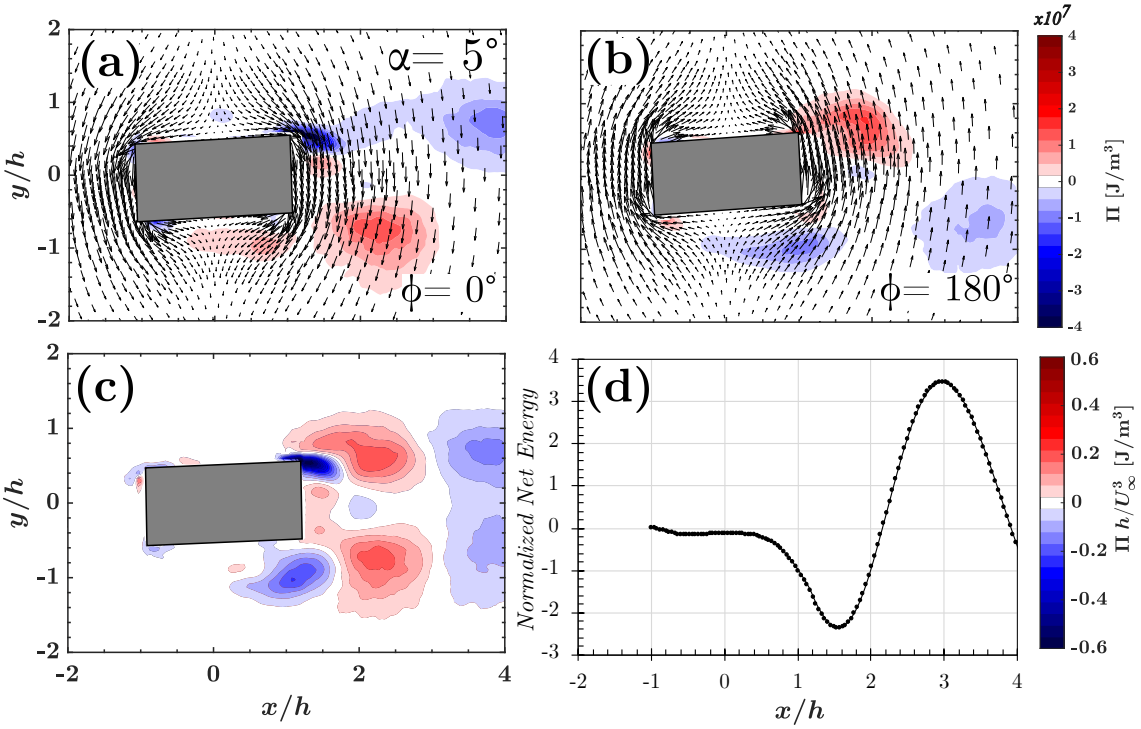

Figure 4.25: Instantaneous acoustic power (Π) calculated at two instants of the acoustic pressure cycle $\phi = 0°$ and $\phi = 180°$ respectively with the acoustic particle velocity U_a vectors superimposed (a, b); normalized net acoustic power over one pressure cycle ($\Pi h/U_\infty^3$) (c, d) during third acoustic mode excitation f_{a3} for $\alpha = 5°$ at $St_{l'} = 0.6$

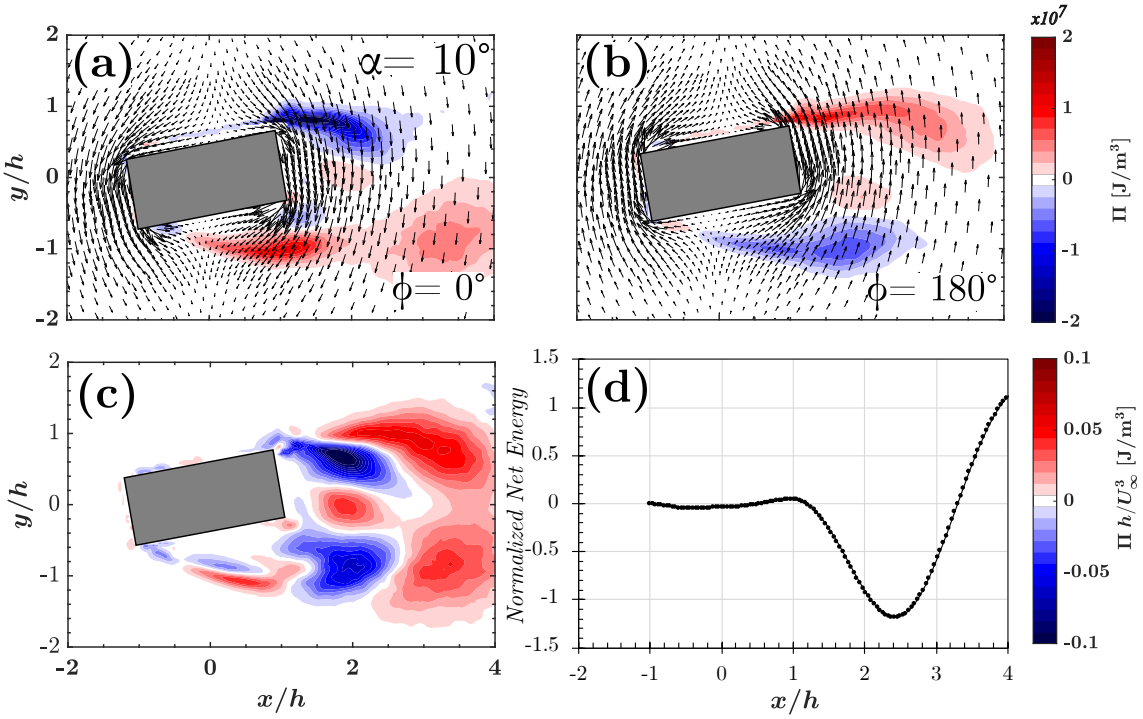

Figure 4.26: Instantaneous acoustic power (Π) calculated at two instants of the acoustic pressure cycle $\phi = 0°$ and $\phi = 180°$ respectively with the acoustic particle velocity U_a vectors superimposed (a, b); normalized net acoustic power over one pressure cycle ($\Pi h/U_\infty^3$) (c, d) during third acoustic mode excitation f_{a3} for $\alpha = 10°$ at $St_{l'} = 0.29$

from figure 4.17. So, the vortex formation and convection are mainly present in the cylinder wake.

4.3.3 Conclusions

Flow visualization methodologies have clearly demonstrated that the wake structure of a rectangular cylinder with an aspect ratio (AR) of 2 is strongly influenced by the incidence angle under non-resonant conditions. Furthermore, under acoustic perturbations triggered during resonance excitation, the inherent shear layer instability with a $St_{l'} = 0.6n$ can couple with an acoustic transverse mode given a frequency coincidence. However, this instability is completely undetectable under non resonant

conditions.

In the case of an incidence angle of $\alpha = 0°$, the ILEV/TEVS instability mode with $n = 1$ arises when its frequency synchronizes with the third transverse acoustic mode. This ILEV/TEVS instability mode was reported in the literature only when the aspect ratio of the cylinder was much larger than 3 (i.e. $AR > 3$) under non-resonant conditions. For an incidence angle of $\alpha = 5°$, the ILEV/TEVS instabilities of $n = 1$ and $n = 2$ are observed under resonant conditions at different flow velocities. These different velocities correspond to the coincidence of two separate Strouhal lines with the third acoustic mode. The ILEV/TEVS instability of $n = 2$ is reported in the literature for $6 < AR < 9$ under non-resonant conditions. Such observations underscore that the combined effect of the angle of incidence and self-excited acoustic resonance can exert a substantial influence on the effective streamwise length of the cylinder. Beyond $\alpha = 5°$, only natural vortex shedding, characterized by a hybrid LEVS/TEVS mode, is observed under both resonant and non-resonant conditions. However, during resonance, an increase in the correlation and vortex strength is noted. The work presented in this chapter shows that the excited resonant mode that was reported in the literature by Stokes & Welsh (1986) [121] is in fact due to a coupling with the inherent 'ILEV' instability as reported by Nakamura et al. (1991) [79].

Chapter 5

Conclusions and Recommendations

5.1 Summary and conclusions

This research has furnished a wealth of experimental results, deepening our understanding of the complex interplay between flow and sound in the context of rectangular cylinders. By investigating a variety of factors such as aspect ratios, edge geometries, and angles of incidence, we have broadened the scope of our knowledge in this area. The findings elucidated intricate mechanisms governing fluid-structure interactions, shedding light on how physical characteristics of rectangular cylinders influence these complex dynamics. This, in turn, lays a robust foundation for future work in this realm, further driving advancements in the field. Here is a list of the main conclusions of this study:

1. The cases with $l/h = 1$ and $l/h = 0.5$ displayed standard vortex shedding progression, locking in to the initial acoustic mode with Strouhal numbers of 0.14 and 0.06 respectively. For the situations where $l/h = 2$, both scenarios with all-sharp edges and downstream-rounded edges showcased similar aeroacoustic responses. Both had a Strouhal number of $\mathrm{St}l \approx 0.16 - 0.18$, coupled with a

sudden excitation of the third acoustic mode. In contrast, cases with upstream-rounded edges and fully rounded edges exhibited a Strouhal number of St$l \approx 0.5 - 0.52$, along with a conventional excitation of both the first and third acoustic modes in sync with the frequency of wake shedding. The interaction mechanism between the duct's higher acoustic modes and the obscured shear layer instability is contingent upon the rod's length, l. Therefore, to prompt an early excitation of the duct's third transverse acoustic mode, the rod length l should be adequately lengthy.

2. Outside of acoustic resonance excitation, rounding the upstream edge appeared to significantly reduce the dynamic lift force due to the absence of the leading edge vorticies and the major change in the Strouhal number.

3. The onset of shear layer instability which is only self-excited by acoustic coupling impose significantly less hydrodynamic loading on the cylinder.

4. The unexpected excitation of the third acoustic mode in cases with sharp edges and downstream-rounded edges can be attributed to the couple between the shear layer instability shedding mode and the duct's acoustic mode. While this mode was entirely obscured prior to the early initiation of the third mode, it seems the third acoustic mode served as an external forcing element. This reinforced the mode and established a coupling with it, thereby manifesting acoustic resonance. This is evident from the phase-locked PIV measurments performed. The wake structure of a rectangular cylinder with an aspect ratio (AR) of 2 is significantly influenced by the incidence angle under non-resonant conditions, as revealed by flow visualization methodologies.

5. Under resonant conditions, the masked shear layer instability with a $St_{l'} = 0.6n$ can engage in a coupling with an acoustic transverse mode if a frequency

coincidence exists. This instability, however, remains undetectable under non-resonant conditions.

6. For an incidence angle of $\alpha = 5°$, the ILEV/TEVS instabilities of $n = 1$ and $n = 2$ are observable under resonant conditions at differing flow velocities. These velocities correspond to the coincidence of two separate Strouhal lines with the third acoustic mode. The ILEV/TEVS instability of $n = 2$ is reported for $6 < AR < 9$ under non-resonant conditions.

7. The combined influence of the angle of incidence and self-excited acoustic resonance can substantially affect the effective streamwise length of the cylinder.

8. Beyond $\alpha = 5°$, only natural vortex shedding, characterized by a hybrid LEV-S/TEVS mode, is observed under both resonant and non-resonant conditions. Nonetheless, during resonance, the correlation and vortex strength increase.

5.2 Recommendations for future investigations

To complement this study, some other investigations can be done to further understand the complex interaction between flow and sound during resonance during acoustic resonance excitation. Here are some suggested avenues for future research:

1. Future work should explore aspect ratios greater than 2, which naturally exhibit ILEV/TEVS shedding patterns. It would be insightful to understand how self-excited acoustic resonance impacts these specific shedding patterns, potentially influencing their onset, magnitude, and frequency.

2. Investigate the combined influence of the angle of incidence and edge modifications, such as chamfering and rounding, during self-excited acoustic resonance.

This could shed light on how these factors work in conjunction to affect the overall dynamics and acoustics of the system.

3. Another promising area of investigation involves examining the concurrent influence of forced oscillation and acoustic resonance on the shear layer's response. Such a study could provide vital insights into the complex interplay between these factors and further our understanding of fluid-sound-structure interactions.

4. Stoneman et al. (1988) [122] introduced noteworthy findings regarding the relationship between the cross-stream length and spacing of cylinders in tandem configurations in relation to the acoustic pressure generated during resonance. However, to better comprehend this intriguing relationship and its implications, a more comprehensive study could be carried out. For instance, investigating different aspect ratios would provide an understanding of how the this ratio affects the acoustic response. Moreover, varying the spacing ratio, or the distance between the cylinders in comparison to their cross-stream length, can elucidate the role of spatial arrangement in acoustic resonance. These investigations can lead to the establishment of proximity and isolation criteria for rectangular cylinders placed in tandem arrangements.

5. A key recommendation is to perform direct measurements of the hydrodynamic loading on the rectangular cylinder for all previously mentioned studies. As indicated in our research, changes in the behavior of the shear layer could have significant effects on hydrodynamic loading. Future studies need to consider these effects for a more comprehensive understanding of flow-structure interactions.

Bibliography

[1] Abdelmwgoud, M., Shaaban, M., and Mohany, A. Flow dynamics and azimuthal behavior of the self-excited acoustic modes in axisymmetric shallow cavities. *Physics of Fluids 32*, 11 (2020), 115109.

[2] Alziadeh, M., and Mohany, A. Vortex dynamics of tandem bare and spiral finned cylinders in cross-flow and their susceptibility to acoustic resonance excitation. *Physics of Fluids 34*, 4 (04 2022), 045105.

[3] Alziadeh, M., and Mohany, A. Flow structure and aerodynamic forces of finned cylinders during flow-induced acoustic resonance. *Journal of Fluids and Structures 119* (2023), 103887.

[4] Arafa, N., and Mohany, A. Aeroacoustic Response of a Single Cylinder With Straight Circular Fins in Cross-Flow. *Journal of Pressure Vessel Technology 137*, 5 (10 2015), 051301.

[5] Arafa, N., and Mohany, A. Wake structures and acoustic resonance excitation of a single finned cylinder in cross-flow. *Journal of Fluids and Structures 86* (2019), 70–93.

[6] Arafa, N., Tariq, A., Mohany, A., and Hassan, M. Effect of cylinder location inside a rectangular duct on the excitation mechanism of acoustic resonance. *Canadian Acoustics 42*, 1 (Mar. 2014), 33–40.

[7] Bearman, P. W. On vortex street wakes. *Journal of Fluid Mechanics 28*, 4 (1967), 625–641.

[8] Bearman, P. W., and Obasaju, E. D. An experimental study of pressure fluctuations on fixed and oscillating square-section cylinders. *Journal of Fluid Mechanics 119* (1982), 297–321.

[9] Bearman, P. W., and Trueman, D. M. An investigation of the flow around rectangular cylinders. *Aeronautical Quarterly 23* (8 1972), 229–237.

[10] Bernard, H. Formation de centres de giration a l'arriere d'un obstacle en movement. *C.R. Hebd Seances Acad. Sci. 147* (1912), 49–59.

[11] Blake, W. K., Ed. *Mechanics of Flow-Induced Sound and Vibration, Volume 1 (First Edition)*, first edition ed. Academic Press, 1986.

[12] Blevins, R. Review of sound induced by vortex shedding from cylinders. *Journal of Sound and Vibration 92*, 4 (1984), 455–470.

[13] Blevins, R. D. The effect of sound on vortex shedding from cylinders. *Journal of Fluid Mechanics 161* (1985), 217–237.

[14] Briggs, R. J. *Electron-stream interaction with plasmas [by] Richard J. Briggs.* M.I.T. Press Cambridge, 1964.

[15] Bunge, U., Gurr, A., and Thiele, F. Numerical aspects of simulating the flow-induced oscillations of a rectangular bluff body. *Journal of Fluids and Structures 18*, 3 (2003), 405–424. Bluff-body/Flow interactions.

[16] Carassale, L., Freda, A., and Marrè-Brunenghi, M. Experimental investigation on the aerodynamic behavior of square cylinders with rounded corners. *Journal of Fluids and Structures 44* (2014), 195–204.

[17] Carberry, J., Sheridan, J., and Rockwell, D. Forces and wake modes of an oscillating cylinder. *Journal of Fluids and Structures 15*, 3 (2001), 523–532.

[18] Chandrasekhar, S. *Hydrodynamic and hydromagnetic stability*. 1961.

[19] Chen, J. M., and Liu, C.-H. Vortex shedding and surface pressures on a square cylinder at incidence to a uniform air stream. *International Journal of Heat and Fluid Flow 20* (1999), 592–597.

[20] Cheng, M., Whyte, D., and Lou, J. Numerical simulation of flow around a square cylinder in uniform-shear flow. *Journal of Fluids and Structures 23*, 2 (2007), 207–226.

[21] Cherry, N. J., Hillier, R., and Latour, M. E. M. P. Unsteady measurements in a separated and reattaching flow. *Journal of Fluid Mechanics 144* (1984), 13–46.

[22] Crandall, S. H., Vigander, S., and March, P. A. Destructive Vibration of Trashracks due to Fluid-Structure Interaction. *Journal of Engineering for Industry 97*, 4 (11 1975), 1359–1365.

[23] Curle, N. The influence of solid boundaries upon aerodynamic sound. *Proceedings of the Royal Society of London. Series A. Mathematical and Physical Sciences 231* (1955), 505 – 514.

[24] Dai, S. S. Prediction of turbulent flow around a square cylinder with rounded corners.

[25] Deniz, S., and Staubli, T. Oscillating rectangular and octagonal profiles: Interaction of leading- and trailing-edge vortex formation. *Journal of Fluids and Structures 11*, 1 (1997), 3–31.

[26] Dobre, A., H. H. Investigation of the three-dimensional intermediate wake topology for a square cylinder at high reynolds number 200-103. *Journal of Wind Engineering and Industrial Aerodynamics 37*, 1 (2004), 518–530.

[27] Drazin, P. G., and Reid, W. H. *Hydrodynamic Stability*, 2 ed. Cambridge Mathematical Library. Cambridge University Press, 2004.

[28] Durfio, D. F. G. Measurements of turbulent and periodic flows around a square cross-section cylinder.

[29] Dutta, S., Muralidhar, K., and Panigrahi, P. Influence of the orientation of a square cylinder on the wake properties. *Experiments in Fluids 34* (01 2003), 16–23.

[30] Eisinger, F. L., and Sullivan, R. E. Unusual Acoustic Vibration in Heat Exchanger and Steam Generator Tube Banks Possibly Caused by Fluid-Acoustic Instability. *Journal of Engineering for Gas Turbines and Power 115*, 2 (04 1993), 411–417.

[31] Esfeh, M., Sohankar, A., and Shirani, E. Influence of rounding corners on the wake of a finite-length cylinder: An experimental study. *International Journal of Heat and Fluid Flow 91* (10 2021), 108854.

[32] Fage, A., and Johansen, F. C. On the flow of air behind an inclined flat plate of infinite span. *Proceedings of the Royal Society of London. Series A, Containing Papers of a Mathematical and Physical Character 116*, 773 (1927), 170–197.

[33] Fujita, H., Sha, W., Furutani, H., and Suzuki, H. Experimental investigations and prediction of aerodynamic sound generated from square cylinders.

[34] Gartshore, I. *The Effects of Free Stream Turbulence on the Drag of Rectangular Two-dimensional Prisms*. Boundary Layer Wind Tunnel Laboratory: Boundary Layer Wind Tunnel Laboratory. Boundary Layer Wind Tunnel Laboratory, Faculty of Engineering Science, University of Western Ontario, 1973.

[35] Gerrard, J. H. The mechanics of the formation region of vortices behind bluff bodies. *Journal of Fluid Mechanics 25*, 2 (1966), 401–413.

[36] Gonçalves da Silva Pinto, W. J., and Margnat, F. Shape optimization for the noise induced by the flow over compact bluff bodies. *Computers and Fluids 198* (Feb. 2020), 104400.

[37] Grove, A. S., Shair, F. H., and Petersen, E. E. An experimental investigation of the steady separated flow past a circular cylinder. *Journal of Fluid Mechanics 19*, 1 (1964), 60–80.

[38] Hillier, R., and Cherry, N. The effects of stream turbulence on separation bubbles. *Journal of Wind Engineering and Industrial Aerodynamics 8*, 1 (1981), 49–58.

[39] Ho, C., and Huerre, P. Perturbed free shear layers. *Annual Review of Fluid Mechanics 16*, 1 (1984), 365–422.

[40] Ho, C.-M., and Nosseir, N. S. Dynamics of an impinging jet. part 1. the feedback phenomenon. *Journal of Fluid Mechanics 105* (1981), 119–142.

[41] Hourigan, K., Thompson, M. C., and Tan, B. T. Self-sustained oscillations in flows around long blunt plates. *Journal of Fluids and Structures 15* (2001), 387–398.

[42] Howe, M. The dissipation of sound at an edge. *Journal of Sound and Vibration 70*, 3 (1980), 407–411.

[43] Howe, M. S. The dissipation of sound at an edge. *Journal of Sound and Vibration 70* (1980), 407–411.

[44] Howe, M. S. Sound generated by fluid-structure interactions. *Computational Structures 65* (1997), 433–446.

[45] Hu, J., Zhou, Y., and Dalton, C. Effects of the corner radius on the near wake of a square prism. *Experiments in Fluids 40* (10 2006), 106–118.

[46] Huang, R., Lin, B., and Yen, S. Time-averaged topological flow patterns and their influence on vortex shedding of a square cylinder in crossflow at incidence. *Journal of Fluids and Structures 26*, 3 (2010), 406–429.

[47] Huerre, P., and Monkewitz, P. A. Local and global instabilities in spatially developing flows. *Annual Review of Fluid Mechanics 22*, 1 (1990), 473–537.

[48] Hunt, J. C. R., Abell, C. J., Peterka, J. A., and Woo, H. Kinematical studies of the flows around free or surface-mounted obstacles; applying topology to flow visualization. *Journal of Fluid Mechanics 86* (May 1978), 179–200.

[49] Igarashi, T. Characteristics of the flow around a square prism. *Bulletin of JSME 27*, 231 (1984), 1858–1865.

[50] Islam, M. R., and Mohany, A. Vortex shedding characteristics in the wake of circular finned cylinders. *Physics of Fluids 32*, 4 (2020), 045113.

[51] Islam, M. R., Shaaban, M., and Mohany, A. Vortex dynamics and acoustic sources in the wake of finned cylinders during resonance excitation. *Physics of Fluids 32*, 7 (07 2020), 075117.

[52] Islam, M. R., Shaaban, M., and Mohany, A. Vortex dynamics and acoustic sources in the wake of finned cylinders during resonance excitation. *Physics of Fluids 32*, 7 (07 2020). 075117.

[53] Islam, S., Zhou, C., Shah, A., and Xie, P. Numerical simulation of flow past rectangular cylinders with different aspect ratios using the incompressible lattice boltzmann method. *Journal of Mechanical Science and Technology 26* (04 2012).

[54] Johns, K., and Dexter, R. The development of fatigue design load ranges for cantilevered sign and signal support structures. *Journal of Wind Engineering and Industrial Aerodynamics 77-78* (1998), 315–326.

[55] Karniadakis, G. E., and Triantafyllou, G. S. Frequency selection and asymptotic states in laminar wakes. *Journal of Fluid Mechanics 199* (1989), 441–469.

[56] Kiya, M., and Sasaki, K. Structure of a turbulent separation bubble. *Journal of Fluid Mechanics 137* (1983), 83–113.

[57] Knisely, C. Strouhal numbers of rectangular cylinders at incidence: A review and new data. *Journal of Fluids and Structures 4*, 4 (1990), 371–393.

[58] Knisely, C., Matsumoto, M., and Menacher, F. Rectangular cylinders in flows with harmonic perturbations. *Journal of Hydraulic Engineering 112*, 8 (1986), 690–704.

[59] Kravchenko, A., and Moin, P. Numerical studies of flow over a circular cylinder at red = 3900. *Physics of Fluids 12* (02 2000).

[60] Kurtulus, D. F., Scarano, F., and David, L. Unsteady aerodynamic forces estimation on a square cylinder by TR-PIV. *Experiments in Fluids 42*, 2 (Feb. 2007), 185–196.

[61] Lander, D. C., Letchford, C. W., Amitay, M., and Kopp, G. A. Influence of the bluff body shear layers on the wake of a square prism in a turbulent flow. *Phys. Rev. Fluids 1* (Aug 2016), 044406.

[62] Lighthill, M. J., and Newman, M. H. A. On sound generated aerodynamically i. general theory. *Proceedings of the Royal Society of London. Series A. Mathematical and Physical Sciences 211*, 1107 (1952), 564–587.

[63] Luo, S., Tong, X., and Khoo, B. Transition phenomena in the wake of a square cylinder. *Journal of Fluids and Structures 23*, 2 (2007), 227–248.

[64] Lyn, D. A., Einav, S., Rodi, W., and Park, J.-H. A laser-doppler velocimetry study of ensemble-averaged characteristics of the turbulent near wake of a square cylinder. *Journal of Fluid Mechanics 304* (1995), 285–319.

[65] Lyn, D. A., and Rodi, W. The flapping shear layer formed by flow separation from the forward corner of a square cylinder. *Journal of Fluid Mechanics 267* (1994), 353–376.

[66] Merati, P., and Adrian, R. Feedback amplification of a plane shear layer by impingement on a downstream body. *Journal of Fluids and Structures 6*, 4 (1992), 415–436.

[67] MILLS, R., SHERIDAN, J., and HOURIGAN, K. Particle image velocimetry and visualization of natural and forced flow around rectangular cylinders. *Journal of Fluid Mechanics 478* (2003), 299–323.

[68] Mills, R., Sheridan, J., Hourigan, K., and Welsh, M. The mechanism controlling vortex shedding from rectangular bluff bodies. In *Proceedings of the Twelfth Australasian Fluid Mechanics Conference* (1995), Sidney University Press, pp. 227–230.

[69] Mohany, A. Self-excited acoustic resonance of isolated cylinders in cross-flow. *AECL Nuclear Review 1*, 1 (2012), 45–55.

[70] Mohany, A., and Ziada, S. A Parametric Study of the Resonance Mechanism of Two Tandem Cylinders in Cross-Flow. *Journal of Pressure Vessel Technology 131*, 2 (12 2008).

[71] Mohany, A., and Ziada, S. Effect of acoustic resonance on the dynamic lift forces acting on two tandem cylinders in cross-flow. *Journal of Fluids and Structures 25*, 3 (2009), 461–478.

[72] Mohany, A., and Ziada, S. Effect of acoustic resonance on the dynamic lift forces acting on two tandem cylinders in cross-flow. *Journal of Fluids and Structures 25*, 3 (2009), 461–478.

[73] Mohany, A., and Ziada, S. Measurements of the dynamic lift force acting on a circular cylinder in cross-flow and exposed to acoustic resonance. *Journal of Fluids and Structures 27*, 8 (2011), 1149–1164.

[74] Monkewitz, P., and Nguyen, L. Absolute instability in the near-wake of two-dimensional bluff bodies. *Journal of Fluids and Structures 1*, 2 (1987), 165–184.

[75] Nakaguchi, H., Hashimoto, K., and Muto, S. An experimental study on aerodynamic drag of rectangular cylinders. *Journal of The Japan Society for Aeronautical and Space Sciences 16* (1968), 1–5.

[76] Nakamura, Y., and Hirata, K. Critical geometry of oscillating bluff bodies. *Journal of Fluid Mechanics 208* (1989), 375–393.

[77] Nakamura, Y., and Nakashima, M. Vortex excitation of prisms with elongated rectangular, h and cross-sections. *Journal of Fluid Mechanics 163* (1986), 149–169.

[78] Nakamura, Y., Ohya, Y., Ozono, S., and Nakayama, R. Experimental and numerical analysis of vortex shedding from elongated rectangular cylinders at low reynolds numbers 200-103. *Journal of Wind Engineering and Industrial Aerodynamics 65*, 1 (1996), 301–308.

[79] Nakamura, Y., Ohya, Y., and Tsuruta, H. Experiments on vortex shedding from flat plates with square leading and trailing edges. *Journal of Fluid Mechanics 222* (1991), 437–447.

[80] Nakiboğlu, G., and Hirschberg, A. Aeroacoustic power generated by multiple compact axisymmetric cavities: Effect of hydrodynamic interference on the sound production. *Physics of Fluids 24*, 6 (2012), 067101.

[81] Naudascher, E., and Rockwell, D. *Flow Induced Vibrations – An Engineering Guide*. A. A. Balkema, 1994.

[82] Norberg, C. Flow around rectangular cylinders: Pressure forces and wake frequencies. *Journal of Wind Engineering and Industrial Aerodynamics 49*, 1 (1993), 187–196.

[83] Ohya, Y. Note on a discontinuous change in wake pattern for a rectangular cylinder. *Journal of Fluids and Structures 8* (1994), 325–330.

[84] Okajima, A. Strouhal numbers of rectangular cylinders. *Journal of Fluid Mechanics 123* (1982), 379–398.

[85] Olsman, W., Willems, J., Hirschberg, A., Colonius, T., and Trieling, R. Flow around a naca0018 airfoil with a cavity and its dynamical response to acoustic forcing. *Experiments in Fluids 51* (08 2011), 493–509.

[86] Omer, A., Mohany, A., and M., H. Effect of impingement edge geometry on the acoustic resonance excitation and strouhal numbers in a ducted shallow cavity. *Wind and Structures 23*, 2 (2016), 91 – 107.

[87] Ongoren, A., and Rockwell, D. Flow structure from an oscillating cylinder part 1. mechanisms of phase shift and recovery in the near wake. *Journal of Fluid Mechanics 191* (1988), 197–223.

[88] Ota, T., Asano, Y., and ichi Okawa, J. Reattachment length and transition of the separated flow over blunt flat plates. *Jsme International Journal Series B-fluids and Thermal Engineering 24* (1981), 941–947.

[89] Otsuki, Y. (in japanese). In *5th Symp. on Wind Effects on Structures* (1978), p. 169.

[90] Ozgoren, M. Flow structure in the downstream of square and circular cylinders. *Flow Measurement and Instrumentation 17*, 4 (2006), 225–235.

[91] Ozono, S., Ohya, Y., Nakamura, Y., and Nakayama, R. Stepwise increase in the strouhal number for flows around flat plates. *International Journal of Numerical Methods for Fluids 15*, 9 (1992), 1025–1036.

[92] Parker, R. Resonance effects in wake shedding from parallel plates: Some experimental observations. *Journal of Sound and Vibration 4*, 1 (1966), 62–72.

[93] Parker, R., and Llewelyn, D. Flow induced vibration of cantilever mounted flat plates in an enclosed passage: An experimental investigation. *Journal of Sound and Vibration 25*, 3 (1972), 451–463.

[94] Parker, R., and Welsh, M. Effects of sound on flow separation from blunt flat plates. *International Journal of Heat and Fluid Flow 4*, 2 (1983), 113–127.

[95] Perrin, R., Braza, M., Cid, E., Cazin, S., Barthet, A., Sevrain, A., Mockett, C., and Thiele, F. Obtaining phase averaged turbulence properties in the near wake of a circular cylinder at high reynolds number using pod. *Experiments in Fluids 43* (08 2007), 341–355.

[96] Perry, A. E., Chong, M. S., and Lim, T. T. The vortex-shedding process behind two-dimensional bluff bodies. *Journal of Fluid Mechanics 116* (1982), 77–90.

[97] Raffel, M., Willert, C. E., Scarano, F., Kähler, C. J., Wereley, S. T., and Kompenhans, J. *Particle Image Velocimetry: A Practical Guide*. Springer, 2018.

[98] Rockwell. Organized Fluctuations Due to Flow Past a Square Cross Section Cylinder. *Journal of Fluids Engineering 99*, 3 (09 1977), 511–516.

[99] Rockwell, D. Active control of globally-unstable separated flows. In *Non-steady Fluid Dynamics* (Jan. 1990), pp. 379–394.

[100] Rockwell, D., and Naudascher, E. Review—Self-Sustaining Oscillations of Flow Past Cavities. *Journal of Fluids Engineering 100*, 2 (06 1978), 152–165.

[101] Rockwell, D. O. Organized Fluctuations Due to Flow Past a Square Cross Section Cylinder. *Journal of Fluids Engineering 99*, 3 (09 1977), 511–516.

[102] Roshko, A. On the wake and drag of bluff bodies. *J. Aero. Sci. 22* (1955), 124–132.

[103] Saathoff, P., and Melbourne, W. The generation of peak pressures in separated/reattaching flows. *Journal of Wind Engineering and Industrial Aerodynamics 32*, 1 (1989), 121–134.

[104] SAATHOFF, P. J., and MELBOURNE, W. H. Effects of free-stream turbulence on surface pressure fluctuations in a separation bubble. *Journal of Fluid Mechanics 337* (1997), 1–24.

[105] Saha, A., Muralidhar, K., and Biswas, G. Experimental study of flow past a square cylinder at high reynolds numbers. *Experiments in fluids 29*, 6 (2000), 553–563.

[106] Saha, A. K., Muralidhar, K., and Biswas, G. Vortex structures and kinetic energy budget in two-dimensional flow past a square cylinder. *Computers & Fluids 29* (2000), 669–694.

[107] Sarioglu, M., Akansu, Y. E., and Yavuz, T. Control of the flow around square cylinders at incidence by using a rod. *AIAA Journal 43*, 7 (2005), 1419–1426.

[108] Sarpkaya, T. Fluid forces on oscillating cylinders. *Journal of the Waterway, Port, Coastal and Ocean Division 104*, 3 (1978), 275–290.

[109] Sasaki, K., and Kiya, M. Three-Dimensional Vortex Structure in a Leading-Edge Separation Bubble at Moderate Reynolds Numbers. *Journal of Fluids Engineering 113*, 3 (09 1991), 405–410.

[110] Schewe, G. Reynolds-number-effects in flow around a rectangular cylinder with aspect ratio 1:5. *Journal of Fluids and Structures 39* (May 2013), 15–26.

[111] Shaaban, M., and Mohany, A. Phase-resolved piv measurements of flow over three unevenly spaced cylinders and its coupling with acoustic resonance. *Experiments in Fluids 60*, 5 (2019), 71.

[112] Shaaban, M., and Mohany, A. Experimental study of the self-excited resonance effect on the dynamic lift and flow structure around inline cylinders. *Journal of Fluids and Structures 96* (2020), 103015.

[113] Shaaban, M., and Mohany, A. Synchronous vortex shedding from aerodynamically isolated side-by-side cylinders imposed by flow-excited resonant acoustic modes. *Experiments in Fluids 62* (10 2021).

[114] Shaaban, M., and Mohany, A. Flow–acoustic coupling around rectangular rods of different aspect ratios and incidence angles. *Experiments in Fluids 63* (02 2022).

[115] Shair, F. H., Grove, A. S., Petersen, E. E., and Acrivos, A. The effect of confining walls on the stability of the steady wake behind a circular cylinder. *Journal of Fluid Mechanics 17*, 4 (1963), 546–550.

[116] Shoukry, A., and Mohany, A. Direct measurements of the dynamic lift force acting on rectangular rods in cross-flow during acoustic resonance excitation. *Proceedings of the 12th International Conference on Flow-Induced Vibration 1* (2022), 263 – 279.

[117] Sirovich, L. Turbulence and the dynamics of coherent structures. i - coherent structures. ii - symmetries and transformations. iii - dynamics and scaling. *Quarterly of Applied Mathematics - QUART APPL MATH 45* (10 1987).

[118] Sohankar, A., Norberg, C., and Davidson, L. Low-reynolds-number flow around a square cylinder at incidence: study of blockage, onset of vortex shedding and outlet boundary condition. *International Journal for Numerical Methods in Fluids 26* (1998), 39–56.

[119] Soria, J., and Wu, J. The character of the instability of the separated shear layer from a square leading edge flat plate. In *Proc. 11th Australasian Fluid Mech. Conf.* (1992), pp. 391–394.

[120] Stansby, P. Base pressure of oscillating cylinders. *Proc. ASCE J. Eng. Mech. 102* (1976), 591–600.

[121] Stokes, A. N., and Welsh, M. C. Flow-resonant sound interaction in a duct containing a plate; part ii: Square leading edge. *Journal of Sound and Vibration 104* (1986), 55–73.

[122] Stoneman, S. A. T., Hourigan, K., Stokes, A. N., and Welsh, M. C. Resonant sound caused by flow past two plates in tandem in a duct. *Journal of Fluid Mechanics 192* (1988), 455–484.

[123] Strouhal, V. Uber eine besondere ort der tonne regung. *Ann. Phys. Chem. 5*, 10 (1878), 216–251.

[124] Surendran, A., Heckl, M., Peerlings, L., Boij, S., Bodén, H., and Hirschberg, A. Aeroacoustic response of an array of tubes with and without bias-flow. *Journal of Sound and Vibration 434* (11 2018), 1–16.

[125] Taira, K., Hemati, M. S., Brunton, S. L., Sun, Y., Duraisamy, K., Bagheri, S., Dawson, S. T. M., and Yeh, C.-A. Modal analysis of fluid flows: Applications and outlook. *AIAA Journal 58*, 3 (2020), 998–1022.

[126] Tamura, T., and Miyagi, T. The effect of turbulence on aerodynamic forces on a square cylinder with various corner shapes. *Journal of Wind Engineering and Industrial Aerodynamics 83* (1999), 135–145.

[127] Tan, B., Thompson, M., and Hourigan, K. Simulated flow around long rectangular plates under cross flow perturbations. *International Journal of Fluid Dynamics 2* (1998), 1.

[128] Taneda, S. The main structure of turbulent boundary layers. *Journal of the Physical Society of Japan 52*, 12 (1983), 4138–4144.

[129] Taylor, I., and Vezza, M. Prediction of unsteady flow around square and rectangular section cylinders using a discrete vortex method. *Journal of Wind Engineering and Industrial Aerodynamics 82*, 1 (1999), 247–269.

[130] Tong, X., Luo, S., and Khoo, B. Transition phenomena in the wake of an inclined square cylinder. *Journal of Fluids and Structures 24*, 7 (2008), 994–1005.

[131] Trias, F., Gorobets, A., and Oliva, A. Turbulent flow around a square cylinder at reynolds number 22,000: A dns study. *Computers and Fluids 123* (2015), 87–98.

[132] Uffinger, T., Becker, S., and Delgado, A. Investigations of the flow field around different wall-mounted square cylinder stump geometries. In *14th Int Symp on Applications of Laser Techniques to Fluid Mechanics* (2008).

[133] Van Hinsberg, N., Schewe, G., and Jacobs, M. Experiments on the aerodynamic behaviour of square cylinders with rounded corners at reynolds numbers up to 12 million. *Journal of Fluids and Structures 74* (10 2017), 214–233.

[134] van Oudheusden, B. W., Scarano, F., van Hinsberg, N. P., and Watt, D. W. Phase-resolved characterization of vortex shedding in the near wake of a square-section cylinder at incidence. *Experiments in Fluids 39* (2005), 86–98.

[135] Vickery, B. J. Fluctuating lift and drag on a long cylinder of square cross-section in a smooth and in a turbulent stream. *Journal of Fluid Mechanics 25*, 3 (1966), 481–494.

[136] von Kármán, T., and Rubach, H. Uber den mechqnismus des flussigkeits und luftwiderstandes. *Phys. Z. 13*, 2 (1912), 49–59.

[137] Waals, O., Phadke, A., and Bultema, S. Flow induced motions on multi column floaters. *26th International Conference on Offshore Mechanics and Arctic Engineering, San Diego, California, USA 1* (2007), 669—-678.

[138] Wang, P., Ma, H., Deng, Y., and Liu, Y. Influence of vortex-excited acoustic resonance on flow dynamics in channel with coaxial side-branches. *Physics of Fluids 30*, 9 (2018), 095105.

[139] Weaver, D., and Fitzpatrick, J. A review of cross-flow induced vibrations in heat exchanger tube arrays. *Journal of Fluids and Structures 2*, 1 (1988), 73–93.

[140] Welsh, M., and Gibson, D. Interaction of induced sound with flow past a square leading edged plate in a duct. *Journal of Sound and Vibration 67*, 4 (1979), 501–511.

[141] Williamson, C. H. K. Vortex dynamics in the cylinder wake. *Annual Review of Fluid Mechanics 28*, 1 (1996), 477–539.

[142] Wu, J., Sheridan, J., Soria, J., Welsh, M., and Hourigan, K. Experimental investigation of vortex shedding from a plate: effect of external velocity perturbation. *J. Wind Eng. and Ind. Aero. 49* (1993), 401–410.

[143] Yu, D., Butler, K., Kareem, A., Glimm, J., and Sun, J. Simulation of the influence of aspect ratio on the aerodynamics of rectangular prisms. *Journal of Engineering Mechanics 139*, 4 (2013), 429–438.

[144] Zaki, T., S, M., and Gad-El-Hak, M. Numerical and experimental investigation of flow past a freely rotatable square cylinder. *Journal of Fluids and Structures 8*, 7 (1994), 555–582.

[145] Ziada, S., Bühlmann, E., and Bolleter, U. Flow impingement as an excitation source in control valves. *Journal of Fluids and Structures 3*, 5 (1989), 529–549.

[146] Ziada, S., and Shine, S. Strouhal numbers of flow-excited acoustic resonance of closed side branches. *Journal of Fluids and Structures 13*, 1 (1999), 127–142.

[147] Ünal, U., and Atlar, M. An experimental investigation into the effect of vortex generators on the near-wake flow of a circular cylinder. *Experiments in Fluids 48* (06 2009), 1059–1079.

Appendix A

Appendices

A.1 Particle Image Velocimetry (PIV)

To estimate the uncertainty in the PIV measurements, correlation statistics analysis is applied through DaVis 12.0 software. This type of analysis utilizes different factors to estimate the uncertainty such as:

1. Uneven seeding distribution throughout the plane of interest.
2. Background noise due to reflections.
3. Camera focus adjustments.
4. window size for interrogation during post-processing.

The case of $AR = 2$ at a velocity $U_\infty = 19.32 m/s$ under non-resonant conditions is utilized for this analysis. 1200 images are captured after which statistical averaging is performed to construct a time-averaged or phase-averaged flow field. The uncertainty in the flow velocity in the x-direction is obtained with 95% confidence. Figure A.1 shows the uncertainty distribution. We can see that the maximum value is within

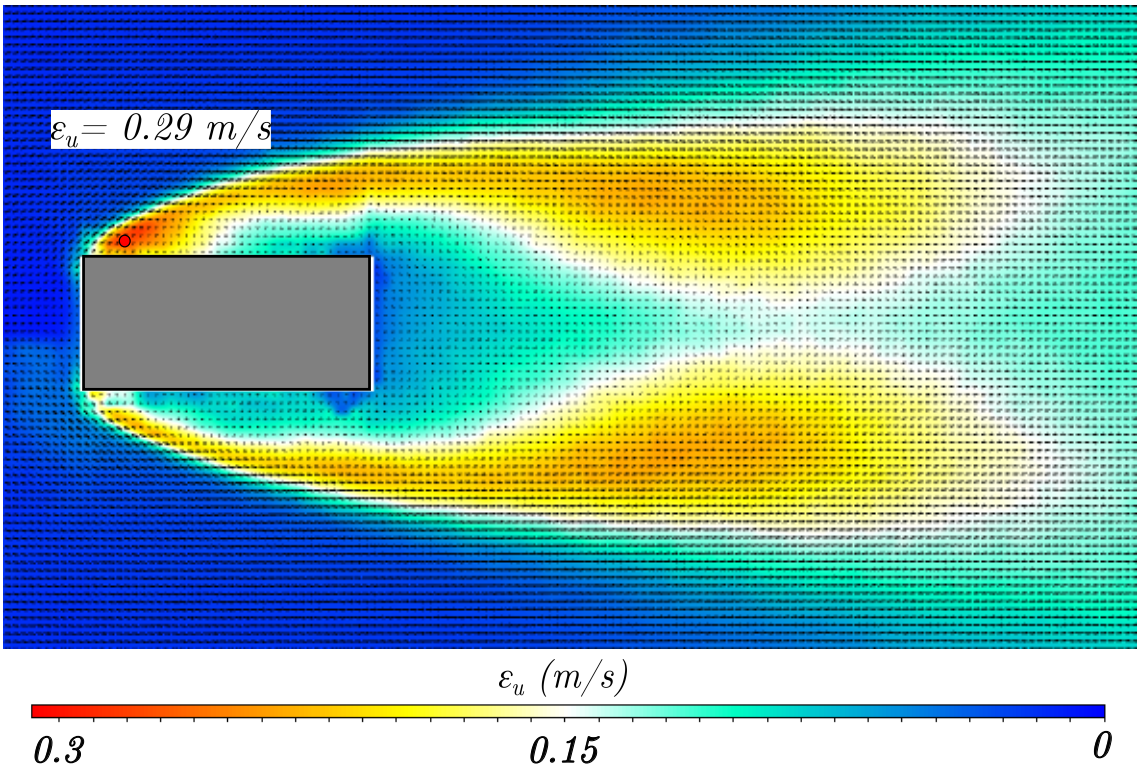

Figure A.1: Uncertainty of time-averaged flow velocity decomposed in the streamwise direction for the case of $AR = 2$ and $\alpha = 0°$

the shear layer right after separation and is equal to $0.29m/s$. The error percentage can be calculated as follows:

$$Error = \frac{\epsilon_u}{U_\infty} \cdot 100 = 1.5\% \tag{A.1}$$